Technische Universität München

Fakultät für Chemie

Max-Planck-Institut für Biochemie

Abteilung für Molekulare Strukturbiologie

“Cryo-EM Studies of Vesicle Inducing Protein in Plastids 1 (Vipp1)”

Tilak Kumar Gupta

Vollständiger Abdruck der von der Fakultät für Chemie der Technischen Universität München zur Erlangung des akademischen Grades eines Doktors der Naturwissenschaften genehmigten Dissertation.

Vorsitzender:	Prof. Dr. Matthias Feige
Prüfer der Dissertation:	1. Hon.-Prof. Dr. Wolfgang Baumeister
	2. Prof. Dr. Johannes Buchner

Die Dissertation wurde am 22.01.2020 bei der Technischen Universität München eingereicht und durch die Fakultät für Chemie am 16.06.2020 angenommen.

Table of Contents

Summary

Thylakoid membrane biogenesis is a multi-dimensional process involving the concerted assembly of proteins and pigments into large membrane-integral complexes, as well as the architectural shaping of an intricate membrane network that organizes these protein complexes in space and time. In recent years, several proteins have been suggested to play crucial roles in thylakoid membrane biogenesis. Vesicle inducing protein in plastids 1 (Vipp1) is one of the best known proteins that is essential for thylakoid biogenesis in both chloroplasts and cyanobacteria. The molecular structure and the exact function of Vipp1 is not yet known.

Due to its strong affinity for lipid, Vipp1 has been proposed to bind to membranes and participate in vesicle transportation and shaping membrane architecture. To explore these proposed functions, we performed an *in vitro* study of Vipp1 protein from the green alga *Chlamydomonas reinhardtii* (CrVipp1). CrVipp1 predominantly oligomerized into extended hollow rods. Using cryo-electron tomography and sub-tomogram averaging, we showed that CrVipp1 rods can engulf liposome membranes containing phosphatidylinositol-4-phosphate (PI4P). We also found that CrVipp1 assembles into rods of variable symmetries and diameters.

To resolve the molecular structure of Vipp1, we studied Vipp1 protein from the cyanobacterium *Synechocystis* sp. PCC 6803 (SynVipp1) using single-particle cryo-electron microscopy. SynVipp1 predominantly assembled into barrel-like rings. We were able to reconstruct electron density maps of five distinct rotational symmetries of Vipp1 (C14 to C18) with resolutions varying from 3.8 to 5 Å. The density maps below 4 Å allowed us to build atomic models of Vipp1. Monomers were found to interweave with each other, giving a basket-like appearance. By comparing the different structures, we identified several regions of flexibility that allow Vipp1 monomers to assemble into rings of variable rotational symmetry. These high-resolution structures also reveal a potential nucleotide binding site in one layer of the Vipp1 ring and provide a structural basis for lipid binding inside the lumen of the ring by Vipp1's N-terminal Helix-1.

Zusammenfassung

Die Biogenese von Thylakoidmembranen ist ein multidimensionaler Prozess, der die Assemblierung Proteinen und Pigmenten zu großen membranständigen Proteinkomplexen beinhaltet, sowie die Bildung eines komplizierten Membrannetzwerks, das diese Proteinkomplexe reguliert. In den vergangenen Jahren wurden einige Proteine als zentrale Regulatoren der Biogenese von Thylakoidmembranen diskutiert. Eines der am besten erforschten Proteine ist das Vesikel-induzierende Protein in Plastiden (Vipp1), das essenziell für die Thylakoid Biogenese sowohl in Chloroplasten als auch in Cyanobakterien ist. Die molekulare Struktur und die genaue Funktion von Vipp1 sind bislang unbekannt.

Aufgrund seiner starken Lipophilie, ist Vipp1 ein Kandidat um Membranen zu binden und zu formen und am Vesikeltransport beteiligt zu sein. Um diese Funktionen zu besser zu verstehen, haben wir eine *in vitro*-Studie an Vipp1 aus der Grünalge *Chlamydomonas reinhardtii* (CrVipp1) durchgeführt. CrVipp1 neigt vorrangig dazu in lange Hohlzylinder zu oligomerisieren. Mit Hilfe der Kryoelektronentomographie und der Untertomogrammmittelung, konnten wir zeigen, dass CrVipp1-Zylinder in der Lage sind, Liposomen bestehend aus Phosphatidylinositol-4- Phosphat (PI4P) einzuhüllen. Wir konnten ebenfalls feststellen dass CrVipp1 in Zylinder mit variablen Symmetrien und Durchmessern assembliert.

Um die molekulare Struktur von Vipp1 aufzulösen, untersuchten wir Vipp1-Protein aus dem Cyanobakterium *Synechocystis sp. PCC6803* (SynVipp1) mit Hilfe von Einzelpartikel Kryoelektronenmikroskopie. SynVipp1 assembliert bevorzugt in Form fassförmiger Ringe. Wir waren in der Lage die Elektronendichte von fünf unterschiedlichen Symmetriestrukturen von Vipp1 (C14 bis C18) mit einer Auflösung von 3.8 bis 5 Å zu berechnen. Die Elektronendichtekarten mit einer Auflösung von unter 4 Å erlaubten uns die Erstellung eines atomaren Modells von Vipp1. Wir stellten fest, dass Monomere sich in eine korbförmige Struktur miteinander verweben. Durch den Vergleich der verschiedenen Strukturen, konnten wir flexible Regionen identifizieren, durch die Vipp1-Monomere sich in Ringe von unterschiedlicher Rotationssymmetrie zusammenfügen kann. Weiterhin zeigen diese hochaufgelösten

Strukturen ein Nukleotid-bindendes Motiv in einer Schicht des Vipp1-Rings und bieten außerdem die strukturelle Basis für Lipidbindung durch die N-terminale Helix-1 im Lumen des Vipp1 Rings.

Publications

Theis, J.*, **Gupta, T.K.***, Klingler, J.*, Wan, W., Albert, S., Keller, S., Engel, B.D., and Schroda, M. (2019). Vipp1 rods engulf membranes containing phosphatidylinositol phosphates. Sci. Rep. *9: 8725*. (*equal contribution)

Theis, J., Niemeyer, J., Schmollinger, S., Ries, F., Rütgers, M., **Gupta, T.K.,** Sommer, F., Muranaka, L.S., Venn, B., Schulz-Raffelt, M., Willmund, F., Engel, B.D., Schroda, M. (2020). Vipp2 interacts with Vipp1 and HSP22E/F at chloroplast membranes and modulates a retrograde signal for HSP22E/F gene expression. Plant Cell Environ. 5: 1212-1229

Gupta, T.K., Klumpe, S., Gries, K., Heinz, S., Wietrzynski, W., Rudack, T., Strauss, M., Baumeister, W., Nickelsen, J., Schuller, J.M., Schroda, M., and Engel, B.D. (2020). Structural basis for Vipp1 ring assembly, nucleotide binding, and lipid interaction. *In revision*.

List of figures

1 Introduction

1.1 Vipp1, a very important protein in plastids

Photosynthesis produces food and oxygen, which make heterotrophic life possible on Earth. The protein complexes that power photosynthesis are embedded within the thylakoid membranes of cyanobacteria, algae, and plants. However, not much is known about the mechanisms that drive the assembly of thylakoid membranes. This is a crucially important question, as the reactions of photosynthesis, and thus most of the life on our planet, rely on these membranes.

Thylakoid membrane biogenesis is a multi-dimensional process, involving the synthesis of lipids, proteins, and pigments, as well as their coordinated transport and integration to form an intricate membrane architecture densely populated with membrane-integral complexes (Vothknecht et al., 2012). In recent years, several proteins have been suggested to play a crucial role in thylakoid membrane biogenesis. Some examples include CURT1 (Armbruster et al., 2013), PratA (Klinkert et al., 2004), Alb3.2 (Göhre et al., 2006), DnaK proteins (Rupprecht et al., 2010) and a prohibitin homolog (Bryan et al., 2011). Another protein that has been strongly implicated in thylakoid membrane biogenesis is the Vesicle inducing protein in plastids 1 (Vipp1).

Vipp1 is an essential protein for thylakoid biogenesis in chloroplasts and cyanobacteria. The exact function, however, is not yet known. Originally named as inner membrane-associated protein of 30kDa (IM30) (Li et al., 1994), Vipp1 is conserved from cyanobacteria to higher plants (Kroll et al., 2001; Westphal et al., 2001a) and appears to have co-evolved with thylakoid membranes (Vothknecht et al., 2012). In higher plants and algae, it is a nuclear-encoded protein that contains an N-terminal signal sequence (Vothknecht et al., 2012). After being translated by cytosolic ribosomes, Vipp1 is imported into the chloroplast by the TOC-TIC general import pathway (Schnell et al., 1997).

1.1.1 Vipp1, an essential protein in the plant kingdom

Vipp1, first identified biochemically in 1994, was found to be located in the inner envelope of the chloroplast and thylakoid membrane of *Pisum sativum*, a pea plant (Li et al., 1994). Later, the Vipp1 gene was identified in the cyanobacterium *Synechocystis* sp. PCC6803 (henceforth *Synechocystis*) and other higher plants such as *Arabidopsis thaliana* (Kroll et al., 2001; Westphal et al., 2001b).

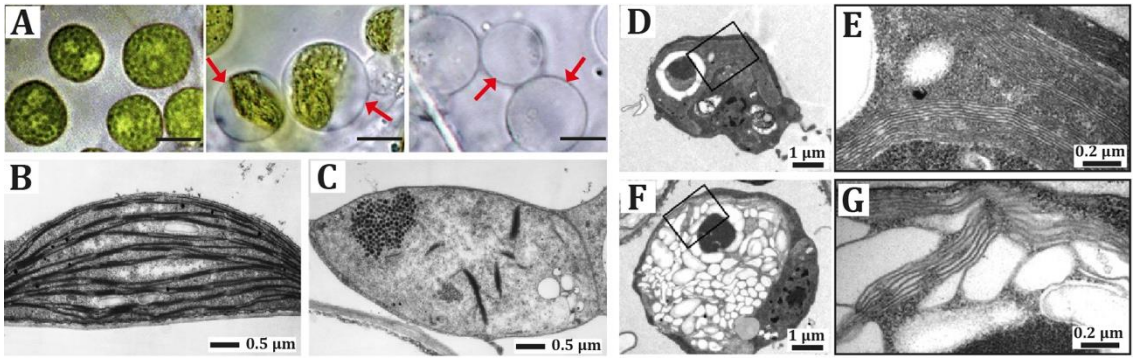

Figure 1: Role of Vipp1 in thylakoid morphology.

A. Vipp1-kd (middle) and Vipp1-ko (right) mutants in *Arabidopsis* show balloon-like chloroplasts (red arrows) with reduced chlorophyll content (green) in comparison to the wild-type chloroplast (left) (modified from Zhang et al., 2012). Scale bars =10 µm.

B-C. EM imaging of *Arabidopsis* shows a typical chloroplast of the wild-type strain (B) and the Vipp1-kd (knockdown to 20%) mutant (C). Thylakoid membranes are almost completely absent in the Vipp1-kd mutant (modified from Aseeva et al., 2007).

D-G. EM imaging of Vipp1-amiRNA strains of *Chlamydomonas* (F-G), and of control strains (D-E). An overview image is shown on the left-side, and a zoom-in of the region demarcated by the black box is shown on the right-side. When cells are shifted to high-light growth conditions, extremely swollen thylakoids are observed in Vipp1-amiRNA strains (F-G) compared to control strains (D-E) (modified from Nordhues et al., 2012).

In *Synechocystis*, Vipp1 could not be deleted completely because it is an essential protein. However, prolonged depletion of Vipp1 leads to severe phenotypes such as strong reduction of thylakoid membranes and decreased levels of active photosystems, thus leading to a deficiency in oxygenic photosynthesis (Fuhrmann et al., 2009a; Gao and Xu, 2009; Kroll et al., 2001; Westphal et al., 2001b). Knockdown (kd) and knockout (ko) mutants of *Arabidopsis* Vipp1 were unable to grow photoautotrophically and caused seedling lethality. The mutants could be maintained on sucrose-supplemented agar, growing into pale-green plants (Kroll et al., 2001). In these *Arabidopsis* VIPP1 mutants, vesicles were no longer found in the chloroplasts upon cold treatment, thus leading to the name “vesicle-inducing protein in plastids” (Kroll et al., 2001).

Furthermore, the Vipp1 mutants have swollen, balloon-like chloroplasts due to increased osmotic stress on the plastid envelope (Figure 1A) (Zhang et al., 2012). Further effects of knockdown mutants are shown in Figure 1B-G.

1.1.2 PspA, a bacterial homolog of Vipp1

PspA is the bacterial homolog of the Vipp1 protein. Vipp1 likely evolved in a cyanobacterial ancestor from PspA via gene duplication (Heidrich et al., 2017; Westphal et al., 2001b). PspA, discovered in 1990, is a member of the phage shock protein system and is involved in the bacterial stress response.

Cyanobacteria have both PspA and Vipp1 genes (Zhang and Sakamoto, 2015). Genomic analysis suggested that the evolution of thylakoids in photosynthetic organisms coincides with the acquisition of Vipp1, whereas PspA has been lost in land plants and only Vipp1 remains (Zhang and Sakamoto, 2015). Furthermore, PspA is a non-essential protein in bacteria, whereas Vipp1 is essential for normal development of both cyanobacteria and higher plants (Aseeva et al., 2007; Fuhrmann et al., 2009a; Kroll et al., 2001; Weiner and Model, 1994; Westphal et al., 2001b). Due to the common origin of Vipp1 from PspA, they share a similar structure and many similar functions. These include a predominantly α-helical structure, the formation of oligomeric high molecular weight complexes, an affinity for membranes, and an apparent role in coping with membrane stress (Aseeva et al., 2004; Bultema et al., 2010; Fuhrmann et al., 2009b; Hankamer et al., 2004).

Vipp1-family proteins from the following organisms have been studied to understand their structure and function:

1. Bacterial PspA
2. Vipp1 from cyanobacteria, such as *Synechocystis sp. PCC 6803* (protein henceforth referred to as SynVipp1)
3. Vipp1 from green algae, such as *Chlamydomonas reinhardtii* (protein henceforth referred to as CrVipp1)
4. Vipp1 from higher plants, such as *Arabidopsis thaliana* (protein henceforth referred to as AtVipp1) and *Pisum sativum*.

1.1.3 Vipp1 is primarily localized to the thylakoid membranes and inner membrane of the chloroplast

Vipp1 was identified to be bound specifically to membranes with high curvature stress (Gutu et al., 2018; McDonald et al., 2015) and was found to co-localize with CURT1, a protein believed to induce thylakoid membrane curvature (Armbruster et al., 2013; Heinz et al., 2016). However, no evidence of direct Vipp1-CURT1 interaction has been found (Bryan et al., 2014; Heinz et al., 2016), thus the co-localization is likely caused by the membrane curvature itself. Vipp1 was also suggested to function as a membrane chaperone at the curved membrane region (Thurotte et al., 2017).

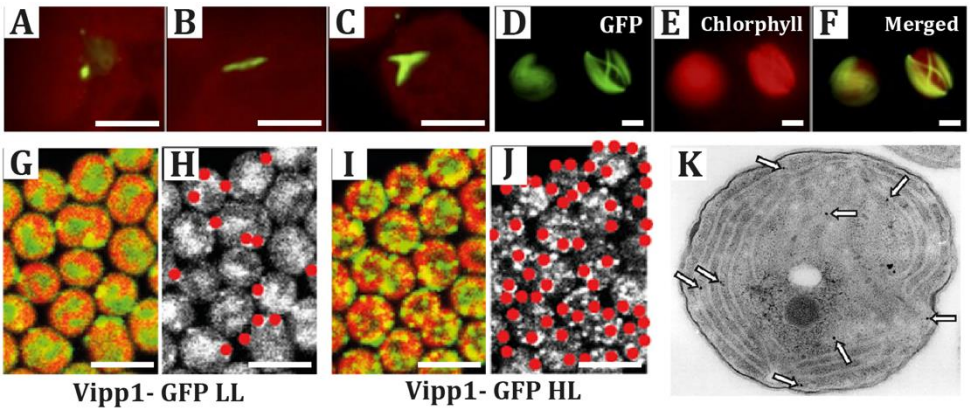

Figure 2: *In vivo* higher-order assembly and localization of Vipp1.

A-C. Light microscopy studies revealed that Vipp1-GFP formed various supercomplexes along the chloroplast envelope in *Arabidopsis* such as a dot (A), line (B) and fork (C) (modified from Zhang et al., 2012).

D-F. Lattice-like structures of Vipp1-GFP occasionally formed along the chloroplast envelope of *Arabidopsis* (modified from Zhang et al., 2012).

G-J. Vipp1–GFP was found to be redistributed under high-light in *Synechocystis*. Confocal microscopy imaging of Vipp1-GFP showed that cells grown in low light conditions had few puncta (G-H), but when shifted to high light conditions, many Vipp1 puncta were formed (I-J). The overlay of chlorophyll (red) and Vipp1:GFP (green) signal is shown in G-I, and the localized puncta of GFP fluorescence are indicated with red dots in H-J (modified from Bryan et al., 2014).

K. Subcellular localization of Vipp1 in *Synechocystis* has been shown by immunogold labeling of Vipp1-GFP combined with EM imaging. Vipp1-GFP (black arrowheads) was observed to be enriched near the edges of thylakoids (high curvature regions) (modified from Fuhrmann et al., 2009b).

Light microscopy studies revealed that Vipp1-GFP formed various supercomplexes along the chloroplast envelope in *Arabidopsis* (Figure 2A-C). Fluorescence microscopy-based *in vivo* studies in cyanobacteria showed that Vipp1 has two discrete localization patterns: puncta located at the inner membrane and freely

diffuse in the cytoplasm. This distribution was proposed to be dynamic, as a shift in localization was clearly visible when the cells were transferred from the low light (mainly diffuse) to high light (stable puncta near the inner membrane) (Figure 2G-J) (Bryan et al. 2014). A more recent super-resolution light microscopy study of cyanobacteria found that Vipp1 puncta were located to regions of high curvature on thylakoid membranes. In growing cells, these puncta were short-lived (1-2 min), whereas in non-growing cells they appeared to be stable (Gutu et al. 2018). In an interesting parallel, PspA and LiaH (PspA orthologue in *Bacillus subtilis*) were found evenly distributed throughout the bacterial protoplasm under non-stress conditions but formed discrete puncta under defined stress conditions (Engl et al. 2009; Yamaguchi et al. 2013; Domínguez-Escobar et al. 2014; Gutu et al. 2018; Manganelli & Gennaro 2017).

Early electron microscopy (EM) studies showed that thylakoid centers in cyanobacteria (regions where multiple thylakoid membranes converge) contain rod-shaped structures of 50 to 1000 nm length and 30 to 50 nm width (Kunkel 1982; Van De Meene et al. 2006; Rütgers & Schroda 2013). Similar structures, referred to as microtubule-like structures (MTLs), have been observed in plastids of diverse algal and plant species. MTLs have diameters of 15 to 40 nm, reach lengths of up to 5 µm, and appear to bridge inner envelope and thylakoid membranes (Lawrence & Possingham 1984; Schnepf 1961; Pickett-Heaps 1968; Newcomb 1967; Rütgers & Schroda 2013).

In vitro-assembled Vipp1 rings/rods resemble MTLs and the structures found within the cyanobacterial thylakoid centers. In support of this, GFP-tagged Vipp1 in *Arabidopsis* was found to organize into rod-like structures along the inner envelope (Figure 2B) (Zhang et al. 2012a). It has been debated whether Vipp1 rods are similar to these cytoskeleton-like structures and whether they provide a “railway” for the transport of proteins and lipids (Liu et al. 2007). In another proposed function, these rods were hypothesized to serve as an inert storage box inside cyanobacteria and chloroplasts (Liu et al. 2007). However, a recent cryo-electron tomography study of *Synechocystis* failed to find large rings or rods *in vivo*, and instead showed that the large rod-like strucutures previously described in cyanobacteria are in fact membrane tubules that connect thylakoid membranes to the plasma membrane (Rast et al., 2019).

1.2 The structure of Vipp1

1.2.1 The Vipp1 monomer consists of seven α-helices

SynVipp1 is a protein of 267 amino acids. The CrVipp1 protein is 251 amino acids long, excluding its signal peptide (Figure 3A). At the secondary structure level, Vipp1 has two major domains: an N-terminal PspA-like domain and a C-terminal helix of 16-20 amino acids separated by a linker region of variable length (Figure 3B) (Heidrich et al., 2017; Otters et al., 2013; Vothknecht et al., 2012; Westphal et al., 2001b).

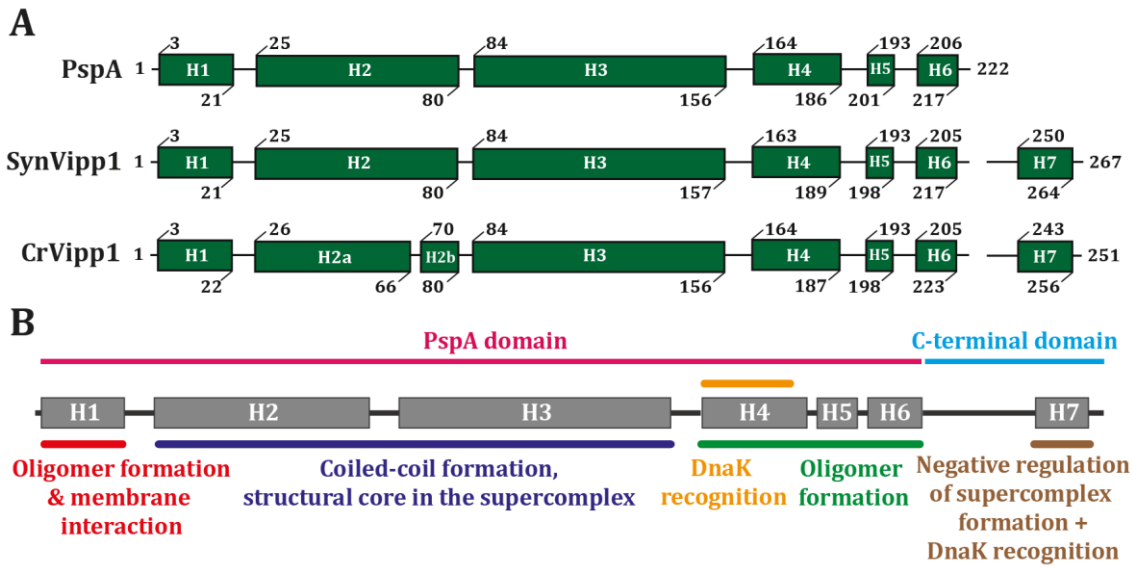

Figure 3: Secondary structure elements of PspA, SynVipp1 and CrVipp1, and the predicted functions of each of the domains.

A. This domain model is based on results from several prediction programs (Phyre, JPred3, NSP@, Predator, GORIV, PSIPred). Numbering refers to amino acid residues of the mature Vipp1 without its transit sequence (modified from Otters et al., 2013).

B. The first six α-helices of Vipp1 are homologous to PspA and form the PspA domain (pink line). Vipp1 has an additional helix (H7) of 16-20 amino acids separated by a linker region of variable length (sky-blue line). Reported and proposed functions of corresponding Vipp1 helices (H1-H7) are mentioned (modified from Heidrich et al., 2017).

The PspA domain of Vipp1 shares a conserved α-helical secondary structure with the bacterial PspA protein (Bultema et al., 2010; Fuhrmann et al., 2009b; Hankamer et al., 2004; Otters et al., 2013). While the amino acid sequence is not strictly conserved between the proteins, these proteins share a highly conserved secondary structure. Various computational methods were used to predict the secondary

structure of Vipp1 to consist of seven α-helixes (Figure 3A). These α-helices play a crucial role in the structural stability, macromolecular assembly and potential function of Vipp1. Some of these functions are summarized in Figure 3B.

The complete structures of PspA and Vipp1 are not yet known. Recently, the N-terminal fragment of PspA (amino acid 3-144) was solved by X-ray crystallography and found to have a coiled-coil structure (Osadnik et al., 2015). This structure was consistent with the computationally predicted secondary structure of PspA. As PspA and Vipp1 share similar secondary structure, the crystal structure of PspA was used to model Vipp1 (Saur et al., 2017).

1.2.1.1 N-terminal Helix-1 of Vipp1 (Helix-1)

N-terminal Helix-1 (henceforth H1 or Helix-1) is an amphipathic α-helix with several highly conserved amino acid positions (Westphal et al., 2001b). Structurally, H1 plays a crucial role in the stability of Vipp1 higher-order assemblies (Figure 6). The helical wheel projection of H1 shows that hydrophobic amino acid residues clearly fall on one side of the helix and thus are proposed to be involved in lipid interactions (Figure 4A and Figure 8) (McDonald et al., 2015; Otters et al., 2013). The H1 domains of PspA and Vipp1 exhibit high affinities for membranes that contain lipid-packing defects (i.e., membranes exhibiting stored curvature elastic [SCE] stress) (McDonald et al., 2015, 2017).

Strong evidence has been found to support a direct lipid interaction by the N-terminal H1 of PspA and Vipp1 (McDonald et al., 2017). In this study, the individual peptides of PspA (1–24 amino acids) and Vipp1 (1–24 amino acids) were analyzed for their effect on membrane stability. The binding of these peptides destabilized membrane vesicles. However, the $PspA_{1-24}$V11E mutant did not have such an effect. The destabilizing nature of this interaction seems counterintuitive for a membrane maintenance role of PspA and Vipp1 *in vivo*. It was proposed that PspA and Vipp1 higher-order oligomers may function to limit the number of contacts that can be made with the membrane (McDonald et al., 2017). Point mutant substitutions such as F4E, V11E, and N14D have been shown to decrease the membrane interaction ability of PspA. Additionally, a P25A mutant was shown to severely compromise membrane

binding. Proline was proposed to play an important role in proper positioning of H1 onto the membrane and, possibly, high-order oligomer formation (Jovanovic et al., 2014).

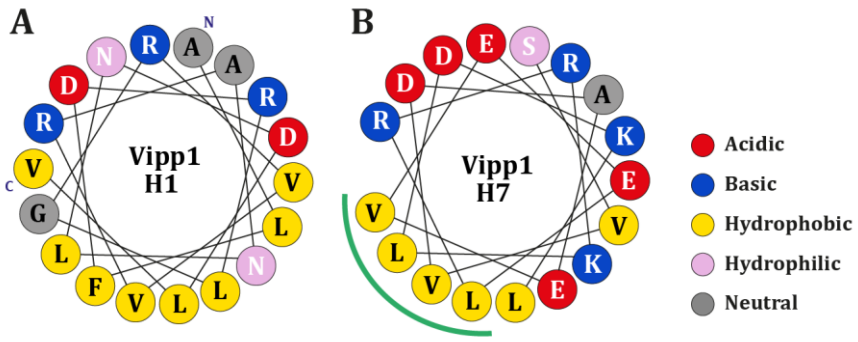

Figure 4: Helical wheel projection of the amino acids of Vipp1 Helix-1 and Helix-7.

A. Helical wheel projection of the N-terminal Helix-1 (residues from 2 to 19) of SynVipp1. Three positively charged amino acids face one side, and the hydrophobic amino acids all face the opposite side, making it an amphipathic α-helix (modified from McDonald et al., 2017).

B. Helical wheel projection of the consensus sequences of the Helix-7. This is also predicted to be an amphipathic α-helix with a small hydrophobic patch facing on one side of the helix (indicated by a green arch) (modified from Vothknecht et al., 2012).

1.2.1.2 C-terminal Helix-7 of Vipp1 (Helix-7)

The C-terminal domain is an additional feature of Vipp1 that is absent from PspA. A multiple-sequence alignment of Vipp1 homologs in cyanobacteria, algae and plants revealed the conserved non-polar, amphipathic properties of the extra C-terminal Helix-7 (hereafter H7 or Helix-7), even though most amino acids are not strictly conserved (Figure 4B) (Vothknecht et al., 2012). H7 was proposed to face outward and upward in a Vipp1 ring structure, providing an interaction surface for proteins, lipids or membranes (Aseeva et al., 2004; Vothknecht et al., 2012). The C-terminal H7 is not required for oligomerization and stability of the Vipp1 macromolecular assembly (Figure 6) or for membrane interaction (Figure 8). Rather, it is assumed to be responsible for a Vipp1-specific function (Aseeva et al., 2004, 2007; Liu et al., 2007; Otters et al., 2013), and recently, H7 was found to be involved in the negative regulation of Vipp1 oligomerization (Zhang et al., 2016a)

1.2.2 Vipp1 oligomerizes to make higher-order assemblies

Both PspA and Vipp1 form large homo-oligomeric rings with molecular masses of more than 1 MDa (Figure 5). Their ring dimensions, however, differ significantly. Vipp1assembles into rings of different rotational symmetries (C12-C17) (Bultema et al., 2010), whereas PspA appears to make a single type of ring with nine-fold rotational symmetry (Hankamer et al., 2004). The height of the PspA ring is ~8.5 nm, which is considerably smaller than that of Vipp1 rings (~22 nm) (Bultema et al., 2010).

In vivo, Vipp1 exists in an equilibrium between soluble and membrane-bound forms (Fuhrmann et al., 2009b). In an *Arabidopsis* mutant strain where Vipp1 levels are low, no oligomeric structure of Vipp1 was found. It was proposed that a critical concentration of Vipp1 is needed for the formation of higher-order structures *in vivo* (Aseeva et al., 2007).

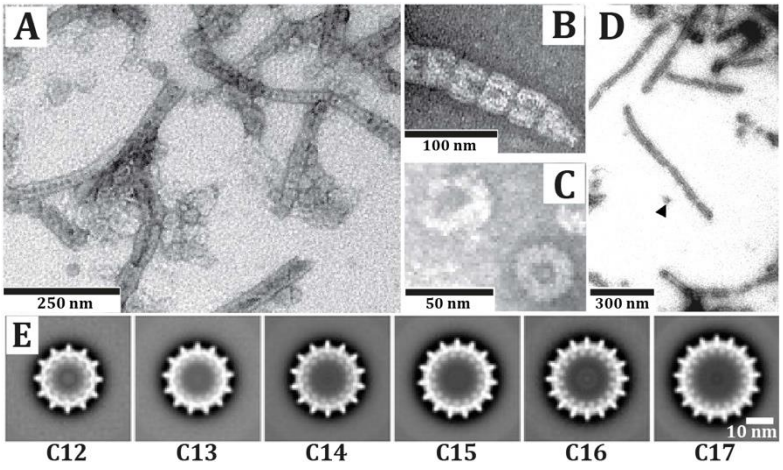

Figure 5: PspA and Vipp1 assemble into higher oligomeric structures *in vitro*.

A-C. Negative stain EM of PspA shows a mixture of rings and rod-like structures (A). A close-up on a rod-like structure showed the indentations and striations (B). A close up of PspA ring structure (C), indicating that the stacking of rings results in a rod-like PspA structure (modified from Male et al., 2014).

D. Negative stain EM image of CrVipp1 showed that it assembles into rings (arrowhead) and rod-like structures *in vitro* (modified from Rütgers and Schroda, 2013).

E. Negative stain EM revealed that SynVipp1 form rings of various rotational symmetries *in vitro* (modified from Fuhrmann et al., 2009b; Heidrich et al., 2017).

Furthermore, *in vivo Synechocystis* studies showed that Vipp1 is distributed between cytosol, cell membrane and thylakoid membrane depending on the light intensity used to grow cells (Bryan et al., 2014). Little is known about whether

oligomeric Vipp1 assemblies such as rings or rods are present in the cell, either in solution or bound to membranes. It has been speculated that ring formation is crucial for membrane binding (Heidrich et al., 2017). *In vitro*, Vipp1 from several species has been observed to form rings and rods in solution (Aseeva et al., 2004; Fuhrmann et al., 2009b; Gao et al., 2015; Heidrich et al., 2016; Liu et al., 2007; Otters et al., 2013; Zhang et al., 2016a).

PspA had been identified in two forms: a hexamer in the solution that interacts with the transcription factor PspF and 36mer ring that interacts with membranes (Jovanovic et al., 2014; Kobayashi et al., 2007b; Osadnik et al., 2015). In contrast, Vipp1 has not been identified in a hexamer form (Heidrich et al., 2017). However, Vipp1 might exist in a highly oligomerized state (potentially rings or rods) when removed from membranes (Fuhrmann et al., 2009b). This theory is supported by the *in vitro* EM observation that Vipp1 rings can attach peripherally to liposomes containing negatively charged lipids (Figure 7E-G) (Hennig et al., 2015). However, the rings disappeared from the liposomes after prolonged incubation with Vipp1 and Mg^{2+}.

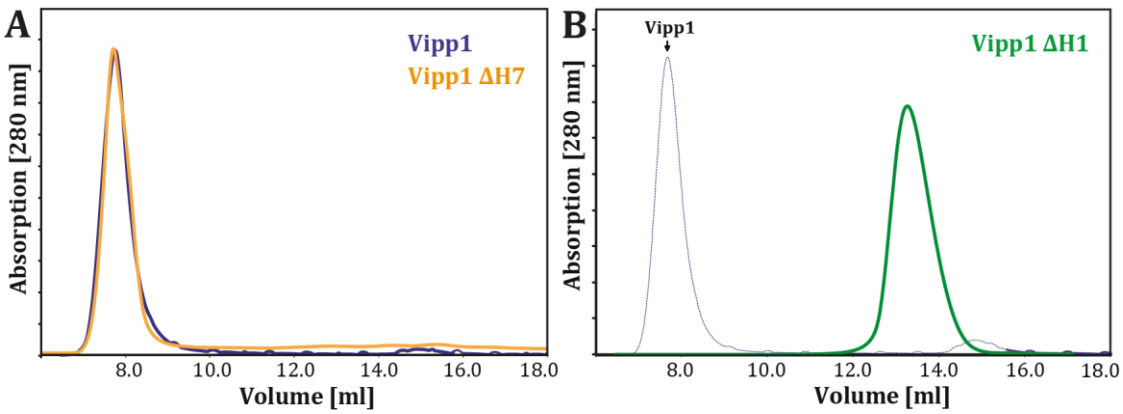

Figure 6: Effects of Helix-7 and Helix-1 on the stability of higher-order oligomeric structure of AtVipp1.

A. Size-exclusion chromatography profile of wild-type AtVipp1 (Vipp1) and C-terminally truncated AtVipp1 (Vipp1 ΔH7). The deletion of C-terminal Helix-7 does not affect the higher-order oligomeric structure of AtVipp1.

B. Size-exclusion chromatography profile of wild-type AtVipp1 (Vipp1) and N-terminally truncated AtVipp1 (Vipp1 ΔH1). The deletion of N-terminal Helix-1 caused the disappearance of higher-order oligomeric species from the high molecular weight range. This demonstrates that Helix-1 is required for Vipp1 to form heavy oligomers (A-B are modified from Otters et al., 2013).

Low-resolution 3D structures of synVipp1 rings in multiple symmetries were determined by negative stain EM (Figure 7A-D). Vipp1 monomers were proposed to

assemble into tetramers, which then oligomerize vertically to make a Vipp1 ring (Saur et al., 2017).

Chaperones may play a crucial role in Vipp1 assembly and disassembly. For example, Vipp1 oligomerization in *C. reinhardtii* chloroplasts was proposed to be regulated by the Hsp70B-CDJ2 CGE1 chaperone system (Liu et al., 2005). *In vitro* experiments showed that CrVipp1 rings/rods are disassembled in the presence of these chaperones and ATP (Liu et al., 2007). This ATP-dependent interaction of chaperones with Vipp1 is proposed to regulate Vipp1 oligomerization *in vivo*.

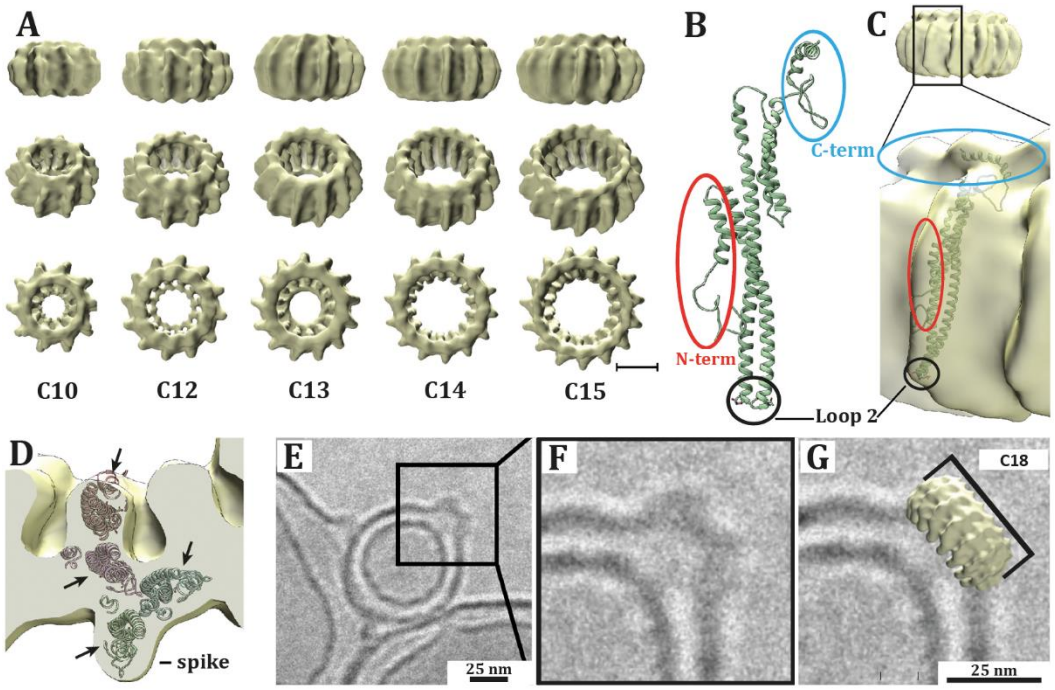

Figure 7: Negative stain EM study of *Synechocystis* Vipp1 *in vitro.*

A. 3D reconstruction showing that SynVipp1 assembles into rings of variable symmetry but similar morphology. One side of the ring is more constricted (defined as the bottom of the ring) than the other (defined as the top). Scale bar =10 nm

B. The full-length structure of wild-type SynVipp1 was computationally predicted with the help of the Rosetta program using the partial crystal structure of PspA.

C. The predicted Vipp1 monomer model was fitted into the 3D volume of a Vipp1 ring. The red circle and the sky-blue circle illustrate the N-terminal H1 and the C-terminal domain (including H7), respectively. The black circle marks the Loop 2 region. According to this model, the N-terminal H1 faces outwards and the C-terminal H7 faces upwards.

D. Model showing that four Vipp1 monomers can fill the EM density of a basal ring "building block" (A-D are modified from Saur et al., 2017).

E-F. The membrane-binding affinity of SynVipp1. When SynVipp1 was incubated with liposomes, extra electron densities were found on membrane surfaces (E). Zoom-in of the boxed area (F). This extra density was superimposed with a Vipp1 ring having C18 rotational symmetry (G) (modified from Hennig et al., 2015).

1.3 Proposed physiological functions of Vipp1

The precise physiological function of Vipp1 is not yet known. However, knock-down and knock-out mutants from multiple species have shown altered thylakoid structure and morphology (Figure 1). In the last two decades, studies have linked Vipp1 to a variety of processes, where Vipp1 may play either direct or indirect roles. Many of these functions are summarized below:

1.3.1 Thylakoid biogenesis

In cyanobacteria, tubular membranes called "convergence membranes" or "thylakoid centers" closely tether the tips of multiple thylakoid membranes to the plasma membrane. While the thylakoids and plasma membrane remain discrete membrane systems, the close tethering likely allows the exchange of proteins, lipids and other components needed for the formation of thylakoids (Frain et al., 2016; Kunkel, 1982; Nickelsen and Rengstl, 2013; Rast et al., 2019; Stengel et al., 2012). Vipp1 is proposed to be a structural core component within these thylakoid centers, which is further supported by the observation that GFP-labelled Vipp1 localizes selectively at the cell periphery (Bryan et al., 2014; Rütgers and Schroda, 2013).

Chloroplasts also have convergence zones where multiple thylakoid tips face the plasma membrane. However, there is not convergence membrane and thus, the thylakoids are not closely tethered to the plasma membrane (Engel et al., 2015; Heidrich et al., 2017). Exchange of material may take place via vesicle transfer or transient membrane fusion (Heidrich et al., 2017; Lindquist et al., 2016), although both of these events are seldom seen in *Chlamydomonas* (Engel et al., 2015). Vipp1 was proposed to play an important role in thylakoid membrane biogenesis by mediating the transport of protein complexes and structural lipids via vesicle formation or membrane fusion events (Heidrich et al., 2017; Nordhues et al., 2012).

An interplay between Vipp1-HSP70B-CDJ2 chaperone system and membrane integrase ALB3.2 has also been suggested. The downregulation of ALB3.2 led to the upregulation of Vipp1 and the chaperones (Göhre et al., 2006). The addition of

recombinant Vipp1 to thylakoid membranes was shown to increase TAT-mediated protein import *in vitro* (Lo and Theg, 2012). The depletion of Vipp1 in higher plants and cyanobacteria affects thylakoid membrane assembly, resulting in photosynthetic defects (Kroll et al., 2001; Westphal et al., 2001b). The depletion of Vipp1 in *Synechocystis* first led to a loss of the photosystems from thylakoids before the thylakoid membranes, themselves, were affected (Gao and Xu, 2009). In *Arabidopsis*, depletion of Vipp1 caused dysfunction of the entire photosynthetic electron transport chain (Kroll et al., 2001). Vipp1 was suggested to play a role not only in thylakoid membrane formation but also in the biogenesis and maintenance of photosystem core complexes (Aseeva et al., 2007). Photosystem I was drastically reduced upon Vipp1 depletion in cyanobacteria (Fuhrmann et al., 2009a; Zhang et al., 2014). However, in *Chlamydomonas*, the depletion of Vipp1 led to the reduced levels of photosystem II. Therefore, Vipp1 was proposed to be significantly involved in photosynthetic complex formation and/or transport (Heidrich et al., 2017; Zhang and Sakamoto, 2015).

1.3.2 Affinity of Vipp1 for lipids and membranes

1.3.2.1 Membrane binding and transport of lipids and proteins

Binding of Vipp1 to membranes is affected by the physical properties of the membranes, including the surface charge and stored curvature elastic stress (Heidrich et al., 2017). Interaction between a protein's positively-charged amino acids and a membrane's negatively charged lipids had been shown to mediate the membrane binding of many peripheral membrane proteins (McLaughlin and Aderem, 1995; Zhou et al., 1994).

SynVipp1 has been shown to interact with dioleoylphosphatidylglycerol (DOPG) (Hennig et al., 2015; McDonald et al., 2015) and sulfoquinovosyl diacylglycerol (SQDG) (Hennig et al., 2015). Similarly, bacterial PspA was shown to interact with negatively-charged lipids such as phosphatidylglycerol (PG) and phosphatidylserine (PS) (Kobayashi et al., 2007b; McDonald et al., 2015). The acyl chain length does not seem to be important for the Vipp1-membrane interaction, as Vipp1 interacts with both 1,2-dimyristoyl-sn-glycero-3-phosphoglycerol (DMPG) and DOPG (Heidrich et al., 2016). However, it remains unknown whether the interactions of PspA and Vipp1 with

negatively-charged membrane surfaces are simply due to electrostatic attractions, or whether these interactions require specific hydrophobic or amphiphilic protein regions (Heidrich et al., 2017).

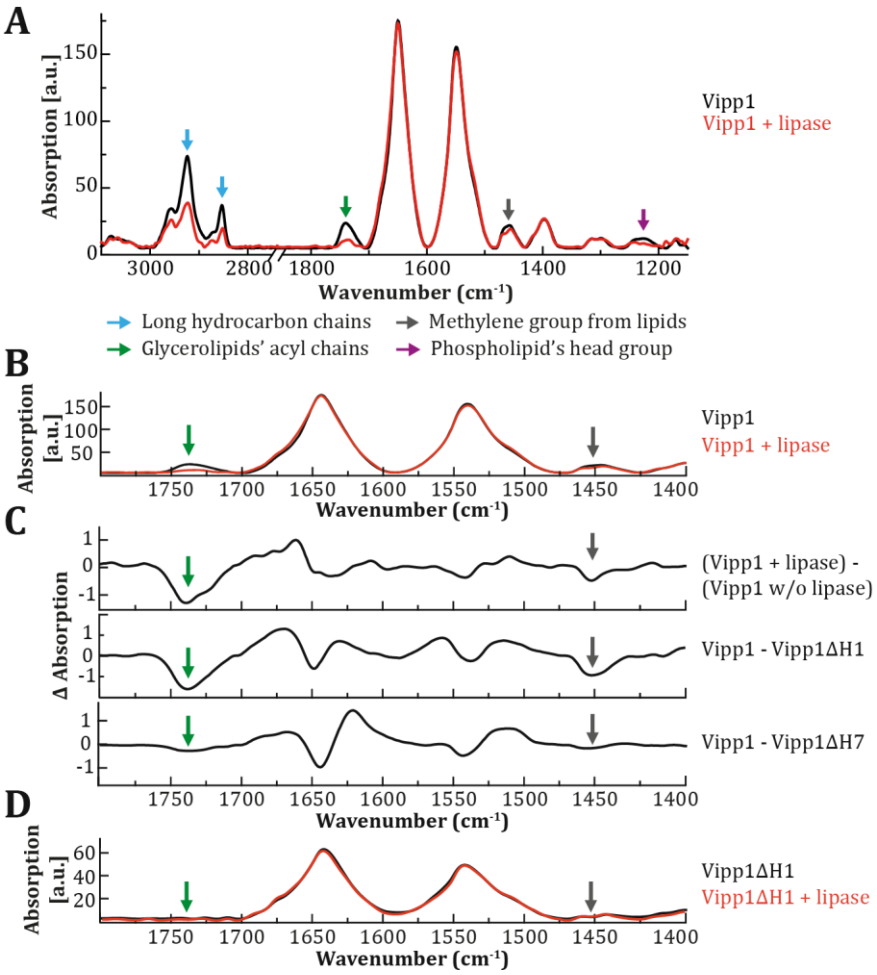

Figure 8: Vipp1 has a strong affinity for lipids.

Lipid binding affinity of Vipp1, studied by Attenuated Total Reflectance-Fourier Transform Infrared Spectroscopy (ATR-FTIR).

A. Complete ATR-FTIR spectra of Vipp1 before (black line) and after (red line) lipase treatment. Peaks corresponding to specific lipid features are annotated with colored arrows.

B. Selected ATR-FTIR spectra of Vipp1 before (black line) and after (red line) lipase treatment. Distinct peaks are marked with green and gray, which are further compared for other Vipp1 mutants.

C. Comparison of IR-difference spectra of Vipp1 before/after lipase treatment of Vipp1/Vipp1 ΔH7 and of Vipp1/Vipp1 ΔH1 shows a clear loss of lipid absorption bands in Vipp1 ΔH1.

D. No change is observed in ATR-FTIR spectra of Vipp1 ΔH1 before (black line) and after (red line) lipase treatment, indicating that lipid binding affinity is greatly reduced for the mutant (A-D are modified from Otters et al., 2013).

It was suggested that the N-terminal amphipathic H1, conserved between PspA and Vipp1, binds parallel to the lipid bilayer with the helix's central axis laying between

the membrane's polar head-groups and hydrophobic alkyl chains. Binding in this manner might enable H1 to "sense" membrane curvature stress (Engl et al., 2009).

Vipp1 has a strong affinity for lipids. When heterologously expressed in *E. coli,* Vipp1 was purified with strongly-bound bacterial lipids (Heidrich et al., 2017; Otters et al., 2013). Biophysical observations with attenuated infrared spectroscopy have shown a significant reduction in lipid group absorption when heterologously-expressed Vipp1 was treated with lipase enzyme (Figure 8) (Otters et al., 2013). A slightly altered Vipp1 structure was reported in the lipase-treated sample, indicating that a specific lipid-protein interaction may affect the conformations of Vipp1 assemblies (Otters et al., 2013).

One of the first proposed functions of Vipp1 was lipid transport (Benning et al., 2006; Li et al., 1994). Some of the thylakoid membrane lipids such as monogalactosyldiacylglycerol (MGDG) are synthesized in the inner envelope of the chloroplast (Douce, 1974; Joyard and Stumpf, 1981; Keren et al., 2005; Kobayashi et al., 2007a; Selão et al., 2016; Zak et al., 2001). How these lipids are then transported from the inner membrane to the thylakoid membrane is not yet known. Several observations suggest that Vipp1 may play a role in lipid transport (Heidrich et al., 2017; Nordhues et al., 2012). Swelling of the thylakoid membranes in Vipp1-RNAi *Chlamydomonas* cells suggested a structural defect in thylakoid membranes (Nordhues et al., 2012; Rütgers and Schroda, 2013). It was speculated that Vipp1 directly transports lipids during thylakoid biogenesis (Rütgers and Schroda, 2013). Radiolabeled lipid was detected in the chloroplast inner envelope before it was detected in the thylakoid membrane, indicating a directional transport mechanism between these two compartments (Andersson and Sandelius, 2004; Heidrich et al., 2017). It remains debated whether this transport proceeds via vesicles or via contact sites such as the cyanobacterial convergence membranes (Rast et al., 2019). In higher plants, a vesicle-mediated transport system had been suggested based on the EM observations of vesicle-like structures in the chloroplasts of *A. thaliana* and *P. sativum* at low temperature (Kroll et al., 2001; Morré et al., 1991; Westphal et al., 2001b). Interestingly, in the Vipp1 knockdown strain of *A. thaliana*, these vesicles were no longer found (Kroll et al., 2001). Vipp1 was proposed to sustain this vesicle transport system by stabilizing highly bent

membranes during vesicle budding, a role that is similar to coat proteins in the secretory pathway (Vothknecht et al., 2012). The diverse oligomeric Vipp1 ring structures could also be involved in vesicle constriction, similar to dynamins in eukaryotes (Fuhrmann et al., 2009b). However, this proposed function lacks experimental evidence (Heidrich et al., 2017).

In an alternative possibility, Vipp1 was proposed to create microdomains enriched in specific lipid species, like PG (Rütgers and Schroda, 2013). Such a function would be analogous to eisosomes in yeast, furrow-like invaginations of the plasma membrane that are enriched in sterols. Eisosomes are formed by the Pil1 and Lsp1 proteins (Strádalová et al., 2009). Both these proteins also assemble into rod-like structures *in vitro* (resembling Vipp1 rods) that can bind and tubulate liposomes (Karotki et al., 2011).

Vipp1 has been proposed to be involved in protein transport and insertion in thylakoid membranes based on the interaction of Vipp1 with Albino3.2 in *C. reinhardtii* (Göhre et al., 2006). Albino3.2 is a protein required for the insertion of certain integral membrane proteins into the thylakoid membrane (Göhre et al., 2006; Walter et al., 2015; Wang and Dalbey, 2011). During Albino3.2-mediated membrane integration of protein complexes, the membrane structure might be locally perturbed, which may recruit Vipp1 to stabilize the membrane (Vothknecht et al., 2012). A similar membrane-stabilizing role was suggested for *E. coli* PspA during YidC-mediated protein insertion (Van der Laan et al., 2003). Another study concurred with this idea, proposing that Vipp1 and PspA may not directly aid protein insertion, but rather help maintain membrane integrity during the protein insertion process by YidC or Albino3.2 (Heidrich et al., 2017). Furthermore, Vipp1 was proposed to be a crucial factor involved in the formation of an MGDG inverse hexagonal lipid platform that acts as a connection and transfer point between embryonic thylakoid membranes and the chloroplast inner envelope (Bastien et al., 2016). Such platforms might be crucial to transfer proteins and/or lipids in between membranes (Bastien et al., 2016; Selão et al., 2016).

1.3.2.2 Membrane protection

Maintaining thylakoid membrane integrity and the proton gradient across this membrane is essential for cell survival (Heidrich et al., 2017). Vipp1 is proposed to protect thylakoids based on the known function of PspA, which acts as a sensor of membrane stress and then responds to protect the cell against this stress by activating a complete operon system (Kleerebezem et al., 1996; Kobayashi et al., 2007b; Standar et al., 2008; Yamaguchi et al., 2013). In *E. coli*, PspA was reported to form a large scaffold structure to stabilize the stressed membranes (Kleerebezem et al., 1996; Kobayashi et al., 2007b; Standar et al., 2008; Yamaguchi et al., 2013). Also, PspA binds preferentially to the cell poles of *E. coli* (Engl et al., 2009), where it protects the highly curved membrane region from proton leakage. Moreover, only the higher-order PspA oligomers were able to repair the membrane upon stress (Kobayashi et al., 2007b). Vipp1 was able to functionally complement the role of PspA in an *E. coli* ΔpspA strain (DeLisa et al., 2004).

There is also evidence that Vipp1 is involved in membrane stress protection. It is believed to form a lattice-like scaffold that facilitates the resealing of osmotically damaged chloroplast envelope (Figure 2D-F) (Zhang et al., 2012). Upon hypotonic treatment, GFP-labeled Vipp1 was observed to form filament-like structures at the envelope's inner membrane, which might be Vipp1 oligomers stabilizing this membrane (Bryan et al., 2014; Zhang et al., 2016a). Ectopic expression of Vipp1 in *A. thaliana* was shown to promote plant tolerance against heat shock stress and oxidative stress (McDonald et al., 2015; Zhang et al., 2016b, 2016a). Vipp1's extra C-terminal helix (H7) was also suggested to be important for membrane stress protection, as the expression of Vipp1ΔH7 in a Vipp1 knockout strain of *A. thaliana* reduced the heat-stress tolerance of the plant compared to wild type (Zhang et al., 2016a). Finally, an *in vitro* study found that binding of Vipp1 to PG liposomes increased membrane rigidity and raised the phase transition temperature (Heidrich et al., 2016).

1.3.2.3 Membrane fusion

Several *in vitro* experiments, including membrane fusion assays, nanoparticle tracking and EM, have indicated that Vipp1 can mediate liposome fusion in the

presence of Mg^{2+} (Hennig et al., 2015). It was proposed that Vipp1 could be playing a similar role *in vivo*, mediating membrane fusion between the thylakoid membrane and the plasma membrane in cyanobacteria or chloroplast inner membrane in algae and plants (Heidrich et al., 2017). In the presence of Mg^{2+} ions *in vitro*, two Vipp1 rings were shown to attach to each other and form a double ring structure. Based on the occurrence of ''bottom-connected'' Vipp1 double rings, the bottom of the Vipp1 ring was predicted to initiate membrane binding and fusion (Saur et al., 2017). Because membrane fusion requires a severe alteration of membrane curvature, it was suggested that binding of different sized Vipp1 rings contributes to a certain flexibility of the membrane. A question has been raised about whether Vipp1 directs membrane fusion or whether membranes fuse in an uncontrolled way due to membrane destabilization caused by Vipp1 (Wolf, 2017).

In vivo, when plant cells were transferred from dark to light growth conditions, a large rearrangement of thylakoid membranes occurs. This transition is correlated with increased Vipp1 puncta formation (Figure 2G-J) (Bryan et al., 2014; Chuartzman et al., 2008; Kenneth Hoober et al., 1991; Kóta et al., 2002). Therefore, it was proposed that Vipp1 might also play a role in the reorganization of existing membranes.

1.3.3 Mg^{2+}, a potential cofactor of Vipp1

Mg^{2+} ions are the most abundant metal ions in the plant cytosol (Shaul, 2002). In the chloroplast stroma, the availability of Mg^{2+} regulates chloroplast metabolism by serving as a cofactor to a host of enzymes. Moreover, stromal Mg^{2+} availability is directly correlated with light conditions. (Ishijima et al., 2003; Lin and Nobel, 1971; Portis, 1981; Portis and Heldt, 1976). Mg^{2+} has been proposed as a cofactor of Vipp1-mediated liposome fusion (Hennig et al., 2015). While it is well established that Mg^{2+} binding can trigger conformational changes in proteins (Cox et al., 2005), direct binding of Mg^{2+} and its potential impact on Vipp1 oligomerization and membrane interaction has not been demonstrated. Since Vipp1 can bind to membranes in the absence of Mg^{2+} but membrane fusion only takes place in the presence of Mg^{2+} (Hennig et al., 2015), it was proposed that the binding of Mg^{2+} to Vipp1 rings may introduce a conformational change.

1.3.4 Vipp1 is proposed to have GTPase activity

Protein machineries that regulate intracellular membrane fusion and remodeling events at organelles such as the endoplasmic reticulum, Golgi and mitochondrion often have GTP binding and/or hydrolysis activity (Bonifacino and Glick, 2004; Montessuit et al., 2010; Youle and Van Der Bliek, 2012). Examples are the GTPase Atlastin, which mediates the homotypic fusion of endoplasmic reticulum membranes (Liu et al., 2015; Ohnishi et al., 2018; Park and Blackstone, 2010), dynamin, which is a component of the membrane fission machinery and requires GTP binding and GTPase activities (Liu et al., 2013), and members of the Rab or ARF/Sar branches of the Ras GTPase superfamily, which regulate intracellular vesicular transport (Mizuno-Yamasaki et al., 2012). Yet, very little is known about the membrane-remodeling machinery of the chloroplast.

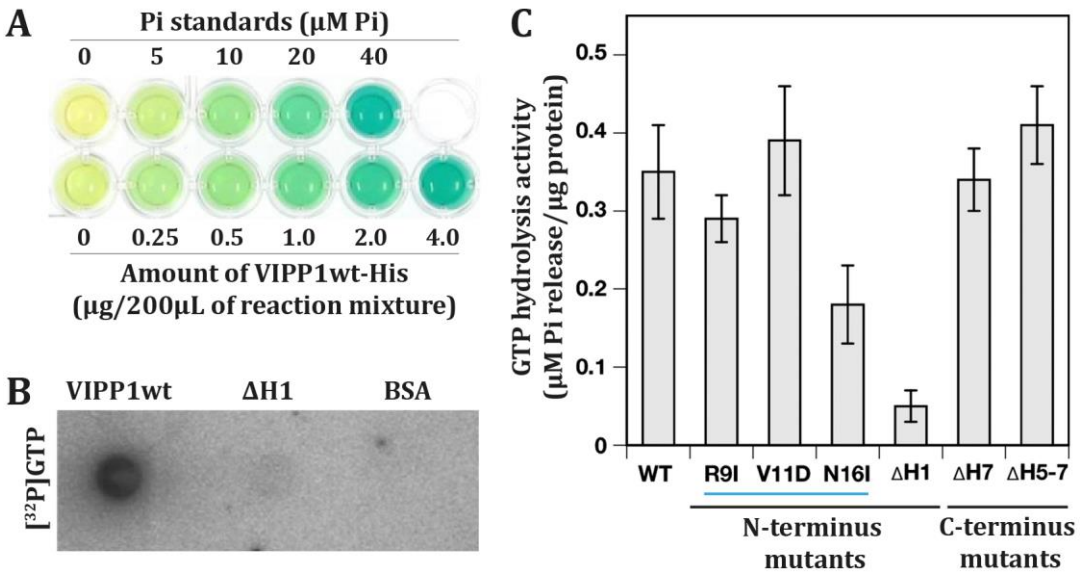

Figure 9: GTP hydrolysis activity of Vipp1.

A. Assay for AtVipp1 GTP hydrolysis activity using a GTPase assay kit (Innova Biosciences). Green denotes the presence of free inorganic phosphate (Pi). The upper row is a control reaction provided by the kit. The lower row shows the release of Pi due to the GTPase activity of Vipp1.

B. Direct binding of GTP to Vipp1-His protein via a dot-blot assay. Vipp1-His appears to be capable of binding GTP, whereas an N-terminally truncated version of Vipp1-His shows almost no signal, similar to the BSA control.

C. Testing the regions of Vipp1 that are necessary for its GTP hydrolysis activity. N-terminal Helix-1 is shown to be necessary for the GTPase activity, as opposed to C-terminal helices. The deletion of C-terminal Helix-7 does not affect the GTPase activity (A-C are modified from Ohnishi et al., 2018).

Recently, CPRabA5e was identified as a chloroplast-localized Rab GTPase protein in *Arabidopsis* (Karim et al., 2014). In addition, FZL (FZO-like), a new protein class within the dynamin superfamily, was suggested to function in chloroplasts as a membrane fusion protein (Gao et al., 2006). Interestingly, GTPase activity-dependent formation of punctate FZL-GFP structures near the chloroplast periphery was similar in appearance to Vipp1-GFP puncta (Gao et al., 2006; Zhang et al., 2012).

As Vipp1 is proposed to play a role in protecting membranes through fusion, it might also require GTPase activity. Supporting this idea, PspA from *E. coli* was found to have GTP hydrolysis activity (Ohnishi et al., 2018). Recent studies on AtVipp1 (Figure 9) have suggested that Vipp1 and PspA are a novel class of GTPase that lacks canonical G domains or tubulin/FtsZ-type G-box (Ohnishi et al., 2018). It was proposed that the GTP binding site on Vipp1 might be structured by oligomerization, similar to multimeric FtsZ (Scheffers et al., 2002). The N-terminal H1 of Vipp1 was shown to be important for GTP hydrolysis activity (Figure 9C), whereas the C-terminal H7 did not play a role in GTPase activity. This is consistent with the observation that PspA does not possess the C-terminal region yet is capable of hydrolyzing GTP. As H1 also participates in oligomer formation, oligomerization is proposed to be necessary for the GTP hydrolysis activity (Ohnishi et al., 2018).

1.4 Cryo-electron microscopy

1.4.1 Why electron microscopy?

One of the most widely used methods for obtaining near atomic-resolution structures of individual proteins and molecular complexes is X-ray crystallography. This method is limited by the requirement for successful crystallization from a high quantity of homogenous protein. Furthermore, crystal packing forces may distort the structures. Another method called nuclear magnetic resonance (NMR) does not require crystallization but also needs a large amount of isotopically-enriched sample. NMR is further restricted to small proteins or single domains (Frueh et al., 2013; Hennig and Sattler, 2014). Some of these challenges can be overcome by single-particle cryo-electron microscopy (cryo-EM), which allows near atomic-resolution structure determination of isolated molecular complexes frozen in a thin layer of vitreous ice. Cryo-EM is suitable for a wide range of sample sizes, from large multi-MDa complexes such as proteasomes (Schweitzer et al., 2016; Wehmer et al., 2017) and ribosomes (Hashem et al., 2013; Liu et al., 2017), to complexes that are smaller than 100 kDa (Fan et al., 2019; Herzik et al., 2019; Khoshouei et al., 2017). Cryo-EM is also more practical for studying proteins that are difficult to isolate, as only a small amount of sample is needed. Recent advances in instrumentation and software have dramatically improved the resolving power of cryo-EM, while simultaneously greatly reducing the time required to acquire data and solve a structure (Bammes et al., 2012; Li et al., 2013; Ludtke, 2016; Milazzo et al., 2011; Nogales, 2016; Scheres, 2016). The automation of data acquisition, including the use of beam shift for multi-shot acquisition, now yields thousands of cryo-EM images per day (Cheng et al., 2018; Lyumkis, 2019). Real-time processing software sorts and pre-processes these images as they are saved off the microscope (Biyani et al., 2017; Tegunov and Cramer, 2019). Deep learning-based autopickers can be trained to automatically pick particles out of these micrographs, and advanced alignment software pushes ever better resolutions through a variety of particle-specific refinements (Tegunov and Cramer, 2019; Wagner et al., 2019). Heterogeneity of the sample can be dealt with successfully through 3D classification approaches such as principal component analysis and maximum likelihood (Sigworth, 1998), yielding multiple structures of different conformational states from one dataset.

The improvement in detector technology (see section 1.4.3, below) has not only led to higher-resolution 3D structures using smaller data sets, but has also lowered the size limit of the samples (Herzik et al., 2019; Khoshouei et al., 2017; Liu et al., 2019; Merk et al., 2016) and even led to the identification of rare conformational states (Fernández et al., 2013; Wehmer et al., 2017).

While single-particle cryo-EM enables near atomic-resolution structural studies of isolated complexes, cryo-electron tomography (cryo-ET) enables structural studies of complexes within their native cellular environment (Albert et al., 2017; Asano et al., 2015; Guo et al., 2018; Rast et al., 2019). Although the resolutions achieved by cryo-ET are more moderate (typically 10-20 Å), examining molecular complexes within the cell provides context to these structures and can lead to the discovery of novel interactions.

1.4.2 Electron-specimen interaction

Electrons can undergo either elastic or inelastic scattering upon interacting with the specimen (Reimer and Kohl, 2008). Elastic scattering is mostly due to the electrostatic interaction between the incident electron and the nucleus of the specimen atom. The higher the atomic number of a specimen atom and the closer the electron passes by the nucleus, the larger is the angular deviation of the electron from its incoming direction. Inelastic scattering is due to the interaction of the incoming electron with electrons of the specimen atom and results in energy deposition in the specimen. This can lead to the radiation damage of the biological sample (Reimer and Kohl, 2008; Williams and Carter, 2009).

The two most common EM methods are Scanning Electron Microscopy (SEM) and Transmission Electron Microscopy (TEM). In SEM, backscattered and secondary electrons are used to reproduce the surface topology of the biological specimen (Goldstein et al., 2003). In TEM, on the other hand, electrons are detected after they have passed through the specimen, creating a projection image that provides details about the internal structure of the specimen (Frank, 2010). TEM imaging is generally performed under high vacuum conditions. To avoid the evaporation of the biological specimen, sample immobilization is required. Classical fixation methods such as heavy

metal staining and plastic embedding are harsh and introduce numerous sample artifacts that distort structures and limit resolution. In contrast, cryo-EM samples are rapidly frozen by plunging into liquid ethane (−210 °C), which preserves the specimen in non-crystalline vitreous ice that is suitable for high-resolution imaging (Dubochet et al., 1982; Lučić et al., 2005). However, these frozen samples are also highly sensitive to damage from the electron beam.

1.4.3 The transmission electron microscope

A transmission electron microscope consists of a large column, with an electron gun positioned at the top (Figure 10). For high-resolution imaging, a highly coherent beam of electrons is required, which is provided by a field emission gun (FEG). Generally, the voltage used to accelerate the electrons is 120-300 kV. The electron microscope is operated under a high vacuum condition ($\sim 10^{-10}$ bar) to prevent interaction between electrons and gas molecules that would add noise to the TEM images. Further down the column, electromagnetic lenses and apertures allow manipulation of the electron beam. The condenser lenses C1 and C2, and the corresponding apertures, provide parallel illumination on the microscope's stage. An EM grid, holding the specimen of interest, is maneuvered on the stage using a computerized goniometer. The goniometer allows precise adjustment of the grid's position in x, y and z, and is also used to tilt the grid up to 70°. Electrons either simply pass through the specimen without interacting or scatter after interacting with the specimen atoms. The objective aperture filters out electrons that have been scattered at a high angle, followed by two additional lenses that enlarge the projection image (Williams and Carter, 2009).

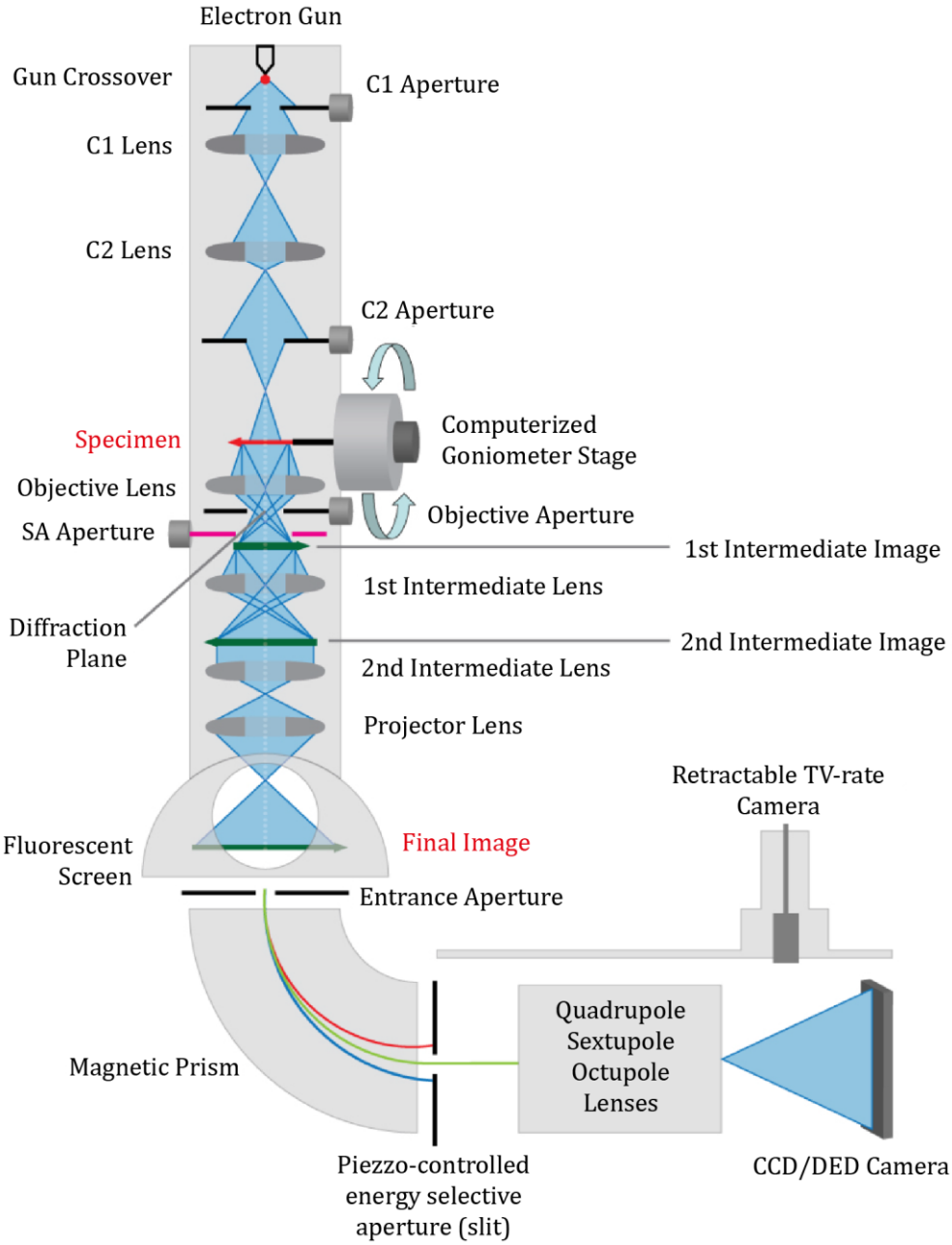

Figure 10: Schematic overview of a transmission electron microscope with the beam path illustrated in blue (modified from Kochovski, 2014).

With increasing thickness of the biological specimen, the percentage of inelastically scattered electrons also increases. Due to the chromatic aberration of electromagnetic lenses, inelastically scattered electrons do not add to the signal of the image. Energy filters use “zero-loss filtering” to remove these inelastically scattered electrons that have lost energy, dramatically improving the image quality of thicker specimens (Krivanek et al., 1995). In the past, the final image was recorded on

photographic film, but in modern microscopes, it is recorded by a digital detector (Li et al., 2013; Ruskin et al., 2013).

Traditionally, electron micrographs were recorded on photographic film. The introduction of CCD (charge-coupled device) cameras made the data collection much more convenient. However, CCDs have several disadvantages, including low signal-to-noise ratio (SNR) and the inability to correct for drift. In these cameras, incoming electrons are first converted into photons by a scintillator, and these photons are then recorded by the CCD chip. This conversion spreads out the signal and introduces additional noise to the final images (McMullan et al., 2014). Several years ago, CMOS direct electron detection cameras (DEDs) were introduced, dramatically increasing the resolution of cryo-EM. DEDs offer several advantages over CCD cameras: (1) by detecting electrons directly with sub-pixel accuracy, DEDs significantly improve the SNR compared to CCDs. (2) DEDs offer improved detective quantum efficiency (DQE), in particular for the high spatial frequencies corresponding to high-resolution information (McMullan et al., 2014; Ruskin et al., 2013). (3) The fast readout of CMOS chips allows multiple sub-frames to be captured for each image. These stacks of sub-frames are then computationally aligned to correct for drift caused by stage instability and beam-induced motion, reducing image blur and recovering fine details (Li et al., 2013). For the work described here, data was acquired with the Gatan K2 Summit. This DED camera operates in 'counting mode', precisely localizing single incoming electrons and suppressing electronic noise (Kuijper et al., 2015).

Two different imaging modalities, single particle cryo-EM and cryo-electron tomography (cryo-ET), can be used to study the 3D structures of macromolecules.

1.4.4 The principle of single-particle cryo-EM

The single-particle cryo-EM method is used to determine near-atomic resolution structures of isolated macromolecules such as protein complexes, ribosomes and viruses (Frank, 2010; Glaeser, 2019; Lyumkis, 2019). Purified molecular complexes are vitrified within a thin film of amorphous ice on an EM grid. This grid is then imaged at high magnification in a transmission electron microscope,

yielding thousands of 2D projection images, called 'micrographs'. Each micrograph can contain up to several hundred copies of the macromolecule, ideally oriented randomly, thus sampling many different orientations of the structure. To avoid excessive beam damage, low electron dose is used to acquire these micrographs (Cheng, 2015), which leads to poor SNR. New methods such as dose fractionation combined with motion correction have significantly improved the data quality (Cheng, 2015; Li et al., 2013).

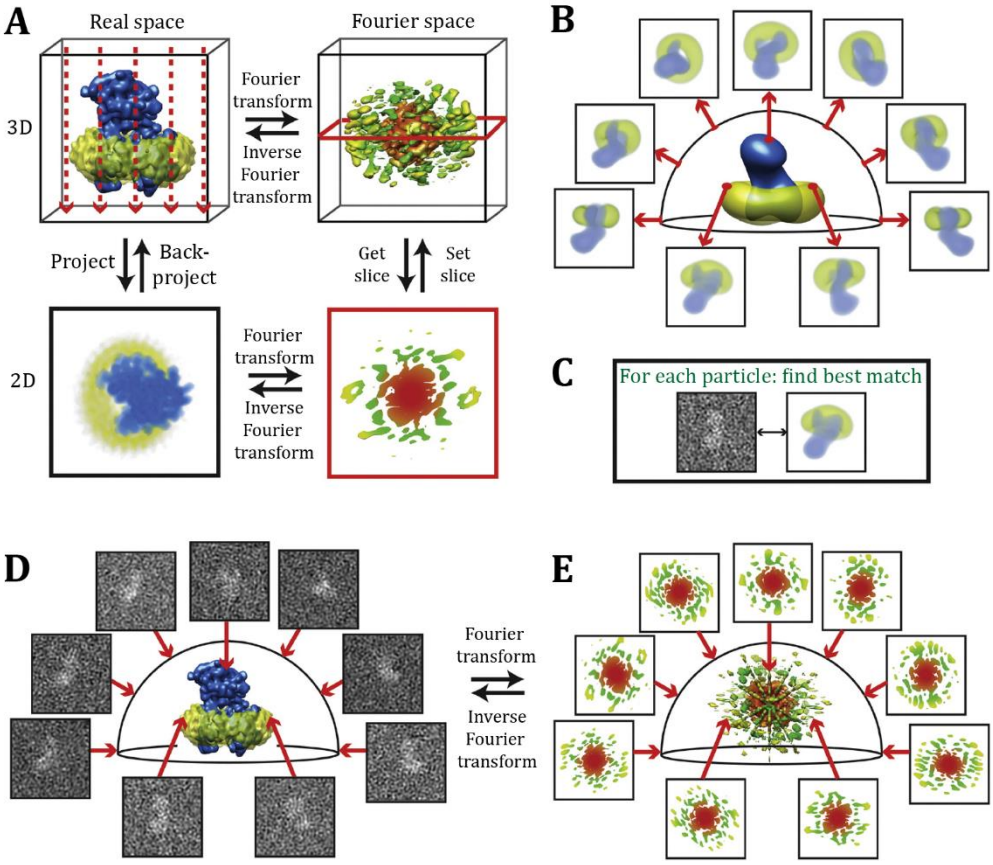

Figure 11: Basic concepts of single-particle cryo-EM (modified from Nogales and Scheres, 2015).

A. The projection-slice theorem states that the 2D projection of a 3D object in real space (left) corresponds to a central 2D slice of the same object in Fourier space (right). The real-space projection direction (left, dashed red arrows) is perpendicular to the Fourier slice (right, red frame).

B. In a 3D reconstruction process, many 2D projections of the same object can be combined through an iterative process called 'projection matching'. Reference projections of a 3D object are calculated in all directions to help determine the relative orientations of the experimental 2D projections.

C-D. Next, each experimental projection image is compared to all the reference projections to find the best match. As a result, all the experimental projections are oriented to the reference 3D structure.

E. A 3D reconstruction can be calculated by positioning many 2D slices (the 2D Fourier transforms of all experimental projections) into the 3D transform and calculating an inverse transform. Iterating steps B–E will gradually improve the particle orientations, and hence the resolution, of the 3D reconstruction.

In the next step, 2D projections of individual macromolecules (referred to as 'particles') are extracted from the micrographs via automated procedures such as Gautomatch (Scheres, 2016) and SPHIRE-crYOLO (Wagner et al., 2019). Thousands of these 2D projections are then averaged together, sampling different orientations and boosting SNR to generate a high-resolution 3D reconstruction. The projection-slice theorem (also known as the central slice theorem) explains how 2D projections of a 3D object can be combined to obtain a 3D reconstruction (Figure 11A). According to this theorem, each 2D projection corresponds to a slice of that 3D molecule in Fourier space in a direction perpendicular to the slice (Van Heel et al., 2000; Nogales and Scheres, 2015).

Each projection image contains limited information. Therefore, to reconstruct a 3D volume, projections from many different directions are required. The projection direction of each particle is determined through an optimization-based alignment called 'projection matching'. Five parameters, also known as 'pose parameters', must be optimized for each particle: the three Euler angles (Φ, Ψ and Θ), which describe the projection direction and in-plane rotation, as well as the x- and y-shifts (Frank, 2010; Sigworth et al., 2010; Sorzano et al., 2006). During projection matching, all particles are compared to 2D projections from different orientations of a 3D reference model (Figure 11B-E). The cross-correlation values from the matching are then used by probabilistic maximum likelihood algorithms to assign particles to a specific projection of the reference. Iterative rounds of projection matching are performed using an updated 3D reference model in each round to refine the pose parameters of the projections until the maximum likelihood probability converges.

The final resolution of the 3D reference mainly depends on the SNR, which improves as more particles are added to the reconstruction, and well-defined particle orientations (pose parameters). The resolution of the average is evaluated by 'gold standard' Fourier Shell Correlation (FSC), which has been implemented in RELION 3.0 (Rosenthal and Henderson, 2003; Zivanov et al., 2018). For the gold standard FSC, the particles are randomly separated into two half sets and processed independently, resulting in two reconstructions. These two reconstructions are then compared at different resolutions to provide a score of self-consistency at each resolution (Scheres,

2012; Zivanov et al., 2018). An FSC cut-off of 0.143 is frequently used to assign a numerical resolution value to a structure.

The resolution of 3D reconstructions is limited by the flexibility and conformational heterogeneity of the target macromolecule. Averaging over different conformations leads to smearing out of the resulting density. This problem can be solved by applying 3D classification to segregate particles into classes based on different symmetries or conformational states. Following classification, refinement proceeds independently for each class, yielding multiple high-resolution averages (Wang et al., 2013).

Single-particle data acquisition is carried out under 'low dose' conditions. This is accomplished by automating three iterative steps: tracking, focus, and exposure. Often, regularly spaced holes with a fixed diameter (e.g., Quantifoil grids) are used for high throughput data collection. Due to the identical geometry of the imaging areas, the tracking step is able to center the current foil hole by comparing the tracking image to a pre-defined reference image. Focusing is carried out on the carbon support foil, 2 micrometers away from the exposure center. In the exposure state, the image is recorded towards the center of the foil hole (Cheng et al., 2016; Gerlach et al., 2018; Schorb et al., 2019; Schuller et al., 2018). The newly developed 'multishot' data acquisition scheme greatly increases the speed of data collection by using beam tilt instead of stage movements to record multiple exposure images for each tracking and autofocus step (Cheng et al., 2018; Lyumkis, 2019).

1.4.4.1 Contrast transfer function (CTF)

In TEM imaging, the original mass distribution of the macromolecule is distorted by the CTF, a Fourier-based description of how the objective lens modulates information in a resolution-dependent way (Penczek et al., 2018). The CTF flips the phases in resolution ranges that depend on the applied defocus, and the 'envelope function' dampens high-resolution information (Frank, 2010). The CTF results from spherical aberration (Cs), an imperfection of the objective lens, along with the envelope function caused by incoherence of the electron beam (Zhou and Chiu, 1993).

CTF correction is commonly applied to cryo-EM images. The goal of CTF correction is to recover positive amplitude values in the Fourier transform of the image. The CTF is determined by fitting the observed Thon rings in the power spectrum of the projection image (Mindell and Grigorieff, 2003; Zhou et al., 1996). Thon rings are the rings in the power spectrum of an electron micrograph reflecting the maxima/minima and zero transitions in the CTF. The spacing of the Thon rings is determined by the defocus of the image. Programs such as CTFFIND4 fit a model to the Thon rings (Rohou and Grigorieff, 2015), and the correction is most commonly accomplished by 'phase flipping' the negative amplitudes to positive values (Downing and Glaeser, 2008; Zubelli et al., 2003). The Volta phase plate is another tool that can be used to increase the image contrast by modulating the CTF to produce a high signal in the low frequency range (Danev and Baumeister, 2016; Danev et al., 2017; Khoshouei et al., 2016).

1.4.5 The principle of cryo-electron tomography

Cryo-ET has provided unprecedented insights into the native molecular organization of the cell (Albert et al., 2017; Asano et al., 2015; Bykov et al., 2017; Engel et al., 2015; Guo et al., 2018; Weiss et al., 2019). Freezing in vitreous ice preserves cellular features in their native state, avoiding staining and chemical fixation artifacts. Cryo-ET has been widely used to study isolated macromolecular assemblies, and cellular organelles (Beck et al., 2004; Davies et al., 2014; Gold et al., 2014; Nicastro et al., 2000; Schur et al., 2016). Previously, cryo-ET of intact cells was limited to small prokaryotes and the periphery of eukaryotic cells, which are thin enough to be transparent to the electron beam (Brandt et al., 2010; Lučić et al., 2005; Medalia et al., 2002; Oikonomou and Jensen, 2017). With the application of focused ion beam milling to cryo samples (Rigort et al., 2012; Schaffer et al., 2017), it is now possible to image the interior of eukaryotic cells with molecular resolution (Albert et al., 2017; Bykov et al., 2017; Guo et al., 2018; Mahamid et al., 2016). Recent developments in correlative light microscopy aid in locating features of interest hidden deep within the cell, which can then be targeted with the focused ion beam (Arnold et al., 2016).

In cryo-ET, the specimen is tilted along an axis perpendicular to the direction of the electron beam, and a set of 2D projection images (called a tilt series) is acquired. These 2D projections are then computationally aligned and merged to obtain a 3D volume called a tomogram. Tilt series are generally limited from −60° to +60° (with 2° or 3° increments) due to physical restrictions of the instrumentation and increased sample thickness at the high tilts. Therefore, information about the sample at high tilts is missing in the final tomogram. This missing information is called the 'missing wedge' due to its characteristic shape in Fourier space. The missing wedge causes anisotropic resolution, with blurred and delocalized features along the direction of the electron beam.

Biomolecules are radiation sensitive. In TEM, electron dose is represented in terms of the number of electrons that hit each square Angstrom of the sample ($e^-/Å^2$) (Elmlund and Elmlund, 2015; Nogales and Scheres, 2015). To limit sample damage, the cumulative dose is usually kept around 100 $e^-/Å^2$ (Lučić et al., 2005). By automation of all the necessary steps, the electron dose applied to the specimen can be reduced to a minimum. This procedure, known as 'low dose' acquisition (Koster et al., 1997), consists of four steps: (i) tilt the sample, (ii) re-center the position by acquiring a tracking image and correlating it with the previous tilt, (iii) adjust the defocus by acquiring and correlating a pair of projections with different beam tilts, and (iv) acquire the projection image for the tilt series.

Three different tilt schemes have been implemented for tomogram acquisition (Hagen et al., 2017). In the unidirectional approach, an undivided tilt series is acquired starting at -60° and proceeding toward +60°. The unidirectional scheme is good for fast acquisition, but it deposits the initial electron dose on high tilts, where resolution is limited. As a result, this scheme is not well suited to high-resolution structure determination. In the bidirectional approach, tilt series are acquired in two halves, usually separated at 0° or 20°. The two halves are then merged to form a full tilt series from -60° to +60°. This method better distributes the initial dose on the lower tilt images and therefore is able to retrieve more high-resolution information. However, alignment of the two halves of the tilt series is prone to errors due to distortion of the sample caused by accumulated dose. A third approach, called dose-symmetric acquisition, optimally distributes the initial dose by starting at 0° and then alternating

between positive and negative tilts as acquisition proceeds towards +/-60° (Hagen et al., 2017). This tilt scheme is ideal for high-resolution structure determination, but it does require significantly more time due to stage settling when moving between high positive and negative tilts.

Before tomogram reconstruction, the projection images at each tilt need to be aligned to a common coordinate system. Two methods have been developed for this purpose. The first method is alignment based on high-density fiducial markers such as 10 nm gold, which are added to the sample before vitrification (Amat et al., 2010). The second method is 'patch tracking', where alignment is performed using the image-based cross-correlation of small patches that are tiled through the tilt series (Kremer et al., 1996; Mastronarde, 1997). This method tends to be less accurate than fiducial markers, but it is often the only option for cellular cryo-ET, where fiducial markers are not present in the sample. Following tilt series alignment, the tomogram is most commonly generated using weighted back-projection, where aligned 2D projections are projected in Fourier space in accordance with the projection-slice theorem to form a 3D reconstruction (Lučić et al., 2005; Radermacher, 2006).

As mentioned above, low SNR and the missing wedge are limiting factors in obtaining high-resolution information from tomographic data. One solution is sub-tomogram averaging.

1.4.5.1 Subtomogram averaging

The goal of subtomogram averaging is to increase the SNR and compensate for the missing wedge by combining multiple sub-volumes containing different orientations of a structure of interest (Briggs, 2013; Walz et al., 1997). First, multiple copies of the structure of interest must be located within the tomograms. This is accomplished either manually or computationally by using a cross correlation-based pattern recognition algorithm called 'template matching' (Förster et al., 2010). Many orientations of the reference structure are searched through each voxel of the tomogram. The highest cross-correlation values indicate the best matches between the reference and the tomogram. Once positions of these sub-volumes are obtained, they are extracted and then iteratively aligned and averaged until convergence. Procedures

such as dose weighting (low-pass filtering of later tilts) and CTF correction further increase SNR and the resolution of the final average (Grant and Grigorieff, 2015).

2 Aim of this work

Vipp1, an essential protein in the plant kingdom, was first identified more than two and a half decades ago. This protein forms defined structural assemblies that resemble barrels and tubes *in vitro*. It is not known yet whether the same is true inside the cell. Several roles have been proposed for Vipp1, including thylakoid biogenesis, vesicle formation, and stress resistance. However, the defined physiological functions of the Vipp1 are not yet known. Moreover, no information is available on whether Vipp1 oligomerization is related to its function. Despite its crucial importance in photosynthetic life, the molecular structure of Vipp1 and the mechanism of its assembly into rings and rods are not understood. To address the structure, a negative stain EM single-particle study of SynVipp1 was conducted recently. However, due to inherent limitations of the negative stain EM method, the quality of the 3D structure was limited and no information about the molecular assembly of Vipp1 could be extracted. On the functional side, due to its strong affinity for lipid, Vipp1 was proposed to bind to membranes and participate in vesicle transportation among other functions.

The scope of this work is to address both functional and structural aspects of Vipp1 with the following two aims:

Aim1: To explore the proposed function of Vipp1 in lipid binding using cryo-electron tomography and subtomogram averaging. We studied Vipp1 protein from the green alga *Chlamydomonas reinhardtii* (CrVIPP1), which predominantly assembles into extended hollow rods.

Aim2: To resolve the molecular architecture of Vipp1 at near-atomic resolution using single-particle cryo-electron microscopy. We studied Vipp1 protein from the cyanobacterium *Synechocystis sp. PCC 6803* (SynVipp1), which predominantly assembles into barrel-like rings.

3 Materials and methods

3.1 Negative stain EM

In negative stain techniques, the biological specimen is stained with heavy metal salts such as uranyl acetate, which generates a cast around the object. This cast scatters electron more strongly that the biological specimen, providing resistance to electron damage and generating strong contrast (Boekema et al., 2009; Brenner and Horne, 1959; Hall et al., 1945; Huxley and Zubay, 1961). 5 µL of the sample was applied to glow discharged, 200 mesh copper grids (G2200C, Plano GmbH) that had been coated with homemade carbon film. The sample was incubated for 2 min, blotted, washed three times with water, and then stained with 2% uranyl acetate for 30 sec. Images were recorded using an FEI Tecnai F20 FEG microscope operated at 200 kV with an FEI Eagle CCD camera, a magnification of 50,000 × (2.21 Å per pixel) and a defocus range of -2 to -5 µm. Measurements of negative stain images were performed with IMOD (Kremer et al., 1996) and ImageJ (Schneider et al., 2012) software packages.

3.2 Cryo-electron tomography

3.2.1 Grid preparation and data acquisition

Cryo-EM grids were prepared with fresh protein that had not been freeze-thawed. 4 µL of sample (Prep #2 for Vipp1 alone and Prep #4 for Vipp1 mixed with 4 mM 95:5 PC:PI4P liposomes) and 1 µL of 10 nm colloidal gold suspension were applied together to glow discharged, holey carbon-coated copper grids (R 2/1, 200 mesh, Quantifoil Micro Tools, Jena, Germany). Grids were plunge-frozen in a liquid ethane/propane mixture using a Vitrobot Mark 4 (Thermo Fisher, FEI). Blotting chamber conditions were set to 4 °C and 95% humidity, and grids were blotted using blot force 10 and a blot time of 8 s. Grids were stored in liquid nitrogen until usage. Tomograms were acquired on an FEI Titan Krios at 300 kV, using a post-column energy filter (Quantum, Gatan) and a K2 Summit direct electron detector (Gatan) operated in

counting mode at 12 frames per second and a calibrated pixel size of 3.42 Å. Tilt series were recorded with SerialEM software (Mastronarde, 2005) using a bidirectional tilt scheme from 0° to ± 60°, with 2° tilt increments, a defocus range of -5 to -6 µm, and a total accumulated dose of ~100 $e^-/Å^2$.

3.2.2 Tomogram reconstruction

Frames from the K2 camera were aligned with MotionCor2 (Zheng et al., 2017) using 3 × 3 patches. Tilt series were aligned with the IMOD software package (Kremer et al., 1996) using fiducial-based tracking, or image-based patch tracking when not enough 10 nm gold particles were present in the images. Tomograms were reconstructed with weighted back projection.

3.2.3 Subtomogram averaging

The subtomogram analysis was performed with 4x binned data (pixel size of 1.368 nm). In IMOD, the long axes of Vipp1 rods were roughly defined by manually placing points along the center of each rod. These central points were used to generate a spline representing the rod axis. A tubular grid was then generated as a set of points with a radial distance from the spline. The initial grid spacing was ~5.5 nm, which was chosen to oversample the underlying asymmetric units. Grid points were then used as subtomogram positions, and initial Euler angles were generated from the relative orientation of the particle with respect to the central spline. Subtomograms were extracted with a box size of ~87.6 nm. For rods with larger diameters (e.g., 56 nm and 61 nm), the box size of the subtomograms was ~129 nm. Subtomogram averaging was performed with scripts derived from TOM (Nickell et al., 2005), AV3 (Förster et al., 2005) and Dynamo (Castaño-Díez et al., 2012). An initial reference was generated using geometrically-defined Euler angles, which produced a cylindrically averaged tubular section. From there, a six-dimensional search was performed to refine Euler angles and Cartesian shifts, resulting in a low-resolution structure; this reference was used to align the full data set. Initially, half of the rod (defined radially) was masked to perform a local search for ten iterations. From cross-correlation and visual analysis, bad subtomograms were identified and discarded. Alignments converged after four

iterations. The averaged structure of the rod after the fourth iteration was used a new reference, and a new cylindrical mask was created. Further averaging was performed for six more iterations. To resolve the averaged structure radially, rather than doing a local search, a global search was performed using the entire rod. This alignment started with the averaged structure after the fourth iteration as a reference and performed six more iterations. These final averaged structures of individual rods were used to measure the geometric parameters plotted in Figure 18.

3.2.4 Measurement of Vipp1 subtomogram averages

Geometric parameters were measured for the average of each rod as follows: *Number of striations:* Using UCSF Chimera (Pettersen et al., 2004), the number of striations was counted from the cross-section of the average (Figure 16 and Figure 17).

Rod diameter and rod-liposome distance: Rod diameter was measured using radial EM density distribution plots, which were generated by converting the Cartesian volumes to polar cylindrical coordinates and averaging along the azimuthal direction and the rod's long axis. The diameter was defined as the distance between the outer surfaces of the rod, measured across the rod's cross-section (as diagrammed in Figure 18C). The rod-liposome distance was measured as the distance between the center point of the engulfed liposome's membrane bilayer and the center point of the outer Vipp1 rod's protein density.

Helical pitch: The pitch of a helix is defined as the distance along the helical axis (the long axis of the Vipp1 rod) to complete one turn (as diagrammed in Figure 18D). In other words, the pitch is the rise of one full turn. In the Cartesian space volume, two random points were chosen on a single striation of the averaged Vipp1 rod. The helical rise was measured as the distance between the two points parallel to the rod's long axis. The rotation angle was measured as the angle between the points, projected on the X.

3.3 Single-particle cryo-EM

3.3.1 Data acquisition

Cryo-EM grids were prepared with freshly purified protein. 4µL of the protein was applied to glow discharged, holey carbon-coated copper grids (R 2/1, 200 mesh, Quantifoil Micro Tools, Jena, Germany). Grids were plunge-frozen in a liquid ethane/propane mixture using a Vitrobot Mark 4 (Thermo Fisher, FEI). Blotting chamber conditions were set to 4 °C and 95% humidity, and grids were blotted using blot force 10 and a blot time of 10 s. Grids were stored in liquid nitrogen until usage. Images were acquired on an FEI Titan Krios at 300 kV, using a post-column energy filter (Quantum, Gatan) and a K2 Summit direct electron detector (Gatan) operated in counting mode. For each image, 80 frames were acquired over 8 sec, with a total dose of ~45 $e^-/Å^2$ and a calibrated pixel size of 1.35 Å. A total of 8120 images were recorded, using a defocus range of -0.5 to -3.5 µm.

3.3.2 Image processing and data analysis

Beam-induced sample motion and radiation damage were corrected by frame-alignment and dose-filtering using MotionCor2 (Zheng et al., 2017). The summed and dose-weighted micrographs were used for further processing. Particles were selected using CrYOLO, a program that uses machine learning for automated particle picking (Wagner et al., 2019). Here, a small training dataset of 80 images was used to train the program and then applied to the whole dataset of 8120 micrographs. All subsequent image processing was carried out using the RELION 3.0 software suite (henceforth referred to as RELION) (Zivanov et al., 2018). CTF parameters were determined and per-particle refinement was performed using Gctf (Zhang, 2016). 337K particles were extracted (defined as Dataset-A). After particle extraction, the dataset was cleaned using reference-free 2D classification to remove non-particle candidates such as ice contamination and broken particles. 2D classification is based on the assumption that noise has a random distribution and the features of the particles have identical signal. 263K particles were obtained (defined as Dataset-B).

The cleaned 2D classes were combined and further subjected to reference-free initial 3D model generation. In 3D alignment, the relative orientations of the 2D projections are unknown and must be determined computationally. As described in the projection-slice theorem, these particles were compared with computationally-generated projections of a 3D reference structure in order to assign 3D positions and orientations to the particles (Penczek et al., 1994). This was done iteratively, and the local sampling rate was increased in each round (Figure 19). Further steps of classification and refinement are described in the results section 5.1.1 and Figure 19. Two 3D volumes were generated and compared by splitting the dataset into two halves and refining them completely separately ('gold standard'). The final refined density was further filtered to the correct resolution determined by the 'gold standard' FSC curve. In RELION, the procedure for B-factor sharpening and calculating masked FSC curves is called 'post-processing'. The B-factor (or temperature factor) describes the attenuation of structure factors by thermal mobility of the molecule atoms.

3.3.3 Particle polishing

Although large drifts at the level of sub-frames are corrected at the beginning of the processing workflow, the individual particles also show some specific motion. The RELION particle polishing algorithm tracked the motion trajectories of the individual particles in each image and fitted them to linear trajectories (Scheres, 2014). Per-frame B-factor and linear intensity factor were also estimated to account for accumulating radiation damage during acquisition. This was achieved by comparing the reconstructed half-maps from individual frames to the full-frame half maps (Bai et al., 2013). As a result, a new set of 'shiny' particles were generated with the spatial frequency contribution from each frame weighted according to their radiation damage (Figure 19). The shiny particles had a higher signal to noise ratio (SNR), which improves the alignment accuracy and typically yields a higher final resolution.

3.3.4 Modelling of Vipp1 into the EM density

The initial PDB structure of SynVipp1 was obtained by homology modeling of SynVipp1, starting with the available crystal structure of *E. coli* PspA (PDB: 4WHE) (Osadnik et al., 2015). Missing residues at the N-terminal helix and the entire C-terminus were modeled using the Rosetta framework in ModelMaker. The models were clustered using the k-means algorithm. For each symmetry, single subunits for each layer of the Vipp1 ring were segmented. Each of the clusters obtained was fitted into the segmented maps using interactive molecular dynamics flexible fitting (MDFF) (Trabuco et al., 2009). After MDFF convergence, the cross-correlation coefficient for the clusters was calculated, and the structure showing the highest correlation was used for subsequent steps. The modeled monomers were truncated at residue 220, as the C-terminal H7 and its long disordered linker was not resolved within the EM density map, presumably due to its highly dynamic nature (Figure 20F-G). Once subunits for each segment were fitted by interactive MDFF, the entire structure was created by applying the respective symmetry operation (C14, C15, C16, C17, and C18) on the model. The structure was then refined using MDFF and symmetry-adapted constraints to apply a harmonic potential to the symmetry-averaged positions of each individual Vipp1 subunit within the complete ring. After this refinement, the structures were re-symmetrized using six selected monomers, one from each layer of the Vipp1 ring. Finally, the structure was energy minimized using MDFF and the EM density map. To avoid overfitting, all operations were performed at a modest gscale of 0.3. The interaction network of Vipp1 monomers in the ring was analyzed in UCSF Chimera based on the distance of residues within the Vipp1 structure.

The initial prediction of a nucleotide binding site in SynVipp1 was carried out using the GTPbinder web server (Chauhan et al., 2010). Predicted conformations of the nucleotide were obtained by docking in AutoDock4. The highest scoring conformations were chosen for subsequent refinement. After identifying the conformations that might occur within the binding pocket, the nucleotide was replaced by a published structure obtained from the PDB (PDB Code: 5L4G). Refinement of the nucleotide binding pocket was performed using interactive MDFF in VMD at a gscale of 0.3 and manual adjustment of residue orientation.

3.3.5 Estimation of the distribution of rings and rods in SynVipp1 mutants

The point mutations we inserted into N-terminal Helix-1 caused some of the ring-forming SynVipp1 to assemble into rods. To roughly estimate the percentage of Vipp1 protein incorporated in rings and rods for each of the mutants, negative stain EM was performed as described in section 3.1. The dimensions of the negative stain micrographs were 4096x4096 pixels, with a pixel size was 0.184 Å. Therefore, each micrograph was a square with a side length of 754 Å (4096 pixels multiplied by 0.184 Å). The diameters of Vipp1 rings and rods were roughly 30-40 nm. Based on the Vipp1 dimensions, a grid spacing of 80 Å was chosen, yielding a grid map of 8x8 squares. One example quantification is shown in Figure 12. The 8x8 grid map was overlaid on each of the images, and the presence of rings and/or rods in each square was manually counted. For both rings and rods, if more than 20-30% of a structure was contained within a grid square, that square was counted. Rods frequently passed through several squares, resulting in multiple counts for one structure. Thus, the goal of this analysis was not to measure the relative abundance of ring and rod structures, but rather to estimate the percentage of Vipp1 protein incorporated into the two types of structures.

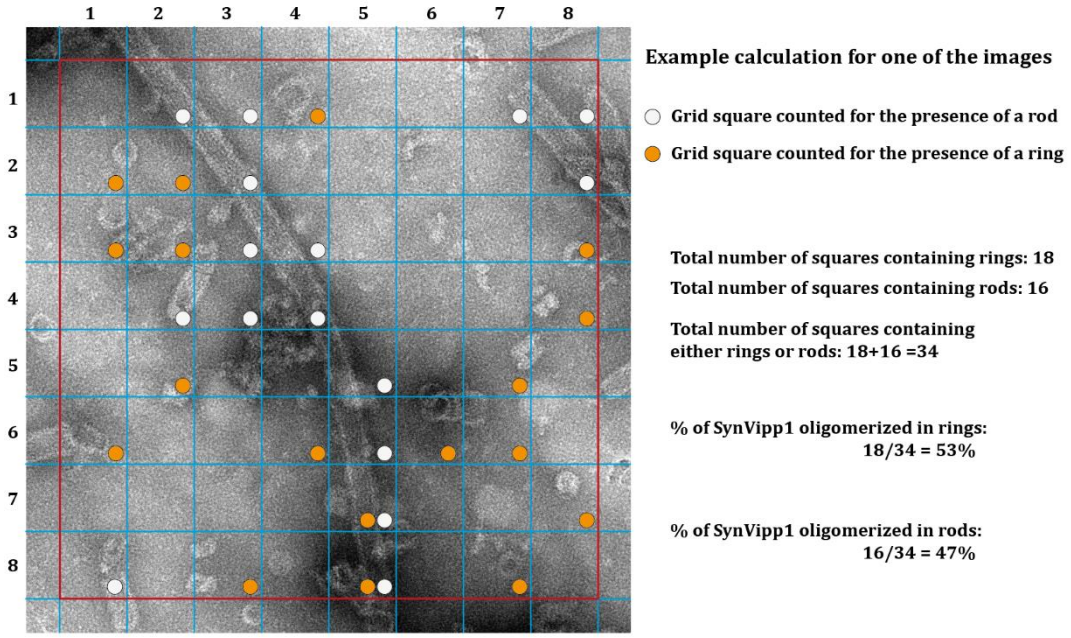

Figure 12: A grid-based approach to calculate the percentage of protein assembled into rings vs. rods in the SynVipp1 mutants. The border of the grid map is outlined in red. Individual grid squares are outlined in blue.

Results and discussion

4 crVipp1 rods engulf membranes containing phosphatidylinositol phosphates

The following results have been published (Theis et al., 2019) and were obtained in collaboration with the co-authors. Purified crVIPP1 protein was provided by Jasmine Theis and Prof. Michael Schroda (TU Kaiserslautern). Electron microscopy, image processing and the data analysis were performed by Tilak Kumar Gupta with the help of Benjamin Engel and William Wan (MPI Biochemistry). The following results are taken from the published manuscript (Theis et al., 2019).

4.1.1 Negative-stain electron microscopy reveals that *Chlamydomonas* Vipp1 forms rods that encapsulate lipids

Through biochemical experiments, our collaborator showed that *Chlamydomonas* Vipp1 (CrVipp1) binds strongly to phosphatidylinositol phosphates. Larger particles of Vipp1 were observed in TRF anisotropy and sucrose density gradient experiments when CrVipp1 were incubated with PC:PI4P (phosphatidylcholine:phosphatidylinositol-4-phosphates) liposomes. We wondered what structural changes occur when Vipp1 particles increase in size by interacting with liposomes, so we performed negative-stain electron microscopy of Vipp1 alone, Vipp1 incubated with pure PC liposomes, and Vipp1 incubated with PC:PI4P liposomes (Figure 13A-C). As observed previously, Vipp1 formed rings and rods under all conditions (Liu et al., 2007).

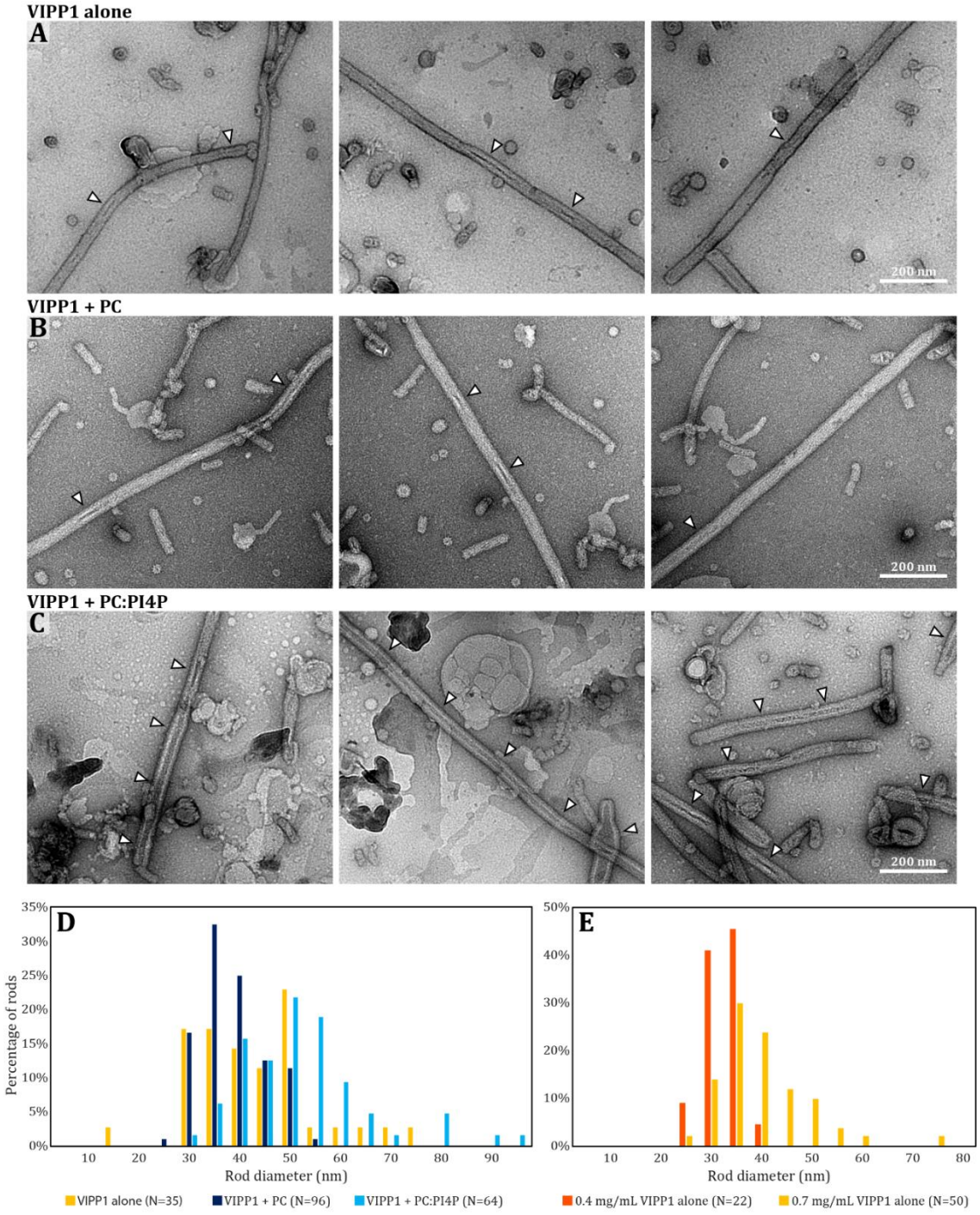

Figure 13: Vipp1 forms large rods that can contain lipids.

Negative stain electron micrographs of (A) Vipp1 alone, (B) Vipp1 incubated with PC liposomes and (C) Vipp1 incubated with PC:PI4P (95:5) liposomes. Vipp1 concentration was 0.4 mg/mL. Encapsulated stained material inside the Vipp1 rods is indicated with arrowheads. (D) Distribution of rod diameters for the three conditions shown in panels A–C. (E) Distribution of rod diameters for Vipp1 alone for two different Vipp1 preparations at concentrations of 0.4 mg/mL and 0.7 mg/mL (Preps #2 and #1, respectively, see methods). The 0.4 mg/mL sample was also used for the "Vipp1 alone" cryo-ET in Figs. 14, 16, and 18.

Interestingly, distinctly stained material was found encapsulated by these rods. Both in the absence of liposomes and when incubated with pure PC liposomes, Vipp1 rods occasionally contained short stretches of such material. In contrast, Vipp1 preparations incubated with PC:PI4P liposomes contained this material over long stretches within the rods. We reasoned that the encapsulated material in the Vipp1 preparations not incubated with liposomes represented endogenous *E. coli* lipids, as Vipp1 was purified under native conditions, and *E. coli* lipids have previously been observed in recombinant Vipp1 preparations (Otters et al., 2013). Pure PC liposomes apparently were encapsulated by Vipp1 rods with low efficiency, whereas PC:PI4P liposomes were encapsulated with high efficiency. Rod diameters only marginally increased in the presence of PC:PI4P liposomes (median of 42 nm for Vipp1 alone vs. 46 nm for Vipp1 + PC:PI4P liposomes; Figure 13D). This indicates that the distinct size increase seen after incubating Vipp1 with PC:PI4P liposomes in the sucrose density and TRF anisotropy experiments did not result from wider Vipp1 rod diameters. Rod diameters rather appeared to depend on the concentration of Vipp1 protein in the preparation, independent of liposome encapsulation (Figure 13E).

4.1.2 Preformed Vipp1 rods can engulf PI4P-containing liposomes, reminiscent of bubbles sucked up into straws

To better understand the molecular architecture of Vipp1 rods with encapsulated lipids, we employed cryo-electron tomography (cryo-ET) on Vipp1 alone and Vipp1 incubated with PC:PI4P liposomes. To our surprise, we found that Vipp1 rods apparently were not composed of stacked rings, as we have previously suspected from negative-stain EM images (Liu et al., 2007), but rather represent continuous tubules with striations visible in the surface views (Figure 14). PC:PI4P liposomes were squeezed inside the hollow Vipp1 rods, regardless of rod diameter, reminiscent of bubbles sucked up into straws (Figure 14E-K). We never observed an empty rod in this sample; every rod contained a liposome ($N > 100$). As the Vipp1 rods were preassembled prior to liposome addition, the liposomes were likely drawn into the rods by a strong interaction with the rod's inner surface until the entirety of the rod was filled, leaving the remainder of the liposome attached as a "bubble" on one end of the rod. These cryo-ET observations strongly suggest that the larger size of Vipp1 -

containing particles upon incubation with PC:PI4P liposomes was due to the engulfment of the liposomes. The specific nature of the interaction between the liposome and the inside of the Vipp1 rod can be inferred from Figure 14H, where only the outer membrane of a bi-lamellar liposome was sucked into the rod. In contrast, a small inner liposome was able to enter the rod because it is smaller than the rod's diameter (Figure 14J). Note that such cases were observed only rarely.

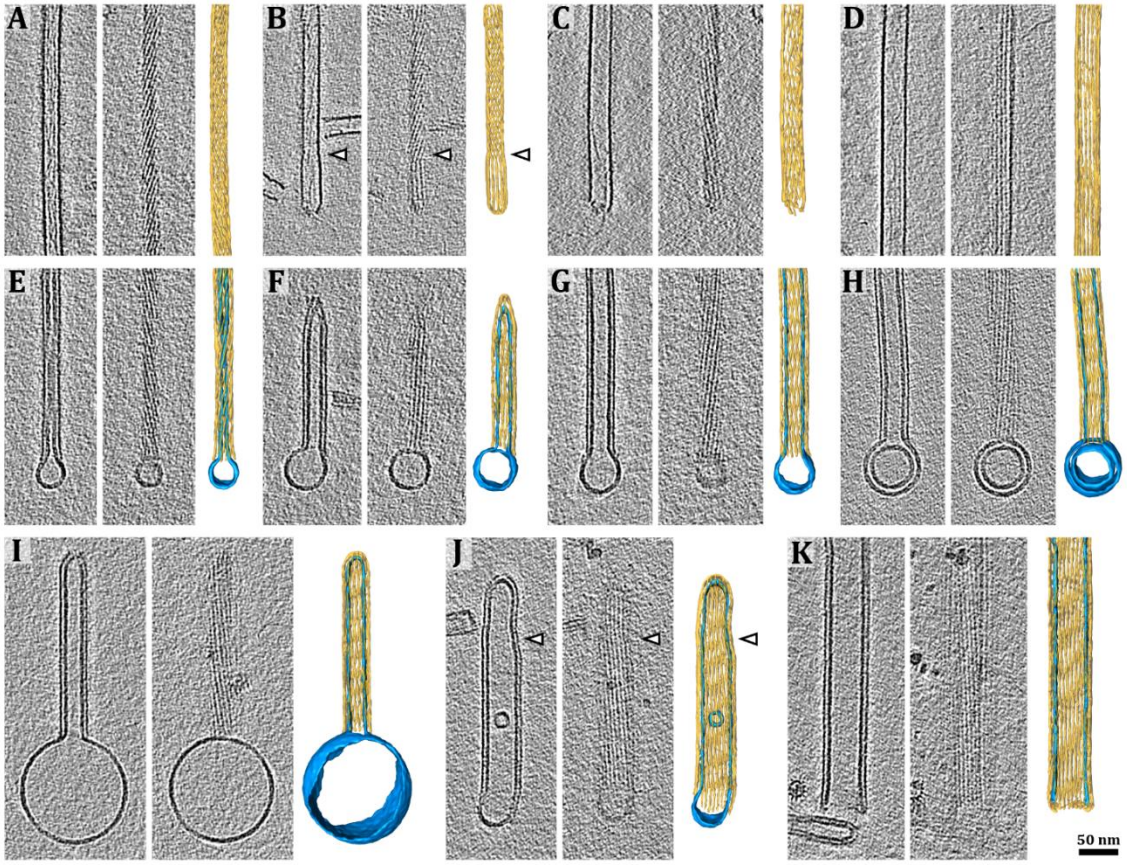

Figure 14: Cryo-electron tomography reveals that Vipp1 rods engulf PI4P-containing liposomes.

For each panel, the left image is a slice from the tomogram showing a central longitudinal section through the Vipp1 rod, the middle image is a slice from the tomogram showing either the top or bottom surface of the rod, and the right image is a 3D segmentation of the rod (yellow) and the liposome (blue). (A–D) Vipp1 rods alone and (E–K) Vipp1 rods incubated with PC:PI4P (95:5) liposomes. Arrowheads in B and J indicate where rods change diameter and helical pitch. The Vipp1 rods shown in (A–D) and (E–K) were from two different Vipp1 protein preparations (see methods).

Both with and without liposomes, the Vipp1 rods exhibited a range of diameters and helical pitches, which can change at discrete points along the rod (Figure 14B and J, and Figure 15). The Vipp1 concentration used in all of our experiments (0.3 to 0.7 mg/mL, see methods) was close to its physiological concentration: *Chlamydomonas* cells have a volume of ~270 μm^3 and contain ~20 pg protein (Hammel et al., 2018;

Weiß et al., 2000), leading to a cellular protein concentration of ~74 mg/mL. Vipp1 represents 0.05% of cellular protein (Liu et al., 2007), but is only present in the chloroplast stroma, which occupies around one fourth of the cell volume (half of the chloroplast) (Engel et al., 2015), yielding an estimated concentration of ~0.15 mg/mL Vipp1 in the stroma.

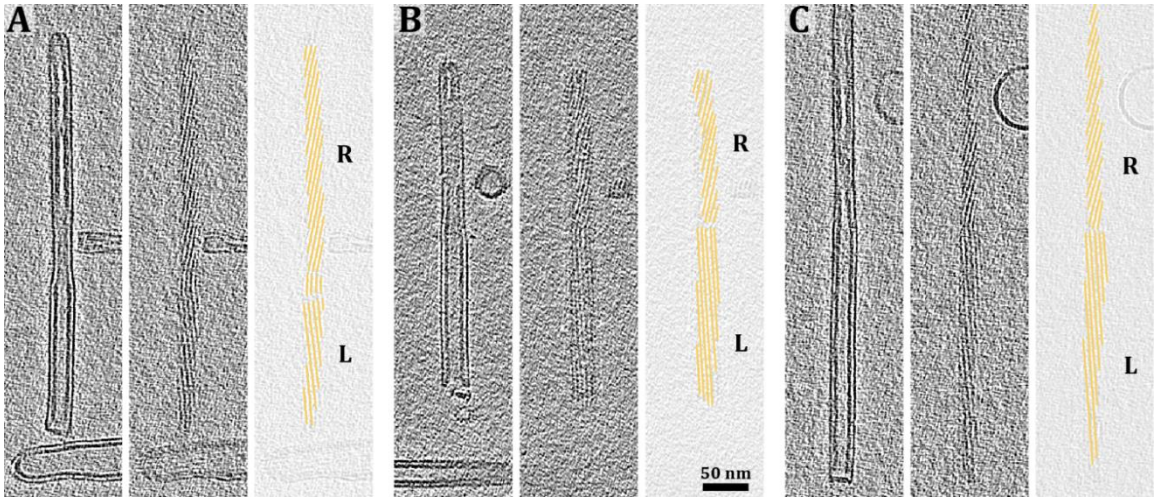

Figure 15: Vipp1 rods can change their handedness at discrete points.

Three Vipp1 rods that switch from a right-handed helix (R) to a left-handed helix (L) at discrete points along their lengths (A-C). For each panel, the left image is a slice from the tomogram showing a central longitudinal section through the Vipp1 rod (with encapsulation of PC:PI4P liposomes), the middle image is a slice from the tomogram showing the top surface of the rod, and the right image shows lines that were draw along each rod's striations (yellow) to illustrate the helical pitch. These examples serve as a control to visually confirm that Vipp1 rods adopt both right- and left-handed helical pitches.

4.1.3 Subtomogram averaging of the CrVipp1 cryo-ET dataset

We next performed subtomogram averaging of the cryo-ET dataset (Figure 16 and Figure 17), with the aim of gaining structural insights into the Vipp1-liposome interaction. Unfortunately, the extreme heterogeneity of Vipp1 rod structure (with variable diameter, helical pitch, and handedness) prevented us from combining multiple rods together to generate a high-resolution average of single Vipp1 proteins within the rod.

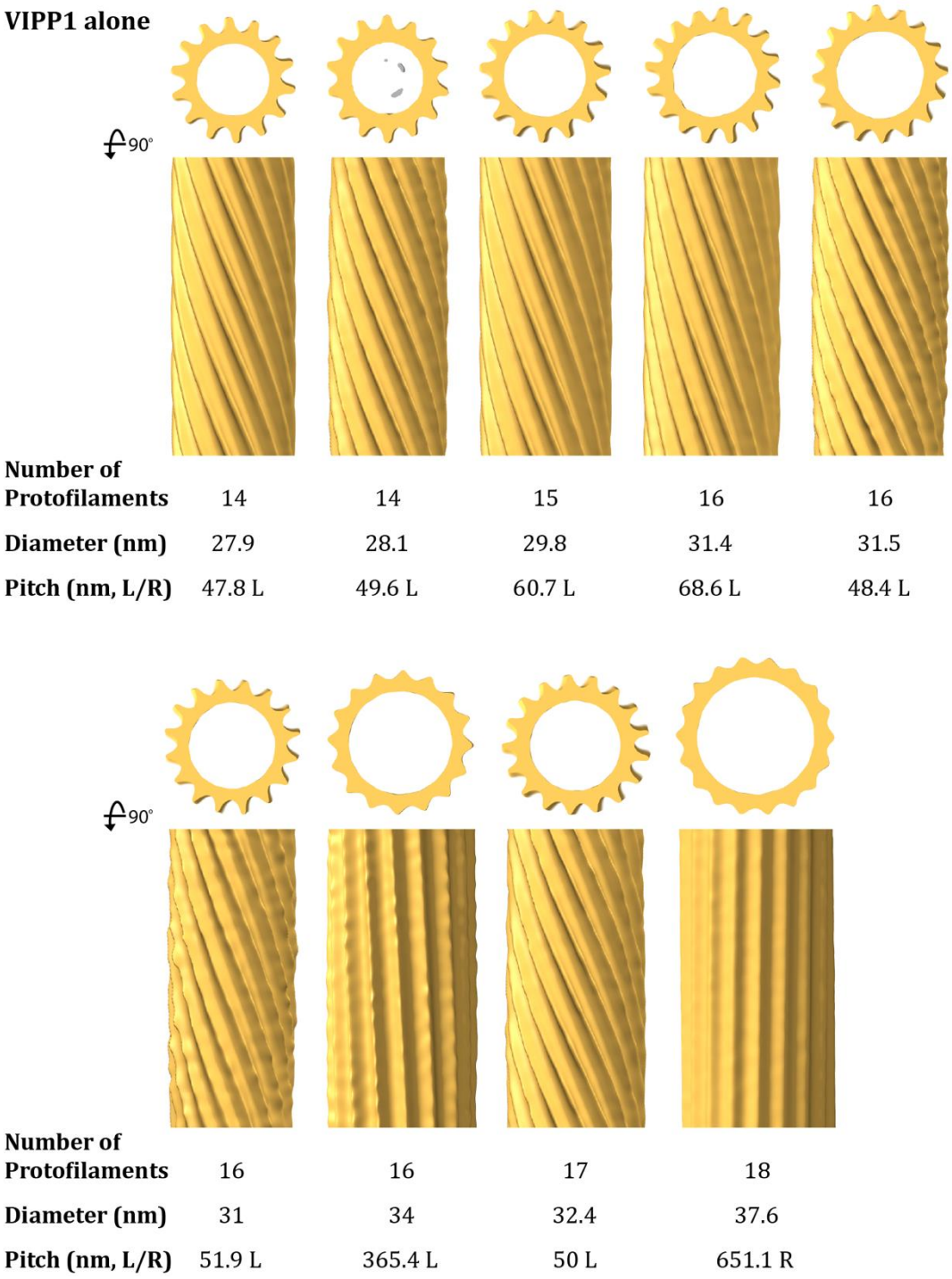

Figure 16: Subtomogram averages of Vipp1 rods alone (yellow).

Top: cross-sections through averages, bottom: longitudinal views of the rod outer surfaces. Rods are shown to scale. Parameters displayed for each individual rod and are quantified in Figure 18B-D.

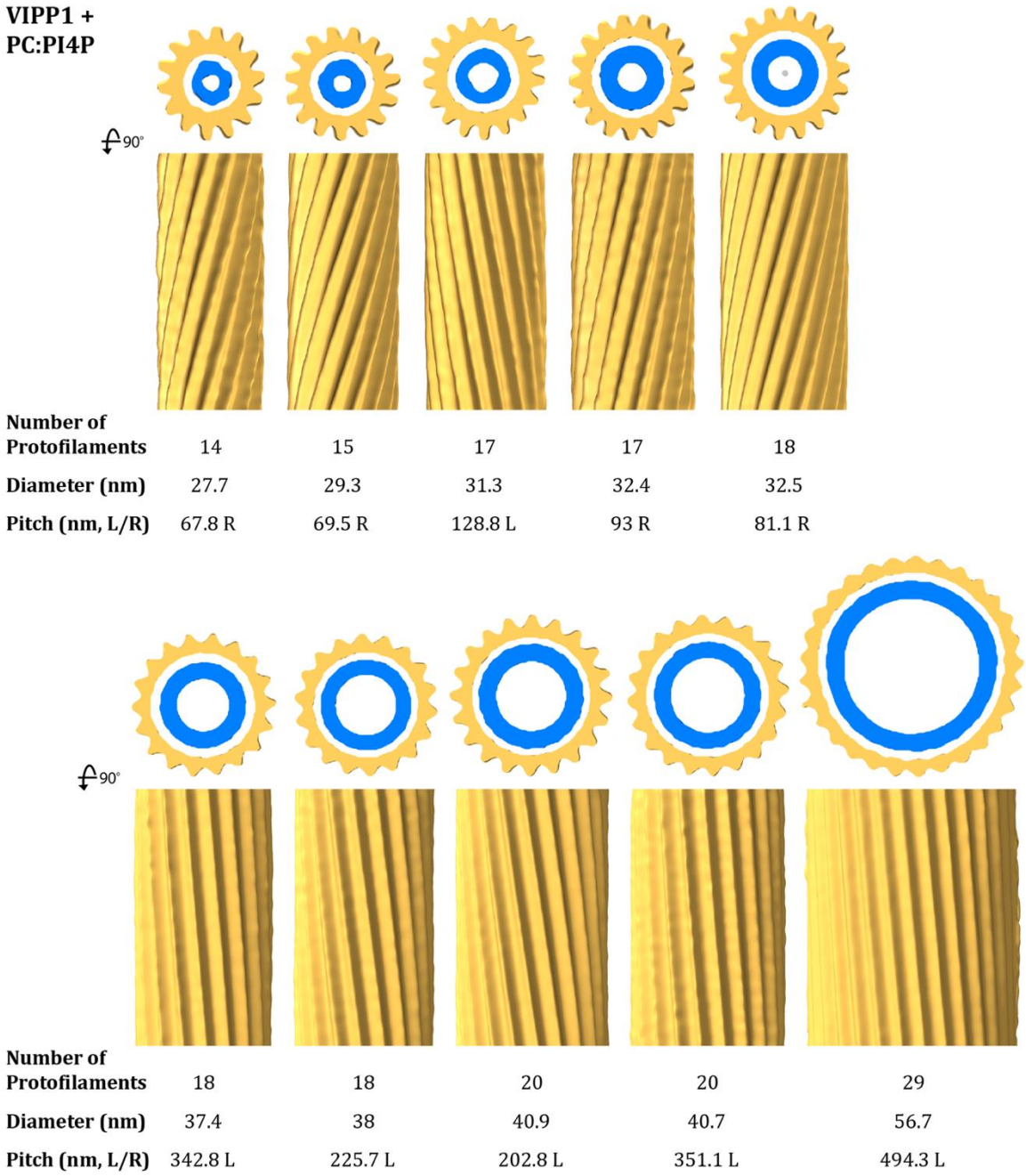

Figure 17: Subtomogram averages of Vipp1 rods (yellow) incubated with PI4Pcontaining liposomes (blue).

Top: cross-sections through averages showing the engulfed liposomes, bottom: longitudinal views of the rod outer surfaces. Rods are shown to scale. Parameters displayed for each individual rod and are quantified in Figure 18B-D.

Nonetheless, we were able to generate averages of individual rods (Figure 16 and Figure 17), enabling accurate measurement of each rod's geometric parameters (Figure 18). The number of striations per rod in the two Vipp1 preparations studied was broadly distributed, ranging from 13 to 35 with the maximum of the distribution

at 16 striations (Figure 18B). Rod diameters ranged from ~28 nm up to ~60 nm and increased linearly with striation numbers (Figure 16, Figure 17 and Figure 18C). The diameter of the engulfed lipid tubule was set by the rod diameter, with the center-to-center distance between the bilayer of the lipid tubule and the wall of the Vipp1 rod remaining at a constant ~5 nm (Figure 18C). This suggested that Vipp1 rods specifically interacted with lipid membranes instead of randomly enclosing them. Rods of all diameters were capable of engulfing liposomes. The wall thickness of the encapsulated lipid tubule was ~6 nm, consistent with a lipid bilayer.

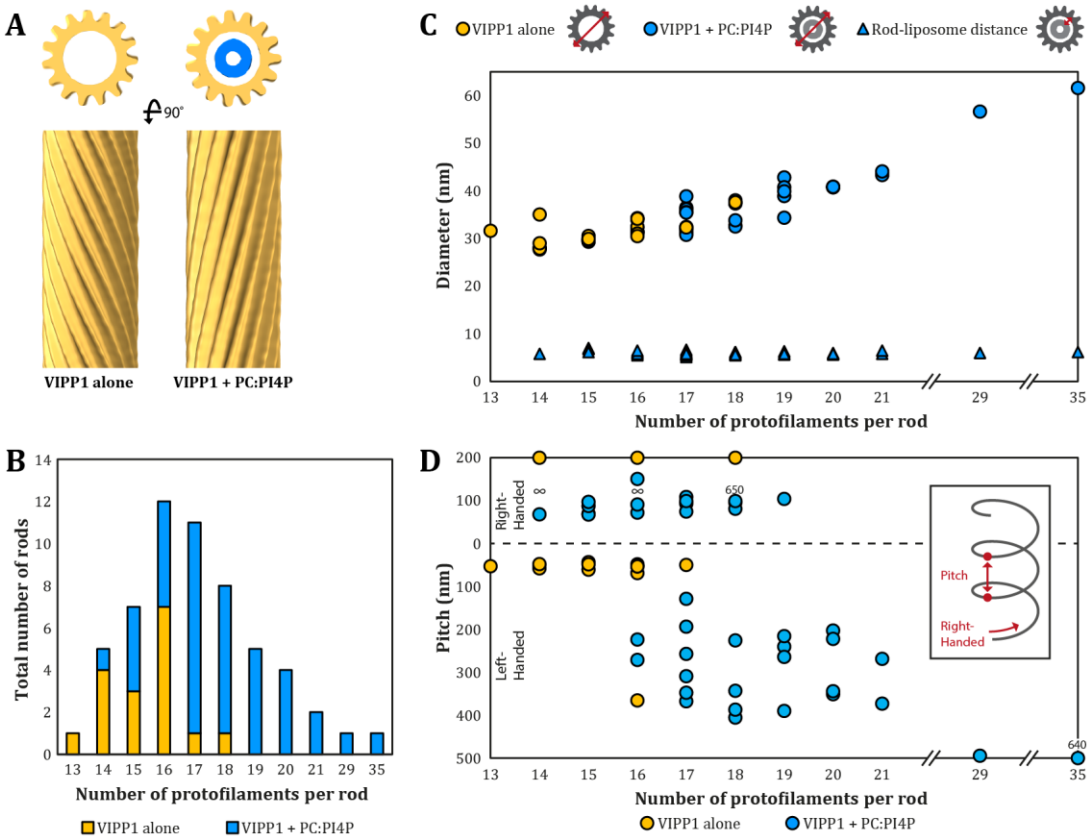

Figure 18: Subtomogram analysis of Vipp1 rods.

(A) Example subtomogram averages from single Vipp1 rods (yellow) without (left) and with (right) PC:PI4P (95:5) liposomes (blue). Top: cross-sections through averages, bottom: longitudinal views of the rod outer surfaces. (B) Distribution of the number of striations per rod in the two cryo-ET datasets, which were acquired from two separate Vipp1 preparations (see methods). (C) Plot of Vipp1 rod diameter vs. number of striations (circles) for the two cryo-ET datasets. For the sample containing Vipp1 and PC:PI4P liposomes, the center-to-center distance between the wall of the Vipp1 rod and the membrane bilayer of the engulfed liposome is also plotted (triangles). (D) Plot of Vipp1 rod helical pitch vs. number of striations for the two cryo-ET datasets. Both left- and right-handed pitches are plotted. Values are listed above individual points for rods with pitches outside the plotted range. "∞" indicates non-helical rods with striations oriented parallel to the rod's long axis.

We observed a higher number of striations, and corresponding wider diameter, for some Vipp1 rods engulfing PC:PI4P lipids compared to empty Vipp1 rods (Figure 18B-C). While it is tempting to speculate that the engulfed liposomes are responsible for the wider rod diameters, it is important to note that the empty and liposome-encapsulating rods came from different preparations of the Vipp1 protein (see methods). We observed major variations in rod diameter between different preparations, which may be correlated with Vipp1 protein concentration, with higher concentrations favoring wider diameters (Figure 13E). However, because the rods were likely already formed on the chitin column after DTT-induced cleavage of the fusion protein, variability in loaded protein concentrations, cleavage efficiency, and elution speed prevents the accurate correlation of rod diameter with final preparation concentration. Thus, the comparison between empty and liposome-encapsulating rods must be made within a single Vipp1 prep. We performed this same-preparation comparison by negative stain and found that the addition of PC:PI4P liposomes only had a minor effect on Vipp1 rod diameter (Figure 13D).

4.1.4 Vipp1 rods assemble with either right- or left-handed helical pitches

In 55 out of 57 Vipp1 rods analyzed in detail by cryo-ET, we observed helical pitches as seen by the inclination of the striations relative to the long axis of the rod. Rod helical pitches were highly heterogeneous, ranging from 43 nm (strongly twisted) to 650 nm (almost parallel), while two rods had parallel striations. Adding to this heterogeneity, Vipp1 rods assembled with either right- or left-handed helical pitches (Figure 16, Figure 17, and Figure 18D). We also observed discrete points along some rods where diameter and helical pitch abruptly changed, independent of liposome engulfment (arrowheads in Figure 14B, J). A few rods even switched their handedness at these points (Figure 15).

4.1.5 Vipp1: a novel PIP-dependent membrane-shaping protein?

Although it has been appreciated for decades that phosphatidylinositols are present in chloroplast membranes (Dorne et al., 1990), very little is known about their

function in this organelle. Only a few PIP-binding chloroplast proteins have been reported. These include the outer envelope-spanning PDV1 and PDV2 proteins that bind to PI4P in the envelope and are involved in chloroplast division (Okazaki et al., 2015), as well as the wheat WKS1 kinase that binds to phosphatidic acid and PIPs via a START domain and phosphorylates a thylakoid-associated ascorbate peroxidase (Gou et al., 2015). Although our results indicated that Vipp1 is another PIP-binding chloroplast protein, it is puzzling that phosphatidylinositols do not exist in cyanobacteria (Boudière et al., 2014), but Vipp1 function is conserved from cyanobacteria to plants. Therefore, either chloroplast Vipp1 has evolved a different lipid specificity, or PIPs mimic an unidentified and rare lipid type, modification, or composition present in both chloroplast and cyanobacterial membranes. In any case, it is noteworthy that PIPs in other cellular membranes serve as targeting sites for proteins with membrane-shaping properties reminiscent of those observed here for Vipp1 (Takenawa, 2010). One such protein is epsin, which binds to plasma membrane areas enriched in PI(4,5)P2 and deforms the membrane via insertion of an amphipathic helix, facilitating the formation of clathrin-coated vesicles (Ford et al., 2002). BAR domain proteins interact with membrane areas enriched in PI(4,5)P2 and phosphatidylserine via cationic residues at the concave surface of their banana-shaped structure to induce membrane curvature (Peter et al., 2004). The yeast BAR domain proteins Pil1 and Lsp1 can assemble into long filaments that align their BAR domains on the plasma membrane to form a "half-pipe" static furrow (Karotki et al., 2011; Strádalová et al., 2009). These furrows, termed eisosomes, act as scaffolds that recruit specific proteins and lipids. Many membrane proteins must be localized to eisosomes in order to function optimally (Foderaro et al., 2017). *In vitro*, Pil1 and Lsp1 can tubulate PI(4,5)P2-containing liposomes in a similar manner to Vipp1 (Karotki et al., 2011).

4.1.6 What are the implications of these *in vitro* observations for Vipp1 function within the cell?

Analogous to eisosomes formed by Pil1 and Lsp1, Vipp1 rods might play a role in organizing domains in thylakoid membranes at which translocases such as TAT and Sec, as well as integrases like Alb3, are recruited into a lipid environment that is

essential for their proper function. This would explain how Vipp1 facilitates protein translocation across, and protein integration into, thylakoid membranes (Lo and Theg, 2012; Walter et al., 2015) and thereby Vipp1 ’s role in the biogenesis and repair of thylakoid membrane protein complexes (Fuhrmann et al., 2009a; Gao and Xu, 2009; Gutu et al., 2018; Kroll et al., 2001; Nordhues et al., 2012; Walter et al., 2015; Westphal et al., 2001b; Zhang and Sakamoto, 2013; Zhang et al., 2014). Vipp1 rods may also play a role in organizing domains in the inner envelope of chloroplasts, giving rise to filamentous and lattice-like structures (Zhang et al., 2012, 2016a). Such structures might help preserve the integrity of stressed membranes (e.g., under osmotic stress) or might have an analogous function to eisosomes in supporting the function of membrane transporters. Long tubules with the same diameter as Vipp1 rods, referred to as microtubule-like structures, have been observed in the stroma of various plastid types in early electron microscopy studies (Lawrence and Possingham, 1984; Liu et al., 2007; Schnepf, 1961). Thus, it is also possible that Vipp1 rods with engulfed lipids exist in the chloroplast stroma with possible functions in lipid transfer or lipid storage.

5 Single-particle cryo-EM study of the *Synechocystis* Vipp1 protein

The following results were obtained together with collaborators. The purified protein was provided by Karin Gries and Prof. Michael Schroda (TU Kaiserslautern). Electron microscopy, image processing, and single-particle structure determination were performed by Tilak Kumar Gupta with the help of Jan Schuller (MPI biochemistry). Model building was performed by Sven Klumpe with the help of Tilak Kumar Gupta and Dr. Till Rudack.

5.1 Results

5.1.1 Data processing and initial model building

In the previous section, we discussed that CrVipp1 forms rods of variable symmetry. Due to the variable handiness, diameter and pitch, the dataset could not be combined to produce a high-resolution molecular structure of crVipp1. Therefore, we next studied *Synechocystis* Vipp1 (SynVipp1) using single-particle cryo-EM. Unlike rod-forming CrVipp1, SynVipp1 predominantly forms rings. Ring structures are accessible by single-particle cryo-EM, where large datasets can be readily obtained and the variation in symmetry can be parsed using 3D classification.

SynVipp1 was heterologously expressed and purified from *E. coli*. The grids were prepared and imaged as described in the method section. From previous studies, we knew that SynVipp1 forms rings of variable symmetry. However, there was no high-resolution structure of a synVipp1 ring available to be used as a reference. A *de novo* approach was applied to pick particles and then generate an initial model from our dataset (Figure 19A and A.1). From 8120 micrographs, we used a subset of manually-picked particles resembling top and side views of rings to train the deep-learning based crYOLO program, which subsequently extracted the full initial dataset of 337,000

particles (Dataset-A). A round of 2D classification was used to clean this dataset, yielding 263,000 particles (Dataset-B). To generate an initial 3D model *de novo*, we used a RELION3.0 implementation of stochastic gradient descent (SGD) without applying symmetry. The SGD algorithm allows for *ab initio* heterogeneous structure determination without a prior model of the molecule's structure. Starting with Dataset-B, a very rough class was obtained from around 33,000 particles. Another round of initial model building was performed using these particles, and 20,000 particles were selected to produce an improved 3D structure exhibiting C17 symmetry. Using this structure as a reference, 3D classification of the 20,000 particles was performed without applying symmetry constraints. The 3D classification split the particles into several classes, yielding 3D volumes for both C15 and C17 symmetries. Using these two volumes as references, a separate 3D classification of the full Dataset-B was performed. This split the particles into two large classes and generated an improved 3D volume to be used as a reference for the next round of 3D classification (Figure 19B). To obtain homogeneous classes of particles, 120,000 particles from the C15 class and 62,000 particles from the C17 class were subjected to several rounds of 3D classification (Figure 19C). These classifications split the particles into new classes with C14, C15, C16, C17 and C18 symmetries. Several rounds of 3D refinement were performed for these symmetry classes, yielding 3D structures with resolutions ranging from 4.5 Å to 6.5 Å (Figure 19D).

When further rounds of 3D classification and refinement did not improve the resolution of Dataset-B, the final density maps of each symmetry were used as references for 3D classification of the full Dataset-A (337,000 particles) (Figure 19E). The reason behind this was to extract the particles directly from the initial dataset based on the specific 3D references corresponding to each symmetry class. Large angular sampling was applied to speed up the classification process, and the dataset was divided into 5 classes corresponding to specific symmetries (Figure 19E). Each symmetry class was subjected to several rounds of 3D classification with fine angular sampling (3.5°) (Figure 19F). The goal of this step was to clean the classes further to generate homogeneous classes of particles.

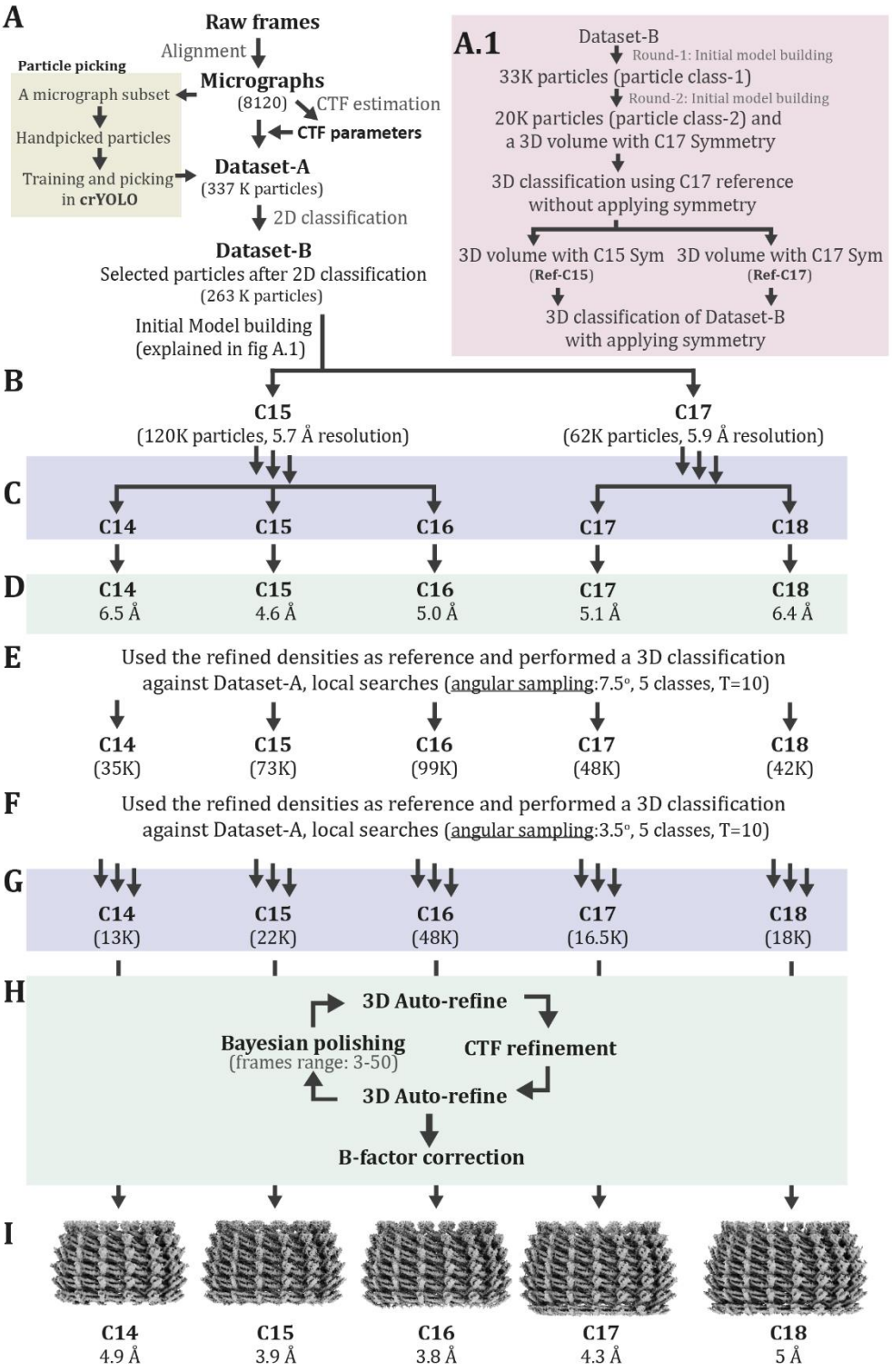

Figure 19: Schematic overview of cryo-EM single-particle data processing.

Automated particle picking was performed with crYOLO. From 8120 micrographs, 337K particles were extracted and designated as Dataset-A. These particles were subjected to 2D classification, yielding 263K particles that were designated as Dataset-B. These particles were then used to generate reference-free initial models as described in A.1. All the steps were performed in RELION3.0's single-particle data processing pipeline. Individual steps are explained in the above section.

In order to rule out any bias due to symmetry application, several symmetry-free rounds of 3D classification were included. At the end of these multiple rounds of 3D classification, a homogeneous particle class was obtained for each symmetry (Figure 19G). These homogeneous classes were then subjected to several rounds of the RELION auto-refinement procedure to obtain final reconstructions. The auto-refinement steps were combined with CTF refinement, Bayesian polishing and B-factor correction (Figure 19H). During Bayesian polishing, the last 30-45 frames (from the total 80 frames) of each micrograph were discarded. The auto-refinement process was iterated until no further improvement was observed. All final density maps of Vipp1 rings were resolved below 5 Å (Figure 19I), and the C15 and C16 maps were resolved below 4 Å.

5.1.2 Vipp1 monomers interweave with each other to make a basket-like structure

Following the data processing pipeline detailed above, density maps for five different symmetries were obtained (Figure 19). In order to understand how 30kDa Vipp1 monomers form these large barrel-like assemblies, the Vipp1 ring with C16 symmetry was analyzed in detail.

One C16 Vipp1 ring is constructed of six layers stacked on one another. Each layer has 16 Vipp1 monomers (Figure 20A-B). Thus, 96 (16x6) Vipp1 monomers are interwoven with each other, giving a basket-like appearance. The top layer (layer-1) of the ring is more tapered (more narrow diameter) than the bottom layer (layer-6). It is also clear from the structure that the outermost layer-1 and layer-6 are the least resolved in the whole structure.

One Vipp1 monomer consists of 7 helices (Figure 20F). In order to understand how these helices are arranged within the oligomer, layer-3 was extracted and examined. Four shades of blue are shown, where each shade represents one Vipp1 monomer. We found that Vipp1 monomers are interwoven in an extended manner, making contact with six other monomers within the same layer (Figure 20D-E).

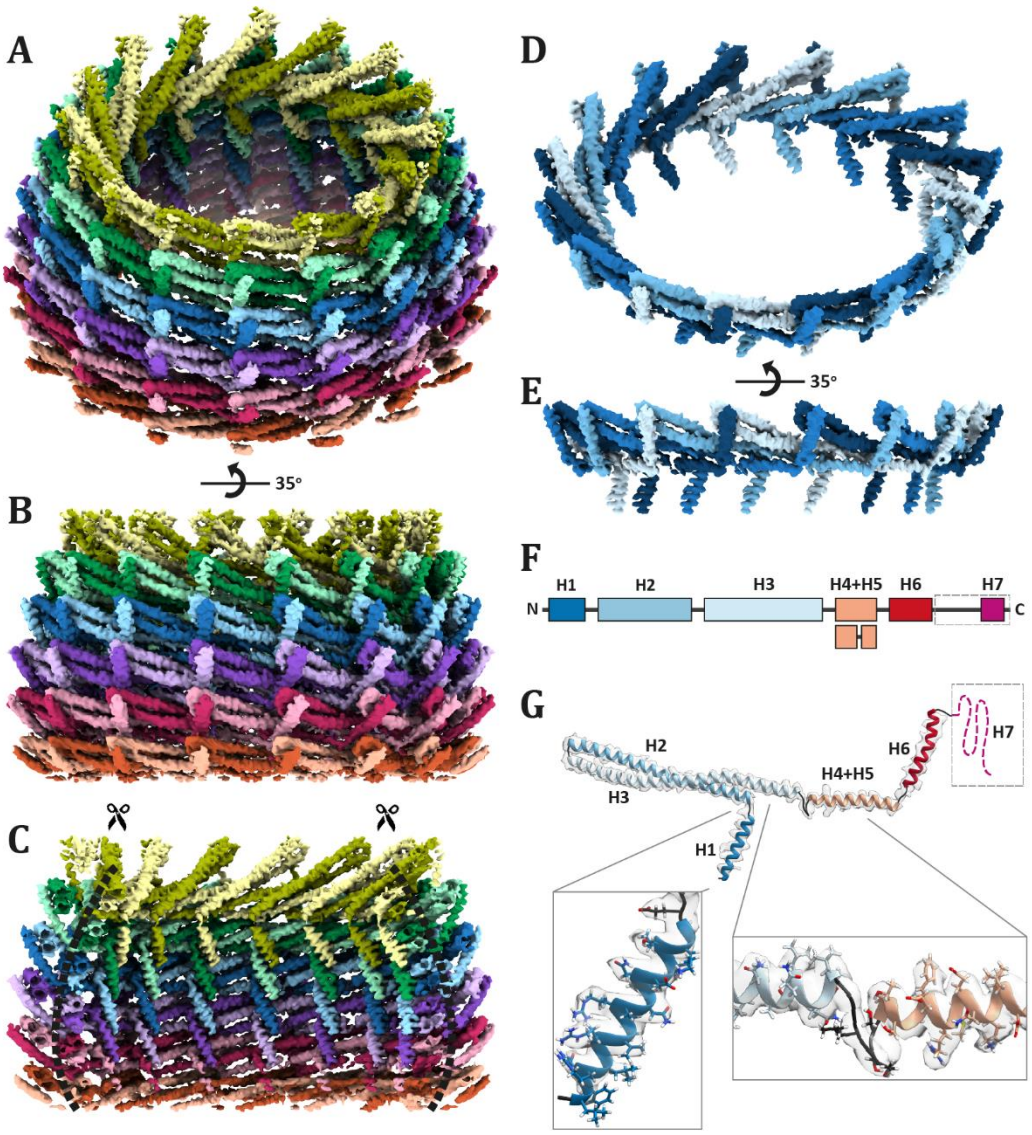

Figure 20: Vipp1 monomers interweave to make a basket-like ring structure.

(A) Top and (B) side views of a Vipp1 ring with C16 symmetry. The ring consists of 6 layers shown in different colors. Vipp1 monomers interweave to produce a basket-like shape. Two shades of each color were used to highlight the interwoven pattern. (C) A cut-open view of the ring reveals that H1 helices align to form vertical columns that face toward the lumen. (D) Top and (E) side views of one of the central layers, shown in isolation to visualize the way Vipp1 monomers interweave. Four shades of blue are used to show that each Vipp1 monomer extends to contact six other monomers within the layer. (F) Schematic diagram of the secondary structure elements of the Vipp1 monomer and (G) the corresponding regions on the Vipp1 model. The C-terminal domain including H7 (dashed line box) was not resolved in the EM density map, likely due to high flexibility. Magnified view of two regions of the monomer structure, showing the fit of the Vipp1 model's side chains into the EM density map.

From this EM density map, we generated an atomic model of the Vipp1 ring oligomer (as described in the methods section). One Vipp1 monomer superimposed with its EM density map is shown in Figure 20G, colored according to the helical domain diagram in Figure 20F. Throughout the structure, side-chain densities were

resolved for several bulky amino acids such as arginine, lysine, leucine, isoleucine, glutamate, aspartate, tryptophan, and phenylalanine (Figure 20G boxes). Density corresponding to a C-terminal domain, including H7, was missing from the EM density map of all the symmetries. This domain was not resolved because it contains disordered regions and thus is highly flexible. H1 faces toward the lumen of the ring and H6 faces outside. The N-terminal H1 helices of all the monomers align with each other to form vertical columns that run along the inside of the ring (Figure 20A and C). H2 and H3 form a coiled-coil structure (Figure 20G), and H3 is connected to H4 via a loop of seven amino acids (Figure 20G, right box).

5.1.3 SynVipp1 can assemble into rings of multiple rotational symmetries

As described earlier, five different symmetries (C14-C18) were found in our Vipp1 dataset. Density maps of the respective symmetries are shown in Figure 21A. Ring diameter increased linearly from C14 to C18 (Figure 21D). Ring height was dependent on the number of layers present in the ring. C14, C15 and C16 rings had six layers and an average height of 17.5 nm. C17 and C18 had seven layers and an average height of 19.5 nm. Atomic protein models were generated for these symmetries (Figure 21B), revealing how each layer has a distinct geometry. Focusing on H6, which protrudes from the outer wall of the ring, the inclination of this helix changes from almost flat in layer-6 to almost vertical in layer-1 (Figure 21C). In order to estimate this change, the angle of H6 with respect to the horizontal plane of the ring was measured for each layer in each symmetry (Figure 21E). The average values were plotted with standard deviation, showing a linear relationship (Figure 21F).

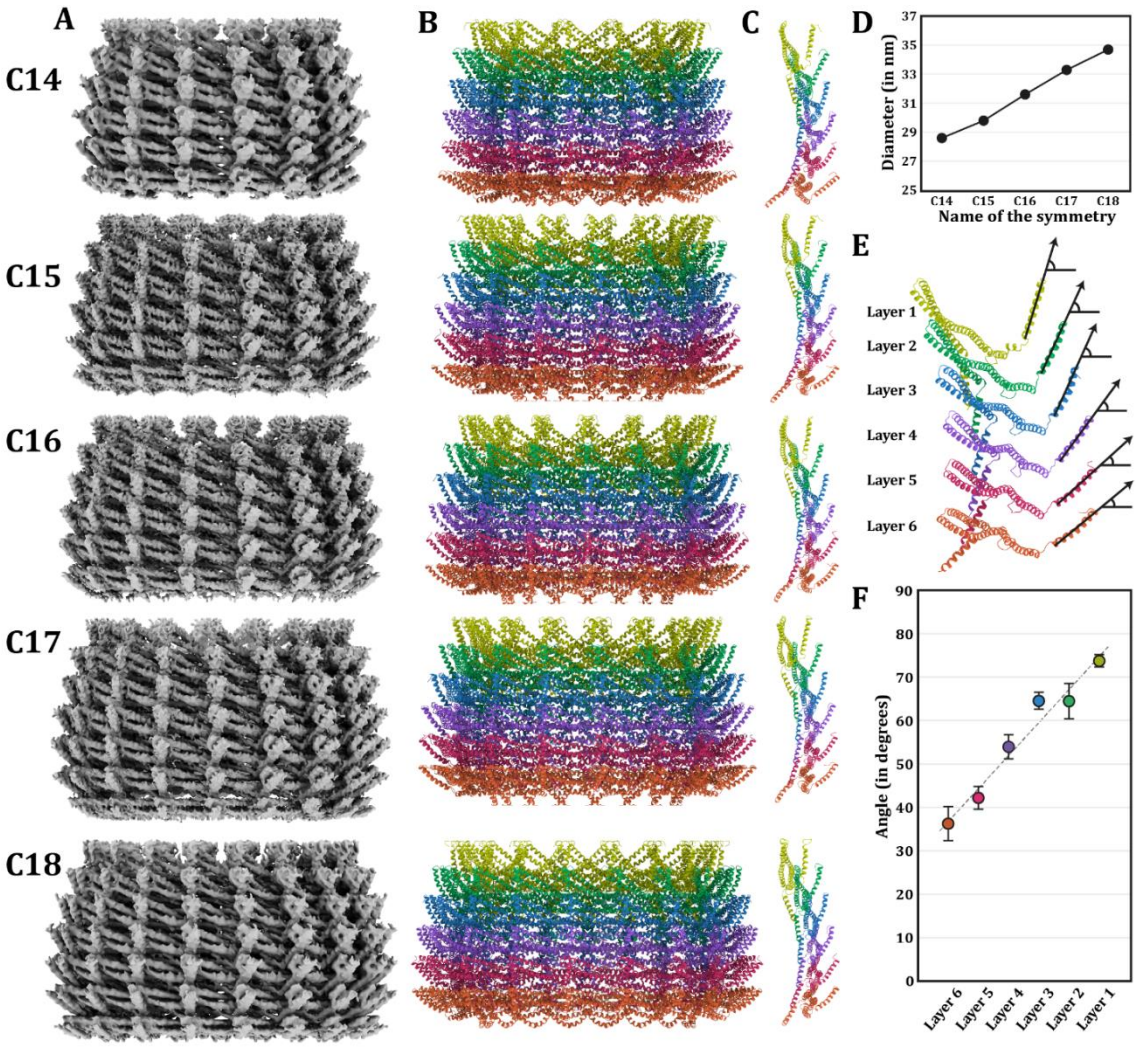

Figure 21: Vipp1 can assemble into the rings of variable symmetries.

(A) Density maps and (B) corresponding protein models are shown for different symmetries. Density maps for C14, C15 and C16 have six layers, whereas C17 and C18 have seven layers (only the first six layers from the top could be modeled). (C) One vertical row of monomers is displayed, showing the arrangement of H1 (left side) and H6 (right side) for each ring structure. (D) Plot showing the maximum diameter of each Vipp1 ring. (E-F) For each Vipp1 structure, the inclination of H6 was analyzed by measuring the angle of H6 relative to the horizontal plane of the ring. Mean values and standard deviations are plotted in (F).

5.1.4 Vipp1 structural features and flexibility

Having generated molecular models of Vipp1 rings for five different symmetries, we were then able to examine how the Vipp1 monomer can accommodate this range of architecture. To understand Vipp1 flexibility, we made two comparisons: 1) how the monomer structure changes across the layers within a single ring of a given symmetry, and 2) how the monomer structure changes for the same layer across the different symmetries.

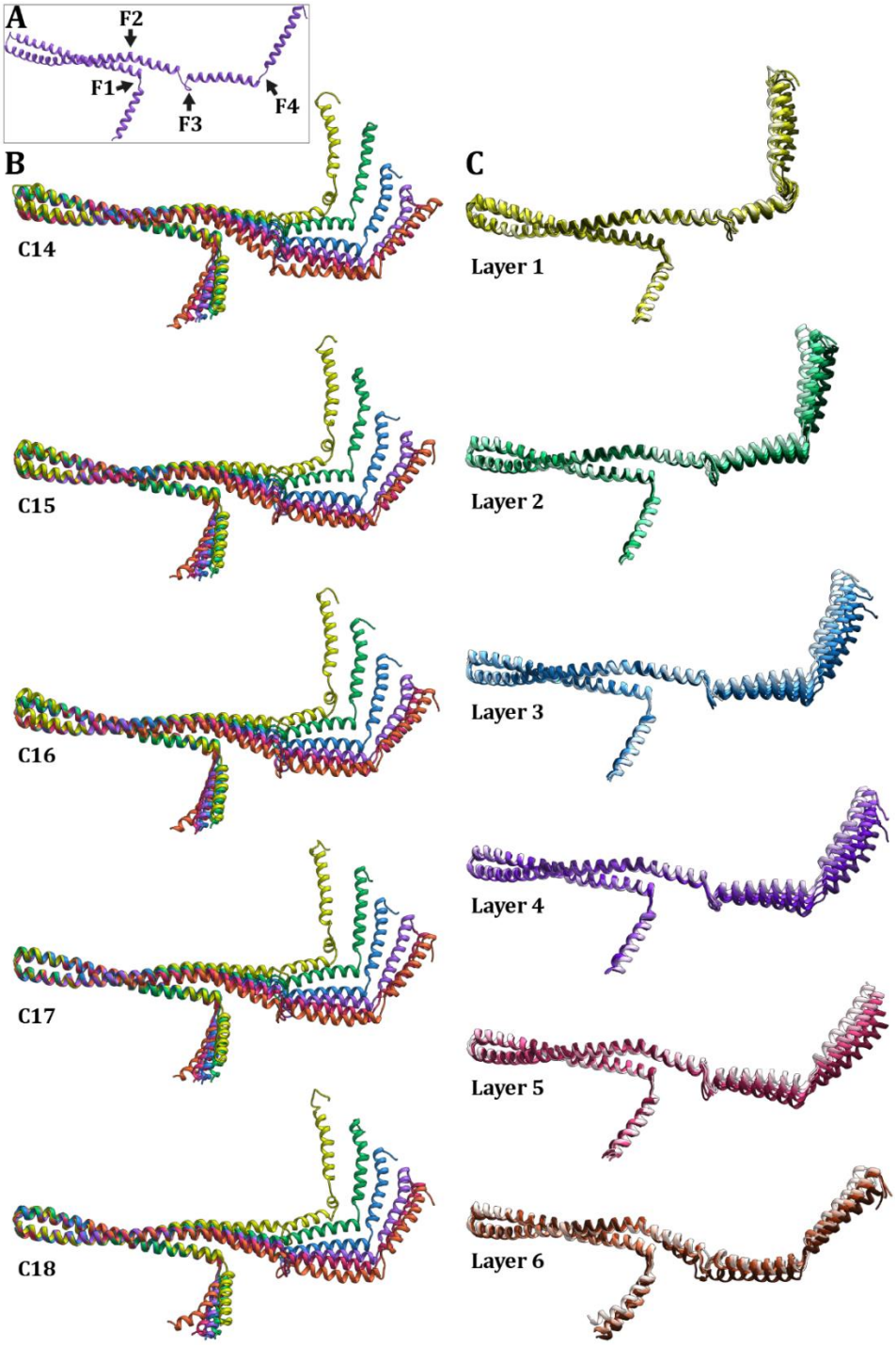

Figure 22: Vipp1 monomers have four regions of flexibility.

Vipp1 makes barrel-shaped rings of variable symmetry. (A) This heterogeneity is due to the presence of four flexibility regions in the Vipp1 monomer. (B) For rings of each symmetry, Vipp1 monomers from each layer were superimposed. The color scheme matches Figure 20A-C. (C) Vipp1 monomers were superimposed with monomers of the same layer across all five symmetries. Five color variants of the corresponding layer color were used, with the darkest color corresponding to C14 and the lightest color corresponding to C18.

For comparison #1, one Vipp1 monomer was taken from each layer of a ring, and the monomers were then superimposed with each other using UCSF Chimera's

Matchmaker program (Figure 22B). This was done for all five symmetries. For comparison #2, one Vipp1 monomer was taken from an individual layer and superimposed with the monomer of the same layer from all five symmetries (Figure 22C). This analysis revealed four regions of flexibility (Figure 22A), which we named F1-F4. F1 is located between H1and H2, F2 is located within H3, F3 is the loop between H3-H4/H5 and F4 is located between H4/H5 and H6. The variation between the layers within a ring was due to movement in F1, F2, F3, and F4. For an individual layer across the symmetries, the flexibility was caused only by movement in F3, the loop of seven amino acids between H3 and H4/H5 (Figure 22C).

5.1.5 Interaction network of Vipp1 monomers within the ring

From the first look at the Vipp1 ring, it is apparent that Vipp1 makes an intricate network where each Vipp1 monomer interacts with several other monomers. To examine these interactions in detail, we mapped the contact points on one Vipp1 monomer from layer-3 (Figure 23A). Based on the distances between individual amino acids, the contact points were identified and visually analyzed with the help of UCSF Chimera. Segments of different Vipp1 monomers are shown that may interact with the chosen Vipp1 monomer (blue, L3) (Figure 23A). The purpose behind this analysis was to map the intricate Vipp1 ring interaction network and to quantify how many other Vipp1 monomers contact individual monomers. To present this more clearly, we show a schematic diagram that illustrates how one Vipp1 protein can interact with as many as 16 other monomers (Figure 23B). As the N-terminal H1 is important for Vipp1 assembly, we examined a zoomed-in view focused on H1 (Figure 23C). H1 interacts with four other monomers: one from the same layer, another from the layer above (layer-2) and two more from the layer below (layer-4) (Figure 23B-C).

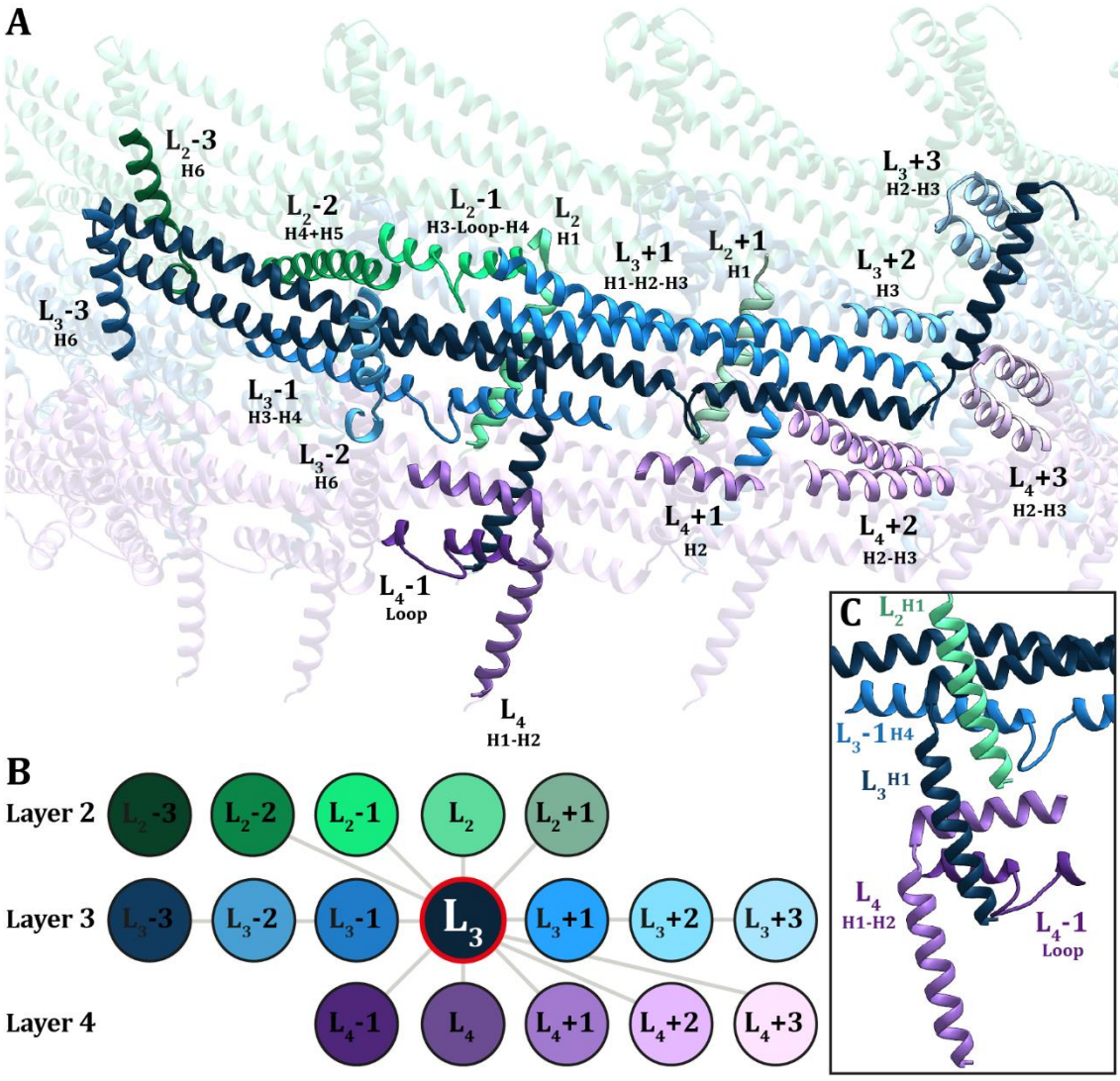

Figure 23: Interaction network of one Vipp1 monomer.

One Vipp1 monomer from layer-3 (L3, dark blue) was examined to highlight the intricate network of interaction in the Vipp1 ring (A). Also displayed are regions of other Vipp1 monomers that are in close vicinity and can interact with the reference monomer L3. Numbering is assigned with respect to L3: monomers that are positioned to the right of L3 are denoted as +1, +2 and +3, whereas monomers that are positioned to the left of L3 are denoted as -1,-2 and -3. Monomers that are directly above and below L3 are denoted as L2 and L4, as these monomers come from layer-2 and layer-4, respectively. (B) The schematic diagram of this interaction network, showing that one monomer can interact with up to 16 neighbors. (C) N-terminal H1 interacts with 4 other Vipp1 monomers: one monomer from the layer above (layer-2 in this case), one monomer from within the same layer (layer-3 in this case) and two monomers from the layer below (layer-4 in this case).

5.1.6 Role of the N-terminal Helix-1 in lipid binding and the assembly of the Vipp1 ring

The H1 domains of each layer are arranged in orderly rows facing the lumen of the Vipp1 ring (Figure 20A and C). Additional density not accounted for by the protein model was also found inside the lumen of all the symmetries (Figure 24A). This density was located in close proximity to the rows of H1 (Figure 24B, left panel). The highly organized arrangement of the H1 and the proximity of this extra density indicated that a specific interaction might be taking place. While examining the H1 rows, we found that the hydrophobic amino acids of H1 were facing toward this density (Figure 24B, right panel).

Vipp1's H1 domain is an amphipathic helix (Figure 24C). Several studies have emphasized the importance of H1 to Vipp1 ring formation and its lipid binding ability. In order to understand the role of H1 in the stability of the ring, several point mutations were introduced to specific positions in H1, especially on hydrophobic amino acids. To decide which amino acid to be mutated, three criteria were considered: the Vipp1 model that was constructed in this study, already available literature, and evolutionarily conserved positions. Based on this information, a series of single H1 point mutations were performed including a double point mutation for highly conserved arginines at positions 6 and 9 (Figure 24C-D). For each point mutation, the amino acid was replaced by glutamate, a negatively-charged amino acid that would interfere with the native interactions of the hydrophobic or positively-charged residues. The effects of these mutations were analyzed by negative stain EM (as described in the method section). None of these point mutations were found to disrupt the ability of Vipp1 to oligomerize into large assemblies. To our surprise, in almost all mutant proteins, the predominantly ring-forming SynVipp1 started assembling into long rod structures, resulting in a mixed population of rings and rods (Figure 24E). The F4E mutation was the only exception, as it formed only rings. Our Vipp1 molecular model shows that Phe4 faces towards the lumen and does not interact with other Vipp1 proteins present in the ring. In contrast, Arg6 and Arg9 face away from the lumen, toward the inner wall of the ring (Figure 24D). Vipp1 proteins with a single point mutation of these two arginines made more rods, while the R6ER9E double mutation

made almost exclusively rods (Figure 24E). This result indicates that the interaction of H1 with the inner wall of the Vipp1 oligomer may promote the formation of closed-symmetry rings over open-symmetry rods. However, as the mutation of lumen-facing hydrophobic residues (L3E, L7E, V10E, V11E, L15E) also resulted in the assembly of rods, it is possible that the binding of luminal material to the H1 rows (orange density in Figure 21A-B) also promotes the ring structure. The effects of mutating the hydrophobic lumen-facing residues on the ability of Vipp1 to bind lipids remains a topic for future study.

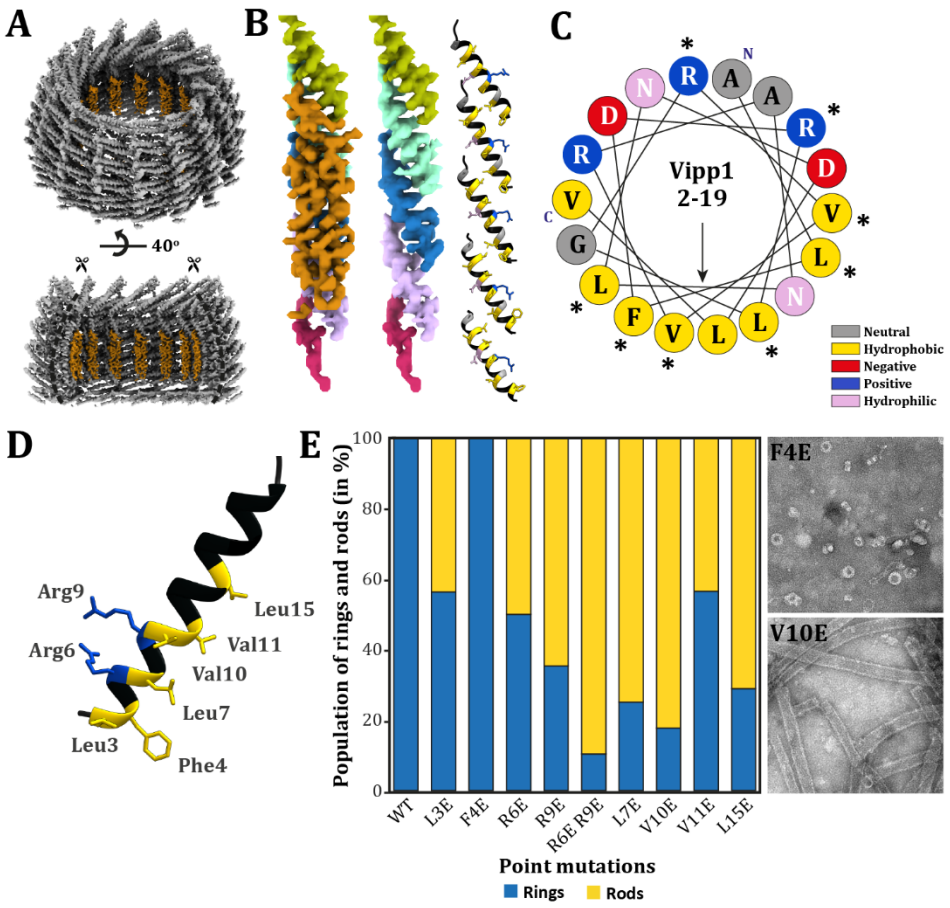

Figure 24: Role of the N-terminal H1 in lipid binding and the assembly of rings and rods.

(A) A density not accounted for by the protein model (orange) is bound the rows of H1 inside the lumen of the Vipp1 ring. (B) One of the H1 rows is shown with (left) and without (middle) this extra density. Amino acids that face toward this density are shown in the Vipp1 molecular model (right). Hydrophobic amino acids are yellow. (C) Helical wheel projection of H1, indicating amino acids that were mutated (*). (D) Positions of mutated amino acids are shown in the molecular model of H1. (E) Different point mutations caused Vipp1 to form rings and rods. (Left) Population distribution of rings and rods for the point mutations is plotted. These percentages were measured using a grid-based method as described in the method section (Figure 12). (Right) Representative negative stain images for the mutants F4E, which makes only rings, and V10E, which predominantly makes rods.

5.1.7 SynVipp1 rings have nucleotide binding pockets

A second density not assigned to the molecular model was found within the Vipp1 ring located between layer-1 and layer-2 (Figure 25A). Close inspection revealed that this unidentified density could be a nucleotide, where the nucleotide binding pocket is created by the combination of three different Vipp1 monomers located in layer-1 and layer-2. A recent study suggested that the Vipp1 has GTP hydrolysis activity (Ohnishi et al., 2018) (Figure 9).

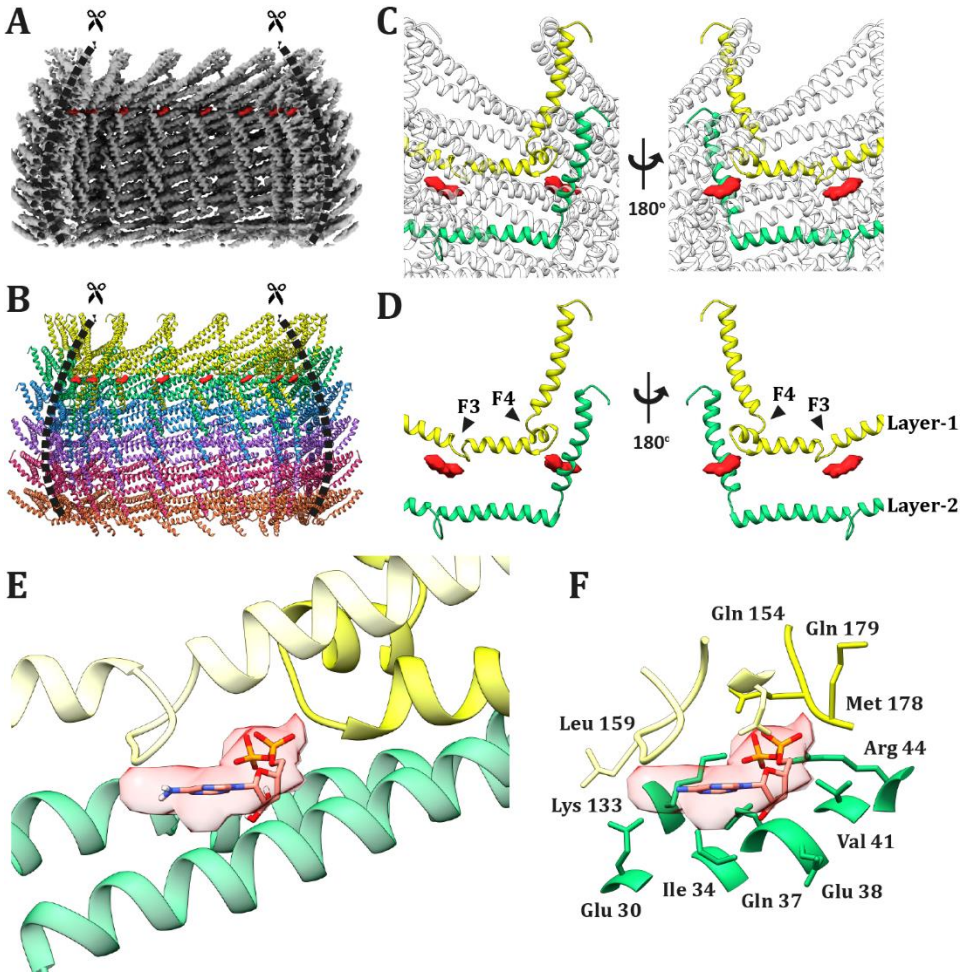

Figure 25: A putative nucleotide binding pocket is located between the layer-1 and the layer-2 of the Vipp1 ring.

(A) A density not accounted for by the Vipp1 molecular model (red) is located between layer-1 and layer-2 facing the lumen of the Vipp1 ring. (B) The same density is shown in the Vipp1 molecular model. (C) The position of two of the nucleotides is shown from outside (left) and from the lumen side (right). (D) Same views as panel C, but with only two monomers displayed. H4 of layer-1 breaks into two helices (H4 and H5) so that the nucleotide can be accommodated. (E) The pocket is formed by interactions from two different loops in layer-1 from two different Vipp1 monomers (shown in two shades of light yellow), supported by H2 and H3 of layer-2 (shown in green). (F) Amino acids surrounding the nucleotide density are displayed.

In order to confirm whether this additional density is a nucleotide, we analyzed purified SynVipp1 rings with electrospray ionization-mass spectroscopy (ESI-MS), coupled to reversed-phase ion-pair high-performance liquid chromatography (RPIP-HPLC). This analysis reliably identified a low-molecular weight mass corresponding to ADP (Figure 26). We closely inspected the SynVipp1 molecular model to learn about the nucleotide binding pocket. The pocket is formed by interactions from two different loops in layer-1, supported by H2 and H3 of layer-2 (Figure 25E-F). Strikingly, H4 of layer-1 breaks into two helices (H4 and H5) so that the nucleotide can be accommodated (Figure 25D).

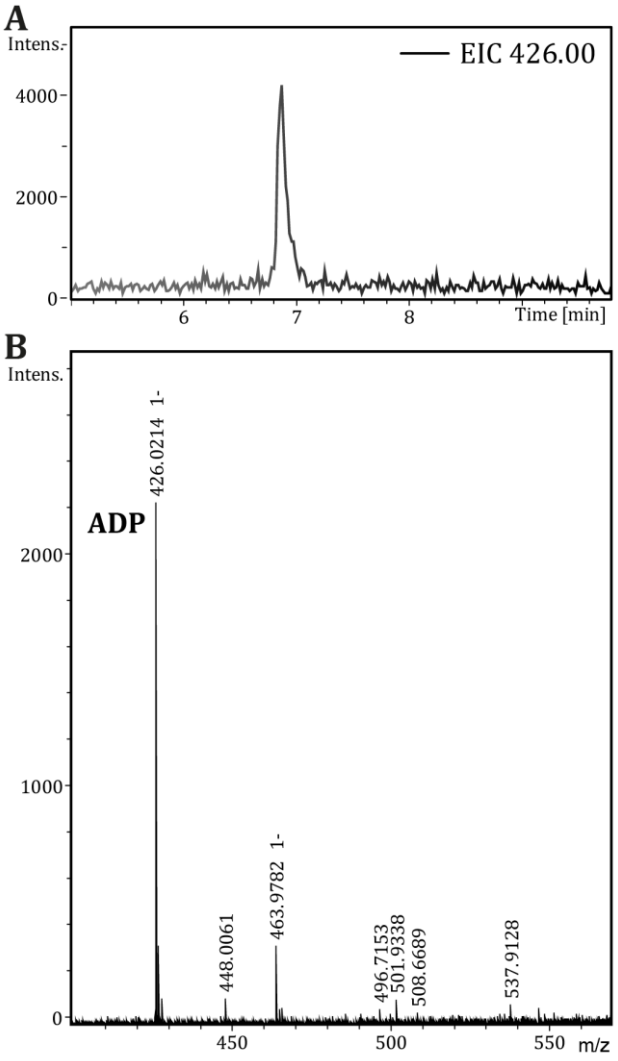

Figure 26: Ion-pair HPLC-MS spectrum of SynVipp1.

(A) HPLC extracted-ion chromatogram and (B) MS analysis of the indicated peak fraction. The MS spectrum reveals that ADP, not GTP or GDP, is bound to the SynVipp1 preparation used in this study.

5.2 Discussion

5.2.1 Vipp1 monomers interweave with each other to make basket-like ring assemblies

Recently, a structural study of SynVipp1 rings was carried out using negative stain EM (Figure 7) (Saur *et al.*, 2017). Due to inherent limitations of the negative staining method, these structures were low resolution and did not provide information about how Vipp1 monomers are arranged within the Vipp1 ring. The molecular model put forward by this study was based on computational structure prediction and limited biochemical information. This model proposed that four Vipp1 monomers assemble vertically side by side to make a tetrameric assembly known as a core particle. The tetrameric core particle would then act as a building block for the assembly of Vipp1 rings. A homology-based model of SynVipp1 was generated using the partial crystal structure of PspA, a bacterial homolog of Vipp1. This homology model was fitted into the negative stain EM density vertically, parallel to the central axis of the ring (Figure 7). Despite a lack of strong experimental evidence, it was proposed that four Vipp1 monomers aligned vertically account for one asymmetric unit of the ring (Saur et al., 2017). There are two issues here:

First, the partial crystal structure of PspA, which was used to make the homology model of Vipp1, represents only amino acids 3-144 (Osadnik et al., 2015), covering H1, H2, and much of H3 (our model shows that H3 extends up to residue 156). Furthermore, the region corresponding to H1, a helical element that is crucial for the Vipp1 oligomer formation, was unstructured in the PspA crystal structure. This may be because, unlike the coiled-coil interaction between H2 and H3, H1 lacks stabilizing interactions within a single monomer and instead primarily interacts with other monomers within the Vipp1 ring. It has also been shown that the presence of lipids may be required to structure the H1 domain into a helix (McDonald et al., 2017).

Second, because the negative stain density map was of a limited resolution, it was not justifiable to fit the homology model. Biochemical and functional studies, e.g. the recent report of Vipp1's GTPase activity, have relied on this structural model. Therefore, a reliable Vipp1 model is of paramount importance to understand the numerous functions of this protein.

Applying cryo-electron microscopy single-particle analysis, we solved structures of Vipp1 rings at with resolutions as high as 3.8 Å resolution. From these maps, we were able to clearly visualize how the Vipp1 monomers are arranged in the ring. We found that Vipp1 monomers are not stacked with each other like vertical columns, but instead make an interwoven network that resembles a wicker basket. Each Vipp1 monomer interacts with 16 other monomers within the ring: six other monomers within the same layer, five monomers within the layer above, and another five monomers in the layer below. This extended interaction network helps stabilize the large, well-defined ring architecture. We could unambiguously assign the positions of the α-helices H1-H6 in the Vipp1 ring, whereas H7 was absent from our density maps. H7, a helix of ~20 amino acids, is connected to H6 by a ~25 amino acid flexible linker region. The flexibility of this linker is likely why H7 could not be resolved in our structure. However, based on the resolved position of H6 on the outer wall of the ring, it is clear that H7 extends outside the ring. Thus, one can envision the complete Vipp1 ring as a "hairy basket", where H7 wobbles around the exterior of the basket through an unstructured connecter of 25 amino acids.

H1, located inside the ring facing toward its lumen, appears to serve two functions. First, it stabilizes the ring structure by interacting with four other monomers. Two monomers come from the ring below (H1-H2 from one monomer and a loop between H3-H4 from another monomer), one monomer comes from the ring above (H1) and another monomer comes from within the same ring (H4). These multiple interactions might be necessary to position H1 in the right orientation, with its hydrophobic surface facing outward toward the ring's lumen. This positioning of H1 is likely important for Vipp1's proposed lipid-binding function.

Vipp1 is known to assemble into the rings of variable symmetries. In a cryo-EM study where MGDG-DOPG liposomes were mixed with SynVipp1 protein, Vipp1 rings of different diameters were found to bind the surfaces of liposomes (Saur et al., 2017). It was proposed that the membrane binding property of Vipp1 was not restricted by the ring size. Rather, structural flexibility is probably necessary for the proper function of Vipp1 in the chloroplast (Zhang et al., 2012). Most of the negative stain EM studies of synVipp1 rings predominantly showed top views of the rings, but side views were occasionally captured (Aseeva et al., 2004; Fuhrmann et al., 2009b; Liu et al., 2007; Nordhues et al., 2012). However, it was not clear whether rings of different symmetries also had different heights. A recent negative stain EM study shed some light on this question but could not reach a definitive conclusion due to the low resolution of the structure (Saur et al., 2017). Using cryo-EM, we more accurately measured the diameters and heights of Vipp1 rings and found that the rings can have different heights of 6-7 layers, with higher symmetries (C17 and C18) adding the seventh layer.

While the overall architecture of Vipp1 monomer was identical across the symmetries, we found four regions of flexibility. This flexibility appears to allow Vipp1 to assemble into a wide variety of symmetries. All four regions (F1-F4) bend and flex to enable Vipp1 monomers to assemble into the different layers of a ring. In contrast, for the same layer across the symmetries (e.g., layer-1 in C14-C18), the flexibility primarily comes from F3, which is a loop of 7 amino acids. Therefore, this loop apparently enables the Vipp1 rings to expand to reach higher symmetries with increased diameter.

5.2.2 Role of the highly conserved Vipp1 motifs in the organization of Vipp1 rings

Two highly conserved clusters of amino acids are present near the loop connecting H2 with H3: $_{75}$AxxAL$_{79}$ (located at the end of H2) and $_{84}$ExLA$_{87}$ (located near the starting point of H3) (Osadnik et al., 2015) (Figure 20F-G). A recent study analyzed the following Vipp1 variants: Vipp1_AAL (A$_{75}$S, A$_{78}$S, and L$_{79}$A) and Vipp1_ELA (E$_{84}$A, L$_{86}$A, and A$_{87}$S). These mutants were no longer able to induce membrane fusion and

could not form double-ring structures in the presence of Mg^{2+} (Hennig et al., 2015; Saur et al., 2017). Based on the incorrect model where Vipp1 monomers were arranged vertically, these amino acids were proposed to be located towards the bottom of the ring (Figure 7).

From our high-resolution model, we found that the region close to the loop connecting H2 with H3 also mediates interactions with the H6 of two other monomers. $_{75}$AxxAL$_{79}$ mediates interaction with H6 of the monomer three positions to the left within the same layer. Similarly, $_{84}$ExLA$_{87}$ mediates interaction with H6 of the monomer three positions to the left but from the layer above. Therefore, these two clusters were important not only to maintain the structure of a single layer ($_{75}$AxxAL$_{79}$) but also for the assembly of multiple layers into a ring ($_{84}$ExLA$_{87}$).

Another highly conserved cluster of five amino acids ($_{168}$FERME$_{172}$) is located within H4 of both Vipp1 and PspA. A recent study described a Vipp1_FERM variant (F168A, E169A, R170A, and M171A) that did not form stable rings but instead made irregular high molecular mass aggregates (Heidrich et al., 2016; Saur et al., 2017). In our model, this cluster is located in H4 near the loop that connects H4 to H3. The amino acid cluster mainly provides interactions to monomers within the same layer, thus stabilizing the individual layer within the ring. Interestingly, we found that the glutamate in this cluster (E169) mediates multiple different interactions depending on its position in the ring. For layer-1, it mediates interaction with Arg56 of a monomer from layer-2 (at +2 position). In layer-2, it mediates interaction with Lys133 of a monomer from layer-3 (at +1 position). For layer-3 and layer-4, it does not make any interaction. For layer-5, it interacts with lys135 of a monomer from the same ring (at +1 position). This variability of interaction might be responsible for the altered positions helices across the layers. Mutating these residues will seriously hamper the overall organization of the Vipp1 ring.

5.2.3 Role of H1 in mediating Vipp1 ring assembly and lipid binding

An extra density was found within the lumen of the Vipp1 barrel, specifically in contact with the vertical H1 rows. Furthermore, our model revealed that hydrophobic amino acids of H1 were lined up facing toward this extra density, apparently mediating the interaction. We speculate that this extra density could be lipid based on the following observations:

1. AtVipp1 protein expressed in bacteria comes with lipid bound to it when purified (Otters et al., 2013).

2. With CrVipp1, we have observed a strong interaction between liposomes and the luminal surface of Vipp1 rods (Figure 14E-K), where rows of H1 are presumably located.

3. An FTIR experiment clearly demonstrated the role of H1 in the lipid binding ability of AtVipp1. Furthermore, lipase treatment of AtVipp1 to remove the bound lipid revealed that the α-helical content of AtVipp1 decreased in the absence of lipid (Otters et al., 2013).

4. SynVipp1, when expressed in bacterial cells lacking PspA, complemented the function of PspA in binding to the plasma membrane and protecting it under stress conditions. Thus, Vipp1 must bind to lipids in order to complement the function of PspA (DeLisa et al., 2004).

5. In a cryo-EM study where MGDG-DOPG liposomes were mixed with SynVipp1 protein, Vipp1 rings of different diameter were observed to bind the liposome surface (Saur et al., 2017).

6. In another study, synthetic peptides corresponding to the H1 domains (1-21 amino acids) of PspA and SynVipp1 were analyzed. Circular dichroism (CD) spectra showed that these peptides were unstructured in solution. However, conversion of these unstructured peptides to α-helical structures was observed

when incubated with membranes, highlighting the role of H1 in membrane sensing and binding (McDonald et al., 2017).

7. A partial crystal structure of bacterial PspA (3-144 amino acids) had unstructured H1, as there was no lipid present (Osadnik et al., 2015).

8. The lack of H1 abolishes the membrane-binding affinity of Vipp1 and PspA *in vivo* and *in vitro*. The importance of hydrophobic face of the H1 amphipathic helix has also been indicated for the membrane interaction (Jovanovic et al., 2014; McDonald et al., 2017; Otters et al., 2013).

9. The role of Vipp1 in membrane binding and lipid ordering (Heidrich et al., 2016) and its specificity to negatively charged lipids had also been studied (Heidrich et al., 2016; Hennig et al., 2015)

Based on these observations, we propose that the binding of lipid is necessary for the properly folded structure of H1 and that the extra density we see interacting with the luminal H1 rows corresponds to bacterial lipid. The SynVipp1 used for our study was expressed and purified from *E. coli*. We believe that our structure provides the first mechanistic look at the interaction between Vipp1 oligomers and lipids. However, complementary biochemical observations are needed to substantiate this claim.

5.2.4 Nucleotide binding pocket in Vipp1

Recently, a biochemical study showed that Vipp1 has a GTP hydrolysis activity. This GTPase activity was lost when H1 was deleted. Therefore, the role of H1 was proposed to be crucial for GTP hydrolysis activity, and the GTP binding pocket was proposed to be present on or near H1 (Ohnishi et al., 2018). Multiple-sequence alignment analysis between known GTPase proteins and Vipp1 did not reveal any common sequence such as canonical G domains or a tubulin/FtsZ-type G-box (Ohnishi et al., 2018). However, it was proposed that the reaction center for GTP binding and

hydrolysis on Vipp1 might be structured by oligomerization similarly to that in multimeric FtsZ, where the reaction site together with the nucleotide binding site was formed on adjacent monomers (Scheffers and Driessen, 2002).

Our molecular structure reveals that the Vipp1 nucleotide binding pocket is indeed formed by the oligomerization of monomers. However, H1 in not a component of the pocket. Rather, it is formed by H2 and H3 on layer-2 and two loops bordering H4 on layer-1. We believe the reason that the H1 mutation lacks GTPase activity is that such a deletion would prevent Vipp1 oligomerization, thereby indirectly preventing the formation of the nucleotide binding site. The biochemical basis and relevance for this unusual nucleotide binding await further investigations, but it could play a role in assembly and extension of the oligomeric Vipp1 assembly.

Using mass spectrometry, we found that ADP was the only nucleotide present in our Vipp1 rings. We did not detect any bound GTP/GDP. This may be because the Vipp1 rings that we examined were treated with an ATP wash to remove bound chaperones. It is possible that this ATP has replaced the bound GTP. This hypothesis is made more plausible by the recent discovery that Vipp1 also has ATPase activity (personal communication, Wataru Sakamoto).

6 Conclusion

Vipp1 was first identified nearly three decades ago. It is essential for thylakoid biogenesis and maintenance and thus is indirectly required for the survival of most life on Earth. Therefore, it is crucial to understand the structure and function of this protein in great detail. Several biochemical experiments have been performed to understand the molecular mechanism of Vipp1 function; however, their interpretation has been greatly hindered by the lack of a Vipp1 structure. We have solved the first molecular structure of Vipp1 oligomerized into rings of several symmetries, providing a structural foundation for understanding Vipp1 function.

In summary,

1. We discovered that the Vipp1 monomers form oligomeric rings by making an interwoven network that resembles a basket.

2. We propose a molecular model for the Vipp1 protein (H1-H6) based on high-resolution cryo-EM density maps.

3. By solving Vipp1 ring structures in five different symmetries (C14-C18), we described how the Vipp1 monomer has four regions of flexibility that enable it to assemble a variety of oligomeric architectures.

4. H1, which assembles into vertical columns on the luminal side of the ring, stabilizes the ring structure by interacting with other monomers. The hydrophobic face of H1 points towards the lumen and may provide a contact site for molecules such as lipids to interact with Vipp1.

5. From our new molecular model, we can precisely predict which amino acids likely play an important role in structural stability and which amino acids could serve a functional role, such as mediating the interaction with lipids.

Several open questions are yet to be answered, including:

1. How does the Vipp1 ring assemble? Given the polar structure of the ring, is there a defined side where assembly begins?

2. How does the transition between rings and rods take place? Some Vipp1 species predominantly make ring or rods, and there is a delicate balance between the two that can be tipped with single point mutations.

3. What is the *in vivo* functional significance of Vipp1 rings and rods?

4. The molecular structure of the C-terminal domain was absent in the Vipp1 structure described in this study. What is the structure of this domain, and how does it regulate Vipp1 function?

5. What is the role of nucleotide binding? Why is the nucleotide present only between layer-1 and layer-2? Do nucleotide binding and hydrolysis regulate assembly of the Vipp1 ring, with layer-1 acting as a starting base or a terminal cap? Alternatively, does the nucleotide perform a different function, such as mediating lipid interactions?

6. What does this new structure of Vipp1 tell us about its interactions with known partners, including several chaperones that regulate its oligomerization?

Our structure for the Vipp1 is just one step forward in understanding the function of this crucially important yet enigmatic protein. Future studies should be able to build on the information contained in our high-resolution model to address the role of Vipp1 in the biogenesis of thylakoid membranes and the maintenance of their intricate architecture.

7 Abbreviations

2D =	Two-dimensional
3D =	Three-dimensional
ADP =	Adenosine diphosphate
Arg =	Arginine
ATP =	Adenosine triphosphate
BSA =	Bovine serum albumin
CCD =	Charged-coupled device
CET =	Cryo-electron tomography
Cryo-EM =	Cryo-electron microscopy
CTF =	Contrast transfer function
DDD =	Direct detection device
DED =	Direct electron detector
DQE =	Detective quantum efficiency
EM =	Electron microscopy
FEG =	Field emission gun
FSC =	Fourier shell correlation
FT =	Fourier transformation
GTP =	Guanosine-5'-triphosphate
MDFF =	Molecular dynamics flexible fitting
ML =	Maximum likelihood
MS =	Mass spectrometry
PSI =	Photosystem I

PSII =	Photosystem II
PI4P =	Phosphatidylinositol-4-phosphate
PIPs =	Phosphatidylinositol phosphates
PDB =	Protein Data Bank
SNR =	Signal-to-noise ratio
SP cryo-EM =	Single-particle cryo-electron microscopy
SPA =	Single-particle analysis
SPR =	Single-particle reconstructions
UA =	Uranyl acetate
VMD =	Visual Molecular Dynamics, a program for the visualization of molecular systems

8 Bibliography

Albert, S., Schaffer, M., Beck, F., Mosalaganti, S., Asano, S., Thomas, H.F., Plitzko, J.M., Beck, M., Baumeister, W., and Engel, B.D. (2017). Proteasomes tether to two distinct sites at the nuclear pore complex. Proc. Natl. Acad. Sci. U. S. A. *114*, 13726–13731.

Amat, F., Castaño-Diez, D., Lawrence, A., Moussavi, F., Winkler, H., and Horowitz, M. (2010). Alignment of cryo-electron tomography datasets. Methods Enzymol. *482*, 343–367.

Andersson, M.X., and Sandelius, A.S. (2004). A chloroplast-localized vesicular transport system: A bio-informatics approach. BMC Genomics *5*, 1–8.

Armbruster, U., Labs, M., Pribil, M., Viola, S., Xu, W., Scharfenberg, M., Hertle, A.P., Rojahn, U., Jensen, P.E., Rappaport, F., et al. (2013). *Arabidopsis* CURVATURE THYLAKOID1 proteins modify thylakoid architecture by inducing membrane curvature. Plant Cell *25*, 2661–2678.

Arnold, J., Mahamid, J., Lucic, V., De Marco, A., Fernandez, J.J., Laugks, T., Mayer, T., Hyman, A.A., Baumeister, W., and Plitzko, J.M. (2016). Site-specific cryo-focused ion beam sample preparation guided by 3D correlative microscopy. Biophys. J. *110*, 860–869.

Asano, S., Fukuda, Y., Beck, F., Aufderheide, A., Förster, F., Danev, R., and Baumeister, W. (2015). A molecular census of 26S proteasomes in intact neurons. Science. *347*, 439–442.

Aseeva, E., Ossenbühl, F., Eichacker, L.A., Wanner, G., Soll, J., and Vothknecht, U.C. (2004). Complex formation of Vipp1 depends on its α-helical PspA-like domain. J. Biol. Chem. *279*, 35535–35541.

Aseeva, E., Ossenbühl, F., Sippel, C., Cho, W.K., Stein, B., Eichacker, L.A., Meurer, J., Wanner, G., Westhoff, P., Soll, J., et al. (2007). Vipp1 is required for basic thylakoid

membrane formation but not for the assembly of thylakoid protein complexes. Plant Physiol. Biochem. *45*, 119–128.

Bai, X.C., Fernandez, I.S., McMullan, G., and Scheres, S.H.W. (2013). Ribosome structures to near-atomic resolution from thirty thousand cryo-EM particles. Elife *2013*, e00461.

Bammes, B.E., Rochat, R.H., Jakana, J., Chen, D.H., and Chiu, W. (2012). Direct electron detection yields cryo-EM reconstructions at resolutions beyond 3/4 Nyquist frequency. J. Struct. Biol. *177*, 589–601.

Bastien, O., Botella, C., Chevalier, F., Block, M.A., Jouhet, J., Breton, C., Girard-Egrot, A., and Maréchal, E. (2016). New insights on thylakoid biogenesis in plant cells. Int. Rev. Cell Mol. Biol. *323*, 1–30.

Beck, M., Förster, F., Ecke, M., Plitzko, J.M., Melchior, F., Gerisch, G., Baumeister, W., and Medalia, O. (2004). Nuclear pore complex structure and dynamics revealed by cryoelectron tomography. Science. *306*, 1387–1390.

Benning, C., Xu, C., and Awai, K. (2006). Non-vesicular and vesicular lipid trafficking involving plastids. Curr. Opin. Plant Biol. *9*, 241–247.

Biyani, N., Righetto, R.D., McLeod, R., Caujolle-Bert, D., Castano-Diez, D., Goldie, K.N., and Stahlberg, H. (2017). Focus: The interface between data collection and data processing in cryo-EM. J. Struct. Biol. *198*, 124–133.

Boekema, E.J., Folea, M., and Kouřil, R. (2009). Single particle electron microscopy. Photosynth. Res. *102*, 189–196.

Bonifacino, J.S., and Glick, B.S. (2004). The mechanisms of vesicle budding and fusion. Cell *116*, 153–166.

Boudière, L., Michaud, M., Petroutsos, D., Rébeillé, F., Falconet, D., Bastien, O., Roy, S., Finazzi, G., Rolland, N., Jouhet, J., et al. (2014). Glycerolipids in photosynthesis: Composition, synthesis and trafficking. Biochim. Biophys. Acta - Bioenerg. *1837*, 470–480.

Brandt, F., Carlson, L.-A., Hartl, F.U., Baumeister, W., and Grünewald, K. (2010). The three-dimensional organization of polyribosomes in intact human cells. Mol. Cell *39*, 560–569.

Brenner, S., and Horne, R.W. (1959). A negative staining method for high resolution electron microscopy of viruses. BBA - Biochim. Biophys. Acta *34*, 103–110.

Briggs, J.A. (2013). Structural biology *in situ*—the potential of subtomogram averaging. Curr. Opin. Struct. Biol. *23*, 261–267.

Bryan, S.J., Burroughs, N.J., Evered, C., Sacharz, J., Nenninger, A., Mullineaux, C.W., and Spence, E.M. (2011). Loss of the SPHF homologue Slr1768 leads to a catastrophic failure in the maintenance of thylakoid membranes in *synechocystis sp. PCC 6803*. PLoS One *6*, e19625.

Bryan, S.J., Burroughs, N.J., Shevela, D., Yu, J., Rupprecht, E., Liu, L.N., Mastroianni, G., Xue, Q., Llorente-Garcia, I., Leake, M.C., et al. (2014). Localisation and interactions of the Vipp1 protein in cyanobacteria. Mol. Microbiol. *94*, 1179–1195.

Bultema, J.B., Fuhrmann, E., Boekema, E.J., and Schneider, D. (2010). Related but not twins. Commun. Integr. Biol. *3*, 162–165.

Bykov, Y.S., Schaffer, M., Dodonova, S.O., Albert, S., Plitzko, J.M., Baumeister, W., Engel, B.D., and Briggs, J.A. (2017). The structure of the COPI coat determined within the cell. Elife *6*, e32493.

Castaño-Díez, D., Kudryashev, M., Arheit, M., and Stahlberg, H. (2012). Dynamo: A flexible, user-friendly development tool for subtomogram averaging of cryo-EM data in high-performance computing environments. J. Struct. Biol. *178*, 139–151.

Chauhan, J.S., Mishra, N.K., and Raghava, G.P.S. (2010). Prediction of GTP interacting residues, dipeptides and tripeptides in a protein from its evolutionary information. BMC Bioinformatics *11*, 301.

Cheng, Y. (2015). Single-particle cryo-EM at crystallographic resolution. Cell *161*, 450–457.

Cheng, A., Tan, Y.Z., Dandey, V.P., Potter, C.S., and Carragher, B. (2016). Strategies for automated cryoEM data collection using direct detectors. Methods Enzymol. *579*, 87–102.

Cheng, A., Eng, E.T., Alink, L., Rice, W.J., Jordan, K.D., Kim, L.Y., Potter, C.S., and Carragher, B. (2018). High resolution single particle cryo-electron microscopy using beam-image shift. J. Struct. Biol. *204*, 270–275.

Chuartzman, S.G., Nevo, R., Shimoni, E., Charuvi, D., Kiss, V., Ohad, I., Brumfeld, V., and Reich, Z. (2008). Thylakoid membrane remodeling during state transitions in *Arabidopsis*. Plant Cell *20*, 1029–1039.

Cox, J.A., Tirone, F., Durussel, I., Firanescu, C., Blouquit, Y., Duchambon, P., and Craescu, C.T. (2005). Calcium and magnesium binding to human centrin 3 and interaction with target peptides. Biochemistry *44*, 840–850.

Danev, R., and Baumeister, W. (2016). Cryo-EM single particle analysis with the volta phase plate. Elife *5*, e13046.

Danev, R., Tegunov, D., and Baumeister, W. (2017). Using the Volta phase plate with defocus for cryo-EM single particle analysis. Elife *6*, e23006.

Davies, K.M., Daun, B., Gold, V.A.M., Muhleip, A.W., Brandt, T., Blum, T.B., Mills, D.J., and Brandt, W.K. (2014). Visualization of ATP synthase dimers in mitochondria by electron cryo-tomography. J. Vis. Exp. *91*, 51228.

DeLisa, M.P., Lee, P., Palmer, T., and Georgiou, G. (2004). Phage shock protein PspA of *Escherichia coli* relieves saturation of protein export via the Tat pathway. J. Bacteriol. *186*, 366–373.

Dorne, A.J., Joyard, J., and Douce, R. (1990). Do thylakoids really contain phosphatidylcholine? Proc. Natl. Acad. Sci. U. S. A. *87*, 71–74.

Douce, R. (1974). Site of biosynthesis of galactolipids in spinach chloroplasts. Science. *183*, 852–853.

Downing, K.H., and Glaeser, R.M. (2008). Restoration of weak phase-contrast images recorded with a high degree of defocus: The “twin image” problem associated with CTF correction. Ultramicroscopy *108*, 921–928.

Dubochet, J., Lepault, J., Freeman, R., Berriman, J.A., and Homo, J. -C. (1982). Electron microscopy of frozen water and aqueous solutions. J. Microsc. *128*, 219–237.

Elmlund, D., and Elmlund, H. (2015). Cryogenic electron microscopy and single-particle analysis. Annu. Rev. Biochem. *84*, 499–517.

Engel, B.D., Schaffer, M., Cuellar, L.K., Villa, E., Plitzko, J.M., and Baumeister, W. (2015). Native architecture of the *Chlamydomonas* chloroplast revealed by *in situ* cryo-electron tomography. Elife *4*, e04889.

Engl, C., Jovanovic, G., Lloyd, L.J., Murray, H., Spitaler, M., Ying, L., Errington, J., and Buck, M. (2009). *In vivo* localizations of membrane stress controllers PspA and PspG in *Escherichia coli*. Mol. Microbiol. *73*, 382–396.

Fan, X., Wang, J., Zhang, X., Yang, Z., Zhang, J.C., Zhao, L., Peng, H.L., Lei, J., and Wang, H.W. (2019). Single particle cryo-EM reconstruction of 52 kDa streptavidin at 3.2 Angstrom resolution. Nat. Commun. *10*, 2386.

Fernández, I.S., Bai, X.C., Hussain, T., Kelley, A.C., Lorsch, J.R., Ramakrishnan, V., and Scheres, S.H.W. (2013). Molecular architecture of a eukaryotic translational initiation complex. Science. *342*, 1240585.

Foderaro, J.E., Douglas, L.M., and Konopka, J.B. (2017). MCC/eisosomes regulate cell wall synthesis and stress responses in fungi. J. Fungi *3*, 61.

Ford, M.G.J., Mills, I.G., Peter, B.J., Vallis, Y., Praefcke, G.J.K., Evans, P.R., and McMahon, H.T. (2002). Curvature of clathrin-coated pits driven by epsin. Nature *419*, 361–366.

Förster, F., Medalia, O., Zauberman, N., Baumeister, W., and Fass, D. (2005). Retrovirus envelope protein complex structure *in situ* studied by cryo-electron tomography. Proc. Natl. Acad. Sci. U. S. A. *102*, 4729–4734.

Förster, F., Han, B.G., and Beck, M. (2010). Visual proteomics. Methods Enzymol. *483*, 215–243.

Frain, K.M., Gangl, D., Jones, A., Zedler, J.A.Z., and Robinson, C. (2016). Protein translocation and thylakoid biogenesis in cyanobacteria. Biochim. Biophys. Acta - Bioenerg. *1857*, 266–273.

Frank, J. (2010). Three-dimensional electron microscopy of macromolecular assemblies: Visualization of biological molecules in their native state (Oxford University Press, 2nd edition).

Frueh, D.P., Goodrich, A.C., Mishra, S.H., and Nichols, S.R. (2013). NMR methods for structural studies of large monomeric and multimeric proteins. Curr. Opin. Struct. Biol. *23*, 734–739.

Fuhrmann, E., Gathmann, S., Rupprecht, E., Golecki, J., and Schneider, D. (2009a). Thylakoid membrane reduction affects the photosystem stoichiometry in the cyanobacterium *Synechocystis sp. PCC 6803*. Plant Physiol. *149*, 735–744.

Fuhrmann, E., Bultema, J.B., Kahmann, U., Rupprecht, E., Boekema, E.J., and Schneider, D. (2009b). The vesicle-inducing protein 1 from *Synechocystis sp. PCC 6803* organizes into diverse higher-ordered ring structures. Mol. Biol. Cell *20*, 4620–4628.

Gao, H., and Xu, X. (2009). Depletion of Vipp1 in *Synechocystis sp. PCC 6803* affects photosynthetic activity before the loss of thylakoid membranes. FEMS Microbiol. Lett. *292*, 63–70.

Gao, F., Wang, W., Zhang, W., and Liu, C. (2015). α-Helical domains affecting the oligomerization of Vipp1 and its interaction with Hsp70/DnaK in *Chlamydomonas*. Biochemistry *54*, 4877–4889.

Gao, H., Sage, T.L., and Osteryoung, K.W. (2006). FZL, an FZO-like protein in plants, is a determinant of thylakoid and chloroplast morphology. Proc. Natl. Acad. Sci. U. S. A. *103*, 6759–6764.

Gerlach, P., Schuller, J.M., Bonneau, F., Basquin, J., Reichelt, P., Falk, S., and Conti, E. (2018). Distinct and evolutionary conserved structural features of the human nuclear exosome complex. Elife *7*, e38686.

Glaeser, R.M. (2019). How good can single-particle cryo-EM become? What remains before it approaches its physical limits? Annu. Rev. Biophys. *48*, 45–61.

Göhre, V., Ossenbühl, F., Crèvecoeur, M., Eichacker, L.A., and Rochaix, J.D. (2006). One of two Alb3 proteins is essential for the assembly of the photosystems and for cell survival in *Chlamydomonas*. Plant Cell *18*, 1454–1466.

Gold, V.A.M., Ieva, R., Walter, A., Pfanner, N., Van Der Laan, M., and Kühlbrandt, W. (2014). Visualizing active membrane protein complexes by electron cryotomography. Nat. Commun. *5*, 4129.

Goldstein, J.I., Newbury, D.E., Echlin, P., Joy, D.C., Lyman, C.E., Lifshin, E., Sawyer, L., Michael, J.R., Goldstein, J.I., Newbury, D.E., et al. (2003). The SEM and its modes of operation. In scanning electron microscopy and X-ray microanalysis, (Boston, MA: Springer US), pp. 21–60.

Gou, J.Y., Li, K., Wu, K., Wang, X., Lin, H., Cantu, D., Uauy, C., Dobon-Alonso, A., Midorikawa, T., Inoue, K., et al. (2015). Wheat stripe rust resistance protein WKS1 reduces the ability of the thylakoid-associated ascorbate peroxidase to detoxify reactive oxygen species. Plant Cell *27*, 1755–1770.

Grant, T., and Grigorieff, N. (2015). Measuring the optimal exposure for single particle cryo-EM using a 2.6 Å reconstruction of rotavirus VP6. Elife *4,* e06980.

Guo, Q., Lehmer, C., Martínez-Sánchez, A., Rudack, T., Beck, F., Hartmann, H., Pérez-Berlanga, M., Frottin, F., Hipp, M.S., Hartl, F.U., et al. (2018). *In situ* structure of neuronal C9orf72 Poly-GA aggregates reveals proteasome recruitment. Cell *172*, 696-705.e12.

Gutu, A., Chang, F., and O'Shea, E.K. (2018). Dynamical localization of a thylakoid membrane binding protein is required for acquisition of photosynthetic competency. Mol. Microbiol. *108*, 16–31.

Hagen, W.J.H., Wan, W., and Briggs, J.A.G. (2017). Implementation of a cryo-electron tomography tilt-scheme optimized for high resolution subtomogram averaging. J. Struct. Biol. *197*, 191–198.

Hall, C.E., Jakus, M.A., and Schmitt, F.O. (1945). The structure of certain muscle fibrils as revealed by the use of electron stains. J. Appl. Phys. *16*, 459–465.

Hammel, A., Zimmer, D., Sommer, F., Mühlhaus, T., and Schroda, M. (2018). Absolute quantification of major photosynthetic protein complexes in *Chlamydomonas reinhardtii* using quantification concatamers (qconcats). Front. Plant Sci. *9*, 1265.

Hankamer, B.D., Elderkin, S.L., Buck, M., and Nield, J. (2004). Organization of the AAA+ adaptor protein PspA is an oligomeric ring. J. Biol. Chem. *279*, 8862–8866.

Hashem, Y., des Georges, A., Fu, J., Buss, S.N., Jossinet, F., Jobe, A., Zhang, Q., Liao, H.Y., Grassucci, R.A., Bajaj, C., et al. (2013). High-resolution cryo-electron microscopy structure of the Trypanosoma brucei ribosome. Nature *494*, 385–389.

Van Heel, M., Gowen, B., Matadeen, R., Orlova, E. V, Finn, R., Pape, T., Cohen, D., Stark, H., Schmidt, R., Schatz, M., et al. (2000). Single-particle electron cryo-microscopy: Towards atomic resolution. Q. Rev. Biophys. *33*, 307–369.

Heidrich, J., Wulf, V., Hennig, R., Saur, M., Markl, J., Sönnichsen, C., and Schneider, D. (2016). Organization into higher ordered ring structures counteracts membrane binding of IM30, a protein associated with inner membranes in chloroplasts and cyanobacteria. J. Biol. Chem. *291*, 14954–14962.

Heidrich, J., Thurotte, A., and Schneider, D. (2017). Specific interaction of IM30/Vipp1 with cyanobacterial and chloroplast membranes results in membrane remodeling and eventually in membrane fusion. Biochim. Biophys. Acta - Biomembr. *1859*, 537–549.

Heinz, S., Rast, A., Shao, L., Gutu, A., Gügel, I.L., Heyno, E., Labs, M., Rengstl, B., Viola, S., Nowaczyk, M.M., et al. (2016). Thylakoid membrane architecture in *Synechocystis* depends on CurT, a homolog of the granal CURVATURE THYLAKOID1 proteins. Plant Cell *28*, 2238–2260.

Hennig, J., and Sattler, M. (2014). The dynamic duo: Combining NMR and small angle scattering in structural biology. Protein Sci. *23*, 669–682.

Hennig, R., Heidrich, J., Saur, M., Schmüser, L., Roeters, S.J., Hellmann, N., Woutersen, S., Bonn, M., Weidner, T., Markl, J., et al. (2015). IM30 triggers membrane fusion in cyanobacteria and chloroplasts. Nat. Commun. *6*, 7018.

Herzik, M.A., Wu, M., and Lander, G.C. (2019). High-resolution structure determination of sub-100 kDa complexes using conventional cryo-EM. Nat. Commun. *10*, 1032.

Huxley, H.E., and Zubay, G. (1961). Preferential staining of nucleic acid-containing structures for electron microscopy. J. Biophys. Biochem. Cytol. *11*, 273–296.

Ishijima, S., Uchibori, A., Takagi, H., Maki, R., and Ohnishi, M. (2003). Light-induced increase in free Mg^{2+} concentration in spinach chloroplasts: Measurement of free Mg^{2+} by using a fluorescent probe and necessity of stromal alkalinization. Arch. Biochem. Biophys. *412*, 126–132.

Jovanovic, G., Mehta, P., McDonald, C., Davidson, A.C., Uzdavinys, P., Ying, L., and Buck, M. (2014). The N-terminal amphipathic helices determine regulatory and effector functions of phage shock protein A (PspA) in E*scherichia coli*. J. Mol. Biol. *426*, 1498–1511.

Joyard, J., and Stumpf, P.K. (1981). Synthesis of Long-Chain Acyl-CoA in Chloroplast Envelope Membranes. Plant Physiol. *67*, 250–256.

Karim, S., Alezzawi, M., Garcia-Petit, C., Solymosi, K., Khan, N.Z., Lindquist, E., Dahl, P., Hohmann, S., and Aronsson, H. (2014). A novel chloroplast localized Rab GTPase protein CPRabA5e is involved in stress, development, thylakoid biogenesis and vesicle transport in *Arabidopsis*. Plant Mol. Biol. *84*, 675–692.

Karotki, L., Huiskonen, J.T., Stefan, C.J., Ziółkowska, N.E., Roth, R., Surma, M.A., Krogan, N.J., Emr, S.D., Heuser, J., Grünewald, K., et al. (2011). Eisosome proteins assemble into a membrane scaffold. J. Cell Biol. *195*, 889–902.

Kenneth Hoober, J., Boyd, C.O., and Paavola, L.G. (1991). Origin of thylakoid membranes in *Chlamydomonas reinhardtii* y-1 at 38°C. Plant Physiol. *96*, 1321–1328.

Keren, N., Liberton, M., and Pakrasi, H.B. (2005). Photochemical competence of assembled photosystem II core complex in cyanobacterial plasma membrane. J. Biol. Chem. *280*, 6548–6553.

Khoshouei, M., Radjainia, M., Phillips, A.J., Gerrard, J.A., Mitra, A.K., Plitzko, J.M., Baumeister, W., and Danev, R. (2016). Volta phase plate cryo-EM of the small protein complex Prx3. Nat. Commun. *7*, 10534.

Khoshouei, M., Radjainia, M., Baumeister, W., and Danev, R. (2017). Cryo-EM structure of haemoglobin at 3.2 Å determined with the Volta phase plate. Nat. Commun. *8* 16099.

Kleerebezem, M., Crielaard, W., and Tommassen, J. (1996). Involvement of stress protein PspA (phage shock protein A) of *Escherichia coli* in maintenance of the protonmotive force under stress conditions. EMBO J. *15*, 162–171.

Klinkert, B., Ossenbühl, F., Sikorski, M., Berry, S., Eichacker, L., and Nickelsen, J. (2004). PratA, a periplasmic tetratricopeptide repeat protein involved in biogenesis of photosystem II in *Synechocystis sp. PCC 6803*. J. Biol. Chem. *279*, 44639–44644.

Kobayashi, K., Kondo, M., Fukuda, H., Nishimura, M., and Ohta, H. (2007a). Galactolipid synthesis in chloroplast inner envelope is essential for proper thylakoid biogenesis, photosynthesis, and embryogenesis. Proc. Natl. Acad. Sci. U. S. A. *104*, 17216–17221.

Kobayashi, R., Suzuki, T., and Yoshida, M. (2007b). *Escherichia coli* phage-shock protein A (PspA) binds to membrane phospholipids and repairs proton leakage of the damaged membranes. Mol. Microbiol. *66*, 100–109.

Kochovski, Z. (2014). Image analysis of molecular complexes present in cryo-tomograms of neuronal synapses. PhD Thesis. Tech. Univ. München.

Koster, A.J., Grimm, R., Typke, D., Hegerl, R., Stoschek, A., Walz, J., and Baumeister, W. (1997). Perspectives of molecular and cellular electron tomography. J. Struct. Biol. *120*, 276–308.

Kóta, Z., Horváth, L.I., Droppa, M., Horváth, G., Farkas, T., and Páli, T. (2002). Protein assembly and heat stability in developing thylakoid membranes during greening. Proc. Natl. Acad. Sci. U. S. A. *99*, 12149–12154.

Kremer, J.R., Mastronarde, D.N., and McIntosh, J.R. (1996). Computer visualization of three-dimensional image data using IMOD. J. Struct. Biol. *116*, 71–76.

Krivanek, O.L., Friedman, S.L., Gubbens, A.J., and Kraus, B. (1995). An imaging filter for biological applications. Ultramicroscopy *59*, 267–282.

Kroll, D., Meierhoff, K., Bechtold, N., Kinoshita, M., Westphal, S., Vothknecht, U.C., Soll, J., and Westhoff, P. (2001). VIPP1, a nuclear gene of *Arabidopsis thaliana* essential for thylakoid membrane formation. Proc. Natl. Acad. Sci. U. S. A. *98*, 4238–4242.

Kuijper, M., van Hoften, G., Janssen, B., Geurink, R., De Carlo, S., Vos, M., van Duinen, G., van Haeringen, B., and Storms, M. (2015). FEI's direct electron detector developments: Embarking on a revolution in cryo-TEM. J. Struct. Biol. *192*, 179–187.

Kunkel, D.D. (1982). Thylakoid centers: Structures associated with the cyanobacterial photosynthetic membrane system. Arch. Microbiol. *133*, 97–99.

Van der Laan, M., Urbanus, M.L., Ten Hagen-Jongman, C.M., Nouwen, N., Oudega, B., Harms, N., Driessen, A.J.M., and Luirink, J. (2003). A conserved function of YidC in the biogenesis of respiratory chain complexes. Proc. Natl. Acad. Sci. U. S. A. *100*, 5801–5806.

LAWRENCE, M., and POSSINGHAM, J. (1984). Observations of microtubule-like structures within spinach plastids. Biol. Cell *52*, 77–81.

Li, H. min, Kaneko, Y., and Keegstra, K. (1994). Molecular cloning of a chloroplastic proteinassociated with both the envelope and thylakoid membranes. Plant Mol. Biol. *25*, 619–632.

Li, X., Mooney, P., Zheng, S., Booth, C.R., Braunfeld, M.B., Gubbens, S., Agard, D.A., and Cheng, Y. (2013). Electron counting and beam-induced motion correction enable near-atomic-resolution single-particle cryo-EM. Nat. Methods *10*, 584–590.

Lin, D.C., and Nobel, P.S. (1971). Control of photosynthesis by Mg^{2+}. Arch. Biochem. Biophys. *145*, 622–632.

Lindquist, E., Solymosi, K., and Aronsson, H. (2016). Vesicles are persistent features of different plastids. Traffic *17*, 1125–1138.

Liu, C., Willmund, F., Whitelegge, J.P., Hawat, S., Knapp, B., Lodha, M., and Schroda, M. (2005). J-domain protein CDJ2 and HSP70B are a plastidic chaperone pair that interacts with vesicle-inducing protein in plastids 1. Mol. Biol. Cell *16*, 1165–1177.

Liu, C., Willmund, F., Golecki, J.R., Cacace, S., Heß, B., Markert, C., and Schroda, M. (2007). The chloroplast HSP70B-CDJ2-CGE1 chaperones catalyse assembly and disassembly of VIPP1 oligomers in *Chlamydomonas*. Plant J. *50*, 265–277.

Liu, T.Y., Bian, X., Romano, F.B., Shemesh, T., Rapoport, T.A., and Hu, J. (2015). *Cis* and *trans* interactions between atlastin molecules during membrane fusion. Proc. Natl. Acad. Sci. *112*, E1851–E1860.

Liu, Y.-W., Mattila, J.-P., and Schmid, S.L. (2013). Dynamin-catalyzed membrane fission requires coordinated GTP hydrolysis. PLoS One *8*, e55691.

Liu, Y., Huynh, D.T., and Yeates, T.O. (2019). A 3.8 Å resolution cryo-EM structure of a small protein bound to an imaging scaffold. Nat. Commun. *10*, 1864.

Liu, Z., Gutierrez-Vargas, C., Wei, J., Grassucci, R.A., Sun, M., Espina, N., Madison-Antenucci, S., Tong, L., and Frank, J. (2017). Determination of the ribosome structure to a resolution of 2.5 Å by single-particle cryo-EM. Protein Sci. *26*, 82–92.

Lo, S.M., and Theg, S.M. (2012). Role of vesicle-inducing protein in plastids 1 in cpTat transport at the thylakoid. Plant J. *71*, 656–668.

Lučić, V., Förster, F., and Baumeister, W. (2005). Structural studies by electron tomography: From cells to molecules. Annu. Rev. Biochem. *74*, 833–865.

Ludtke, S.J. (2016). Single-particle refinement and variability analysis in EMAN2.1. Methods Enzymol. *579*, 159–189.

Lyumkis, D. (2019). Challenges and opportunities in cryo-EM single-particle analysis. J. Biol. Chem. *294*, 5181–5197.

Mahamid, J., Pfeffer, S., Schaffer, M., Villa, E., Danev, R., Cuellar, L.K., Förster, F., Hyman, A.A., Plitzko, J.M., and Baumeister, W. (2016). Visualizing the molecular sociology at the *HeLa* cell nuclear periphery. Science. *351*, 969–972.

Male, A.L., Oyston, P.C.F., and Tavassoli, A. (2014). Self-Assembly of *Escherichia coli* Phage Shock Protein A. Adv. Microbiol. *04*, 353–359.

Mastronarde, D.N. (1997). Dual-axis tomography: An approach with alignment methods that preserve resolution. J. Struct. Biol. *120*, 343–352.

Mastronarde, D.N. (2005). Automated electron microscope tomography using robust prediction of specimen movements. J. Struct. Biol. *152*, 36–51.

McDonald, C., Jovanovic, G., Ces, O., and Buck, M. (2015). Membrane stored curvature elastic stress modulates recruitment of maintenance proteins Pspa and Vipp1. MBio *6*, e01115–e01188.

McDonald, C., Jovanovic, G., Wallace, B.A., Ces, O., and Buck, M. (2017). Structure and function of PspA and Vipp1 N-terminal peptides: Insights into the membrane stress sensing and mitigation. Biochim. Biophys. Acta - Biomembr. *1859*, 28–39.

McLaughlin, S., and Aderem, A. (1995). The myristoyl-electrostatic switch: a modulator of reversible protein-membrane interactions. Trends Biochem. Sci. *20*, 272–276.

McMullan, G., Faruqi, A.R., Clare, D., and Henderson, R. (2014). Comparison of optimal performance at 300keV of three direct electron detectors for use in low dose electron microscopy. Ultramicroscopy *147*, 156–163.

Medalia, O., Weber, I., Frangakis, A.S., Nicastro, D., Gerisch, G., and Baumeister, W. (2002). Macromolecular architecture in eukaryotic cells visualized by cryoelectron tomography. Science. *298*, 1209–1213.

Merk, A., Bartesaghi, A., Banerjee, S., Falconieri, V., Rao, P., Davis, M.I., Pragani, R., Boxer, M.B., Earl, L.A., Milne, J.L.S., et al. (2016). Breaking cryo-EM resolution barriers to facilitate drug discovery. Cell *165*, 1698–1707.

Milazzo, A.C., Cheng, A., Moeller, A., Lyumkis, D., Jacovetty, E., Polukas, J., Ellisman, M.H., Xuong, N.H., Carragher, B., and Potter, C.S. (2011). Initial evaluation of a direct detection device detector for single particle cryo-electron microscopy. J. Struct. Biol. *176*, 404–408.

Mindell, J.A., and Grigorieff, N. (2003). Accurate determination of local defocus and specimen tilt in electron microscopy. J. Struct. Biol. *142*, 334–347.

Mizuno-Yamasaki, E., Rivera-Molina, F., and Novick, P. (2012). GTPase networks in membrane traffic. Annu. Rev. Biochem. *81*, 637–659.

Montessuit, S., Somasekharan, S.P., Terrones, O., Lucken-Ardjomande, S., Herzig, S., Schwarzenbacher, R., Manstein, D.J., Bossy-Wetzel, E., Basañez, G., Meda, P., et al. (2010). Membrane remodeling induced by the dynamin-related protein Drp1 stimulates Bax oligomerization. Cell *142*, 889–901.

Morré, D.J., Selldén, G., Sundqvist, C., and Sandelius, A.S. (1991). Stromal low temperature compartment derived from the inner membrane of the chloroplast envelope. Plant Physiol. *97*, 1558–1564.

Nicastro, D., Frangakis, A.S., Typke, D., and Baumeister, W. (2000). Cryo-electron tomography of *neurospora* mitochondria. J. Struct. Biol. *129*, 48–56.

Nickell, S., Förster, F., Linaroudis, A., Del Net, W., Beck, F., Hegerl, R., Baumeister, W., and Plitzko, J.M. (2005). TOM software toolbox: Acquisition and analysis for electron tomography. J. Struct. Biol. *149*, 227–234.

Nickelsen, J., and Rengstl, B. (2013). Photosystem II assembly: From cyanobacteria to plants. Annu. Rev. Plant Biol. *64*, 609–635.

Nogales, E. (2016). The development of cryo-EM into a mainstream structural biology technique. Nat. Methods *13*, 24–27.

Nogales, E., and Scheres, S.H.W. (2015). Cryo-EM: A unique tool for the visualization of macromolecular complexity. Mol. Cell *58*, 677–689.

Nordhues, A., Schöttler, M.A., Unger, A.K., Geimer, S., Schönfelder, S., Schmollinger, S., Rütgers, M., Finazzi, G., Soppa, B., Sommer, F., et al. (2012). Evidence for a role of VIPP1 in the structural organization of the photosynthetic apparatus in *Chlamydomonas*. Plant Cell *24*, 637–659.

Ohnishi, N., Zhang, L., and Sakamoto, W. (2018). VIPP1 involved in chloroplast membrane integrity has GTPase activity *in vitro*. Plant Physiol. *177*, 328–338.

Oikonomou, C.M., and Jensen, G.J. (2017). Cellular electron cryotomography: Toward structural biology *in situ*. Annu. Rev. Biochem. *86*, 873–896.

Okazaki, K., Miyagishima, S., and Wada, H. (2015). Phosphatidylinositol 4-Phosphate negatively regulates chloroplast division in *Arabidopsis*. Plant Cell *27*, 663–674.

Osadnik, H., Schöpfel, M., Heidrich, E., Mehner, D., Lilie, H., Parthier, C., Risselada, H.J., Grubmüller, H., Stubbs, M.T., and Brüser, T. (2015). PspF-binding domain PspA1-144 and the PspA-F complex: New insights into the coiled-coil-dependent regulation of AAA+ proteins. Mol. Microbiol. *98*, 743–759.

Otters, S., Braun, P., Hubner, J., Wanner, G., Vothknecht, U.C., and Chigri, F. (2013). The first α-helical domain of the vesicle-inducing protein in plastids 1 promotes oligomerization and lipid binding. Planta *237*, 529–540.

Park, S.H., and Blackstone, C. (2010). Further assembly required: Construction and dynamics of the endoplasmic reticulum network. EMBO Rep. *11*, 515–521.

Penczek, P.A., Grassucci, R.A., and Frank, J. (1994). The ribosome at improved resolution: New techniques for merging and orientation refinement in 3D cryo-electron microscopy of biological particles. Ultramicroscopy *53*, 251–270.

Penczek, P.A.A., Zhu, J., Schröder, R., and Frank, J. (2018). 3-D reconstruction with contrast transfer compensation from defocus series. Scanning Microsc. *11*, 232–239.

Peter, B.J., Kent, H.M., Mills, I.G., Vallis, Y., Butler, P.J.G., Evans, P.R., and McMahon, H.T. (2004). BAR Domains as sensors of membrane curvature: The amphiphysin BAR structure. Science. *303*, 495–499.

Pettersen, E.F., Goddard, T.D., Huang, C.C., Couch, G.S., Greenblatt, D.M., Meng, E.C., and Ferrin, T.E. (2004). UCSF Chimera - A visualization system for exploratory research and analysis. J. Comput. Chem. *25*, 1605–1612.

Portis, A.R. (1981). Evidence of a low stromal Mg^{2+} concentration in intact chloroplasts in the dark. Plant Physiol. *67*, 985–989.

Portis, A.R., and Heldt, H.W. (1976). Light-dependent changes of the Mg^{2+} concentration in the stroma in relation to the Mg^{2+} dependency of CO_2 fixation in intact chloroplasts. BBA - Bioenerg. *449*, 434–446.

Radermacher, M. (2006). Weighted back-projection methods. In Electron Tomography, (New York, NY: Springer New York), pp. 245–273.

Rast, A., Schaffer, M., Albert, S., Wan, W., Pfeffer, S., Beck, F., Plitzko, J.M., Nickelsen, J., and Engel, B.D. (2019). Biogenic regions of cyanobacterial thylakoids form contact sites with the plasma membrane. Nat. Plants *5*, 436–446.

Reimer, L., and Kohl, H. (2008). Transmission electron microscopy physics of image formation. Springer Ser. Opt. Sci. *51*, 587.

Rigort, A., Bäuerlein, F.J.B., Villa, E., Eibauer, M., Laugks, T., Baumeister, W., and Plitzko, J.M. (2012). Focused ion beam micromachining of eukaryotic cells for cryoelectron tomography. Proc. Natl. Acad. Sci. U. S. A. *109*, 4449–4454.

Rohou, A., and Grigorieff, N. (2015). CTFFIND4: Fast and accurate defocus estimation from electron micrographs. J. Struct. Biol. *192*, 216–221.

Rosenthal, P.B., and Henderson, R. (2003). Optimal determination of particle orientation, absolute hand, and contrast loss in single-particle electron cryomicroscopy. J. Mol. Biol. *333*, 721–745.

Rupprecht, E., Düppre, E., and Schneider, D. (2010). Similarities and singularities of three DnaK proteins from the cyanobacterium *synechocystis sp. PCC 6803*. Plant Cell Physiol. *51*, 1210–1218.

Ruskin, R.S., Yu, Z., and Grigorieff, N. (2013). Quantitative characterization of electron detectors for transmission electron microscopy. J. Struct. Biol. *184*, 385–393.

Rütgers, M., and Schroda, M. (2013). A role of VIPP1 as a dynamic structure within thylakoid centers as sites of photosystem biogenesis? Plant Signal. Behav. *8*, e27037.

Saur, M., Hennig, R., Young, P., Rusitzka, K., Hellmann, N., Heidrich, J., Morgner, N., Markl, J., and Schneider, D. (2017). A Janus-Faced IM30 Ring Involved in Thylakoid Membrane Fusion Is Assembled from IM30 Tetramers. Structure *25*, 1380-1390.e5.

Schaffer, M., Mahamid, J., Engel, B.D., Laugks, T., Baumeister, W., and Plitzko, J.M. (2017). Optimized cryo-focused ion beam sample preparation aimed at *in situ* structural studies of membrane proteins. J. Struct. Biol. *197*, 73–82.

Scheffers, D.J., and Driessen, A.J.M. (2002). Immediate GTP hydrolysis upon FtsZ polymerization. Mol. Microbiol. *43*, 1517–1521.

Scheffers, D.J., De Wit, J.G., Den Blaauwen, T., and Driessen, A.J.M. (2002). GTP hydrolysis of cell division protein FtsZ: Evidence that the active site is formed by the association of monomers. Biochemistry *41*, 521–529.

Scheres, S.H. (2014). Beam-induced motion correction for sub-megadalton cryo-EM particles. Elife *3*, e03665.

Scheres, S.H.W. (2016). Processing of structurally heterogeneous cryo-EM data in RELION. Methods Enzymol. *579*, 125–157.

Scheres, S.H.W.W. (2012). RELION: Implementation of a Bayesian approach to cryo-EM structure determination. J. Struct. Biol. *180*, 519–530.

Schneider, C.A., Rasband, W.S., and Eliceiri, K.W. (2012). NIH Image to ImageJ: 25 years of image analysis. Nat. Methods *9*, 671–675.

Schnell, D.J., Blobel, G., Keegstra, K., Kessler, F., Ko, K., and Soll, J. (1997). A consensus nomenclature for the protein-import components of the chloroplast envelope. Trends Cell Biol. *7*, 303–304.

Schnepf, E. (1961). Piastidenstrukturen bei *Passiflora*. Protoplasma *54*, 310–313.

Schorb, M., Haberbosch, I., Hagen, W.J.H., Schwab, Y., and Mastronarde, D.N. (2019). Software tools for automated transmission electron microscopy. Nat. Methods *16*, 471–477.

Schuller, J.M., Falk, S., Fromm, L., Hurt, E., and Conti, E. (2018). Structure of the nuclear exosome captured on a maturing preribosome. Science. *360*, 219–222.

Schur, F.K.M., Obr, M., Hagen, W.J.H., Wan, W., Jakobi, A.J., Kirkpatrick, J.M., Sachse, C., Kräusslich, H.-G., and Briggs, J.A.G. (2016). An atomic model of HIV-1 capsid-SP1 reveals structures regulating assembly and maturation. Science. *353*, 506–508.

Schweitzer, A., Aufderheide, A., Rudack, T., Beck, F., Pfeifer, G., Plitzko, J.M., Sakata, E., Schulten, K., Förster, F., and Baumeister, W. (2016). Structure of the human 26S proteasome at a resolution of 3.9 Å. Proc. Natl. Acad. Sci. U. S. A. *113*, 7816–7821.

Selão, T.T., Zhang, L., Knoppová, J., Komenda, J., and Norling, B. (2016). Photosystem II assembly steps take place in the thylakoid membrane of the cyanobacterium *Synechocystis sp. PCC6803*. Plant Cell Physiol. *57*, 95–104.

Shaul, O. (2002). Magnesium transport and function in plants: The tip of the iceberg. BioMetals *15*, 309–323.

Sigworth, F.J. (1998). A maximum-likelihood approach to single-particle image refinement. J. Struct. Biol. *122*, 328–339.

Sigworth, F.J., Doerschuk, P.C., Carazo, J.-M., and Scheres, S.H.W. (2010). An introduction to maximum-likelihood methods in cryo-EM. Methods Enzymol. *482*, 263–294.

Sorzano, C.O.S., Marabini, R., Pascual-Montano, A., Scheres, S.H.W., and Carazo, J.M. (2006). Optimization problems in electron microscopy of single particles. Ann. Oper. Res. *148*, 133–165.

Standar, K., Mehner, D., Osadnik, H., Berthelmann, F., Hause, G., Lünsdorf, H., and Brüser, T. (2008). PspA can form large scaffolds in *Escherichia coli*. FEBS Lett. *582*, 3585–3589.

Stengel, A., Gügel, I.L., Hilger, D., Rengstl, B., Jung, H., and Nickelsen, J. (2012). Initial steps of photosystem II *de novo* assembly and preloading with manganese take place in biogenesis centers in *Synechocystis*. Plant Cell *24*, 660–675.

Strádalová, V., Stahlschmidt, W., Grossmann, G., Blažíková, M., Rachel, R., Tanner, W., and Malinsky, J. (2009). Furrow-like invaginations of the yeast plasma membrane correspond to membrane compartment of Can1. J. Cell Sci. *122*, 2887–2894.

Takenawa, T. (2010). Phosphoinositide-binding interface proteins involved in shaping cell membranes. Proc. Japan Acad. Ser. B Phys. Biol. Sci. *86*, 509–523.

Tegunov, D., and Cramer, P. (2019). Real-time cryo-electron microscopy data preprocessing with Warp. Nat. Methods *16*, 1146–1152.

Theis, J., Gupta, T.K., Klingler, J., Wan, W., Albert, S., Keller, S., Engel, B.D., and Schroda, M. (2019). VIPP1 rods engulf membranes containing phosphatidylinositol phosphates. Sci. Rep. *9*, 8725.

Thurotte, A., Brüser, T., Mascher, T., and Schneider, D. (2017). Membrane chaperoning by members of the PspA/IM30 protein family. Commun. Integr. Biol. *10*, e1264546.

Trabuco, L.G., Villa, E., Schreiner, E., Harrison, C.B., and Schulten, K. (2009). Molecular dynamics flexible fitting: A practical guide to combine cryo-electron microscopy and X-ray crystallography. Methods *49*, 174–180.

Vothknecht, U.C., Otters, S., Hennig, R., and Schneider, D. (2012). Vipp1: A very important protein in plastids?! J. Exp. Bot. *63*, 1699–1712.

Wagner, T., Merino, F., Stabrin, M., Moriya, T., Antoni, C., Apelbaum, A., Hagel, P., Sitsel, O., Raisch, T., Prumbaum, D., et al. (2019). SPHIRE-crYOLO is a fast and accurate fully automated particle picker for cryo-EM. Commun. Biol. *2*, 218.

Walter, B., Hristou, A., Nowaczyk, M.M., and Schünemann, D. (2015). *In vitro* reconstitution of co-translational D1 insertion reveals a role of the cpSec-Alb3 translocase and Vipp1 in Photosystem II biogenesis. Biochem. J. *468*, 315–324.

Walz, J., Typke, D., Nitsch, M., Koster, A.J., Hegerl, R., and Baumeister, W. (1997). Electron tomography of single ice-embedded macromolecules: Three- dimensional alignment and classification. J. Struct. Biol. *120*, 387–395.

Wang, P., and Dalbey, R.E. (2011). Inserting membrane proteins: The YidC/Oxa1/Alb3 machinery in bacteria, mitochondria, and chloroplasts. Biochim. Biophys. Acta - Biomembr. *1808*, 866–875.

Wang, L., Shkolnisky, Y., and Singer, A. (2013). A Fourier-based approach for iterative 3D reconstruction from cryo-EM images. ArXiv Prepr. ArXiv1307.5824.

Wehmer, M., Rudack, T., Beck, F., Aufderheide, A., Pfeifer, G., Plitzko, J.M., Förster, F., Schulten, K., Baumeister, W., and Sakata, E. (2017). Structural insights into the functional cycle of the ATPase module of the 26S proteasome. Proc. Natl. Acad. Sci. *114*, 1305–1310.

Weiner, L., and Model, P. (1994). Role of an *Escherichia coli* stress-response operon in stationary-phase survival. Proc. Natl. Acad. Sci. *91*, 2191–2195.

Weiss, G.L., Kieninger, A.K., Maldener, I., Forchhammer, K., and Pilhofer, M. (2019). Structure and function of a bacterial gap junction analog. Cell *178*, 374-384.e15.

Weiß, D., Schneider, G., Niemann, B., Guttmann, P., Rudolph, D., and Schmahl, G. (2000). Computed tomography of cryogenic biological specimens based on X-ray microscopic images. Ultramicroscopy *84*, 185–197.

Westphal, S., Soll, J., and Vothknecht, U.C. (2001a). A vesicle transport system inside chloroplasts. FEBS Lett. *506*, 257–261.

Westphal, S., Heins, L., Soll, J., and Vothknecht, U.C. (2001b). Vipp1 deletion mutant of *synechocystis*: A connection between bacterial phage shock and thylakoid biogenesis? Proc. Natl. Acad. Sci. U. S. A. *98*, 4243–4248.

Williams, D.B., and Carter, C.B. (2009). Transmission electron microscopy: A textbook for materials science (Boston, MA: Springer US, 2nd edition).

Wolf, D. (2017). One ring, two membranes: IM30 ring complex and the thylakoid membrane fusion. Structure *25*, 1321–1322.

Yamaguchi, S., Reid, D.A., Rothenberg, E., and Darwin, A.J. (2013). Changes in Psp protein binding partners, localization and behaviour upon activation of the *Yersinia enterocolitica* phage shock protein response. Mol. Microbiol. *87*, 656–671.

Youle, R.J., and Van Der Bliek, A.M. (2012). Mitochondrial fission, fusion, and stress. Science. *337*, 1062–1065.

Zak, E., Norling, B., Maitra, R., Huang, F., Andersson, B., and Pakrasi, H.B. (2001). The initial steps of biogenesis of cyanobacterial photosystems occur in plasma membranes. Proc. Natl. Acad. Sci. U. S. A. *98*, 13443–13448.

Zhang, K. (2016). Gctf: Real-time CTF determination and correction. J. Struct. Biol. *193*, 1–12.

Zhang, L., and Sakamoto, W. (2013). Possible function of VIPP1 in thylakoids. Plant Signal. Behav. *8*, e22860.

Zhang, L., and Sakamoto, W. (2015). Possible function of VIPP1 in maintaining chloroplast membranes. Biochim. Biophys. Acta - Bioenerg. *1847*, 831–837.

Zhang, L., Kato, Y., Otters, S., Vothknecht, U.C., and Sakamoto, W. (2012). Essential role of VIPP1 in chloroplast envelope maintenance in *Arabidopsis*. Plant Cell *24*, 3695–3707.

Zhang, L., Kondo, H., Kamikubo, H., Kataoka, M., and Sakamoto, W. (2016a). VIPP1 has a disordered C-terminal tail necessary for protecting photosynthetic membranes against stress. Plant Physiol. *171*, 1983–1995.

Zhang, L., Kusaba, M., Tanaka, A., and Sakamoto, W. (2016b). Protection of chloroplast membranes by VIPP1 rescues aberrant seedling development in *Arabidopsis* nyc1 mutant. Front. Plant Sci. *7*, 1–11.

Zhang, S., Shen, G., Li, Z., Golbeck, J.H., and Bryant, D.A. (2014). Vipp1 is essential for the biogenesis of Photosystem I but not thylakoid membranes in *Synechococcus sp. PCC 7002*. J. Biol. Chem. *289*, 15904–15914.

Zheng, S.Q., Palovcak, E., Armache, J.-P.J.P.J.-P., Verba, K.A., Cheng, Y., and Agard, D.A. (2017). MotionCor2: Anisotropic correction of beam-induced motion for improved cryo-electron microscopy. Nat. Methods *14*, 331–332.

Zhou, Z.H., and Chiu, W. (1993). Prospects for using an IVEM with a FEG for imaging macromolecules towards atomic resolution. Ultramicroscopy *49*, 407–416.

Zhou, W., Parent, L.J., Wills, J.W., and Resh, M.D. (1994). Identification of a membrane-binding domain within the amino-terminal region of human immunodeficiency virus type 1 Gag protein which interacts with acidic phospholipids. J. Virol. *68*, 2556–2569.

Zhou, Z.H., Hardt, S., Wang, B., Sherman, M.B., Jakana, J., and Chiu, W. (1996). CTF determination of images of ice-embedded single particles using a graphics interface. J. Struct. Biol. *116*, 216–222.

Zivanov, J., Nakane, T., Forsberg, B.O., Kimanius, D., Hagen, W.J.H., Lindahl, E., and Scheres, S.H.W. (2018). New tools for automated high-resolution cryo-EM structure determination in RELION-3. Elife *7*, e42166.

Zubelli, J.P., Marabini, R., Sorzano, C.O.S., and Herman, G.T. (2003). Three-dimensional reconstruction by Chahine's method from electron microscopic projections corrupted by instrumental aberrations. Inverse Probl. *19*, 933–949.

9 Acknowledgements

The work of this thesis was conducted in the Department of Molecular Structural Biology at the Max Planck Institute for Biochemistry in Martinsried. I would like to thank all department members for the good working atmosphere. In particular, I would like to thank the following people.

I would like to thank Prof. Baumeister for giving me this rare opportunity to learn and work in this exceptional department not only due to its amazing equipment but also the highly inspiring work atmosphere.

I would like to give special thanks to (late) Prof. Walter Neupert that he allowed me to work under his supervision and introduced me to the mitochondrial biology and MICOS complex. I am also very thankful for the support provided by Dr. Max Harner for the MICOS biochemistry. It was wonderful learning with him. I would also like to thank Prof. Elizabeth Villa who was my first supervisor and helped me join this department.

My special thanks go to my supervisor Dr. Benjamin (Ben) Engel, who gave me the freedom to work independently and supported me whenever I needed support. He was always there to assist me with my data collections and figure making efforts. He is also a good friend of mine who introduced me to my first beer and probably meet as well. In all the ups and downs of the Ph.D. studies, he always encouraged me, motivated me and had a deep faith in my abilities.

Especially in the first years of my studies, I would have been lost without Prof. Jürgen Plitzko, who has been such a great mentor and helped me with technical problems and allow me early on to access the microscope independently.

This department would not be running smoothly without the help from Inga Wolf and Günter Pfeiffer, who reliably provides technical support and maintenance. Günter is always there when it comes to any help at the microscopes. I am also thankful for his generous supplies for the grids to me for the negative stain EM. I want to thank Birgit Book, Nathalie Leclerq and Eva Sartorius, who are always helpful when it comes to any bureaucratic issue. I recall a memory that I would like to mention here. When I came to Germany from India to join this department, that was the first time I was traveling outside India and was also my first plane ride. Honestly, I was scared especially how will I come from the airport and how will I find the institute. Birgit Book arranged institute car pick-up for me. Only later I learned that it was an exceptional arrangement. I am grateful for her support.

I am also very much thankful for our collaborators at the TU Kaiserslautern especially Prof. Michael Schroda, Jasmine Theis and Karin Gries. Furthermore, I am extremely thankful to Jan Schuller for his technical support and training and his knowledge of single-particle data analysis. Without his help, the Single-particle structure of Vipp1 would have been extremely difficult.

The second person I met on my arrival was Dr. Ganesh Pathare. I recall that he immediately gave me his phone and asked me to call India to inform my parents that I arrived safely (By the way, that is a big thing for Indian parents to know). Meeting him was a great relief as I didn't know anyone in Germany. He was a great colleague and tremendous support during my initial months in Germany. He is now a very close friend. Among my colleagues my special thanks go to my former and current group members: Sahradha and Wojciech. My time in the department would not have been the same without the friendship of Uli, Tim, Saikat and most recently also Cristina and Chuan. I am grateful that our lives shared the same path for the last months and years and I am grateful for your scientific expertise.

This acknowledgment is not complete without acknowledging the support of my very close friends. I can not be where I am today without the help of Ashutosh Bajpai, who lend me books to study because I didn't have money to buy them. He treated me like his brother and supported me like his friend. Dheerendra and Arpit

supported me, encouraged and motivated me in the moments of self-doubts. Manovriti Thakur who has been a great friend and supported me during my PhD. I am very much grateful to Claudia for her unconditional support and laughter during my thesis writing phase.

My gratitude goes to my parents for their sacrifices and supporting me unlimitedly during all these years of study in a field that they know nothing about. Although my parents have no relation to science they trusted me to go this long path of education and helped me out whenever I needed them. My dear brothers, Prashant and Gaurav always encouraged me by trusting in my abilities, more than myself.

I spent a long time in this department and I am thankful to so many people who supported me, guided me and helped me in making this PhD journey a very wonderful one. Thank you so much, everyone!